Section D

INTERDISCIPLINARY AND MULTIDISCIPLINARY PROBLEMS

ELECTROSTATIC FIELD ANALYSIS USING HEAT TRANSFER ANALOGY

M. Blagojević[1], M. Živković[2], R. Slavković[3]

[1] Faculty of Mechanical Engineering
The University of Kragujevac, Sestre Janjić 6, 34000 Kragujevac
e-mail: blagoje@kg.ac.rs
[2] Faculty of Mechanical Engineering
The University of Kragujevac, Sestre Janjić 6, 34000 Kragujevac
e-mail: zile@kg.ac.rs
[3] Faculty of Mechanical Engineering
The University of Kragujevac, Sestre Janjić 6, 34000 Kragujevac
e-mail: radovan@kg.ac.rs

Abstract. The electrostatic problems are mathematically very similar to the solution of heat conduction problem. For the low-frequency problems addressed by this paper, a subset of Maxwell's equations (Gauss' Law and Ampere's loop law) is used. Using an analogy of electrostatic and heat transfer problems, software PAK-E is developed. The program solves potential over a user-defined domain for user-defined sources and boundary conditions. Dirichlet boundary condition is used, which gives the value of the potential on specified boundaries. Electric displacement and field intensity are related to one another via the constitutive relationship.

In example shown in this paper the electrostatic potential in linear dielectric material is calculated. The geometry studied is a symmetric quadrant of a plane capacitor. Solution calculated by in-house software modul PAK-E is compared by solutions of other software. Various field variables as well as physical parameters can be calculated based on the potential. Solution calculated by in-house software PAK-E is equivalent to solutions of world leading software.

1. Introduction

Electrostatic interactions between charges govern much of physics, chemistry and biology. The charges are static in the sense of charge amount (it is constant in time) and their positions in space (charges are not moving relatively to each other). Electrostatic problems consider the behavior of electric field intensity, E, and electric flux density D. Quantities of interest in electrostatic analysis are voltages, electric fields, capacitances, and electric forces. Electrostatic analysis is used to design or analyze variety of capacitive systems.

2. Mathematical Description of Physical Phenomena

Numerical solution of problem can begin when the laws governing these processes have been expressed in mathematical form, generally in terms of differential equations. In this

section, some basic equations of used theories are briefly reviewed. Emphasis is on the presentation of various differential equations and boundary conditions that define boundary-value problems to be solved by finite element analysis.

2. 1 Governing Differential Equations for Electrostatics

According to classical electrodynamics theory, Maxwell's equations are set of fundamental equations that govern all macroscopic electromagnetic phenomena. An entire set of fundamental laws of electromagnetic field theory are the result of observation and experiment. The field equations are expressed in terms of the derived field quantities, Equations (1)-(5)

$$\nabla \times \mathbf{E} = -\frac{\partial \mathbf{B}}{\partial t}, \tag{1}$$

$$\nabla \times \mathbf{H} = \mathbf{J} + \frac{\partial \mathbf{D}}{\partial t}, \tag{2}$$

$$\nabla \cdot \mathbf{D} = \rho, \tag{3}$$

$$\nabla \cdot \mathbf{B} = 0, \tag{4}$$

$$\nabla \cdot \mathbf{J} = -\frac{\partial \rho}{\partial t}. \tag{5}$$

where $\mathbf{E}$ is electric field, $\mathbf{D}$ is electric flux density, $\mathbf{H}$ is magnetic field, $\mathbf{B}$ is magnetic flux density, $\mathbf{J}$ is electric current density, and ρ is electric charge density.

Constitutive relations. The constitutive relationships describe the macroscopic properties of medium being considered. In the most general case, derived fields are complicated nonlocal, nonlinear functional of the primary fields $\mathbf{E}$ and $\mathbf{B}$. Under certain conditions, we may assume that the response of a substance to the fields may be approximated as a linear one. For linear materials the fields and fluxes are simply related, so that:

$$\mathbf{D} = \varepsilon \mathbf{E}, \tag{6}$$

$$\mathbf{B} = \mu \mathbf{H}, \tag{7}$$

$$\mathbf{J} = \sigma \mathbf{E}. \tag{8}$$

The constitutive parameters ε, μ, σ denote, respectively, the permittivity (farads/meter), permeability (henrys/meter), and conductivity (siemens/meter) of the medium. These parameters are tensors for anisotropic media, and scalars for isotropic media. For inhomogeneous media, they are function of position, whereas for homogenous media they are not.

The final form of electric permittivity ε depends on the material properties. Electrically nonlinear materials are materials in which the electric permittivity depends on the electric field intensity:

$$\varepsilon = \varepsilon(\mathbf{E}). \tag{9}$$

The permittivity $\varepsilon = \varepsilon_0 \varepsilon_r$ is defined through the permittivity of vacuum ε_0 and the relative permittivity of the material ε_r. That means that the derived fields are linearly proportional to the primary fields and that the electric displacement is only dependent on the electric field.
When the field quantities do not vary with time, the field is called static. In this case, Equations (1) can be written as:

$$\nabla \times \mathbf{E} = 0\,, \tag{10}$$

In this case there are no interactions between electric and magnetic fields. Therefore, we can have separately either an electrostatic or a magnetostatic case.
To solve Maxwell's equations, one may first convert the first order differential equations involving two field quantities into second-order involving only one field quantity. As it is mentioned above, the electrostatic field is governed by equations (1) and (6). The latter can be satisfied by representing the electric field as:

$$\mathbf{E}(\mathbf{r}) = -\nabla \Phi(\mathbf{r})\,, \tag{11}$$

where Φ is called electric scalar potential. Substituting (11) into (1) with aid of (9), one obtains

$$-\nabla \cdot (\varepsilon \nabla \Phi) = \rho\,, \tag{12}$$

or

$$\boxed{-\boldsymbol{\varepsilon} \nabla^2 \Phi = \rho}\,, \tag{13}$$

which is second-order differential equation governing Φ. Equation (12) is the Poison equation which is one of the Maxwell's equations.

Initial and boundary conditions. While there are many functions that satisfy the differential equations given above in the domain of interest, only one of them is the real solution to the problem. Complete description of a problem should include information about both differential equations and boundary conditions. There is a unique solution for given boundary conditions.
In general, boundary conditions can be: prescribed potential at S_1 part (14), interface between different media at S_2 part (15), given surface charge density at S_3 part (16),

$$\Phi = \Phi_{\mathrm{s}}(x, y, z, t)\,, \tag{14}$$

$$\mathbf{n} \times (\mathbf{D}_1 - \mathbf{D}_2) = \rho_s\,, \tag{15}$$

$$\rho_s = \rho_s(x, y, z)\,, \tag{16}$$

where ρ_{s} is surface charge density and S_1, S_2 and S_3 are parts of the surface S, as symbolically represented in Figure 1.
Problem is linear, due to a fact that all differential equations that describe problem and boundary conditions are linear dependent on electric potential.

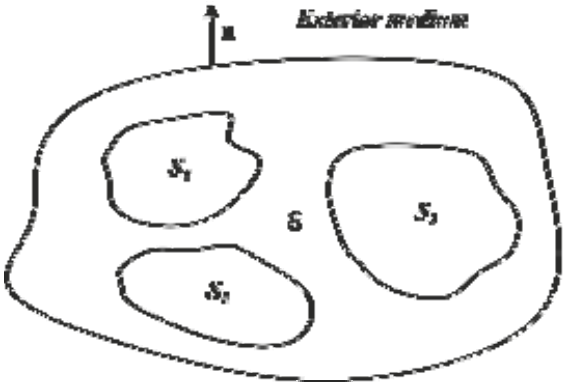

Figure 1. Boundary conditions for the electrostatic problem.

2.2. Governing Differential Equations for Heat transfer

Differential equation of energy balance equation is based on fundamental principle of energy conservation. In case when material characteristics do not depend on temperature and radiation does not exist as a boundary condition, problem is linear, due to a fact that all differential equations that describe heat conduction law and boundary conditions are linear dependent on temperature.
Complete derivation of these equations, considering heat transfer boundary conditions, is given in the literature [1], [2] and [3].

2.3. Heat transfer – Electrostatics analogy

The electrostatic problems are mathematically very similar to the solution of heat conduction problem. Equations describing electrostatic field (13) and heat transfer are second order differential equations of the same form. Analogies that exist between particular quantities are given in Table 1.

Table 1. Electrostatic – Heat Transfer Analogy

Heat transfer	
Temperature	T
/	/
/	/
Heat Flux	$q = -k\nabla^2 T$
Thermal Conductivity Tensor	$k = \begin{bmatrix} k_x & 0 & 0 \\ 0 & k_y & 0 \\ 0 & 0 & k_z \end{bmatrix}$

Electrostatics	
Field Potential	Φ
Electrostatic Field	$\mathbf{E} = -\nabla\Phi$
Electric Displacement	$\mathbf{D} = -\varepsilon\mathbf{E}$
Electric Charge Density	$\rho = -\varepsilon\nabla^2\Phi$
Electric Permittivity Tensor	$\varepsilon = \begin{bmatrix} \varepsilon_x & 0 & 0 \\ 0 & \varepsilon_y & 0 \\ 0 & 0 & \varepsilon_z \end{bmatrix}$

3. Incremental finite element equations implemented in PAK-E software

The derivation of the finite element balance equations is based on equations given in the previous text. Galerkin method is then applied, for derivation of FE equations. Based on Poison differential equation (13), the following can be written

$$\int_{\mathrm{V}}\left[h_{\mathrm{I}}\sum_{\mathrm{j}=1}^{3}\frac{\partial}{\partial \mathrm{x}_{\mathrm{j}}}\left(\varepsilon_{\mathrm{j}}\frac{\partial \Phi}{\partial x_{\mathrm{j}}}\right)\right]\mathrm{d}V+\int_{\mathrm{V}}h_{\mathrm{I}}\rho\mathrm{d}V=0 \qquad \mathrm{I}=1,2,\ldots,\mathrm{N}, \tag{17}$$

where h_{I} are interpolation functions and N is number of nodes per element, and V is finite element volume. Three-dimensional (3D) isoparametric finite element is applied, as defined in [2]. Interpolation functions, geometry and number of nodes are also adopted. Electric potential Φ in a point of element, defined in natural coordinates r,s,t is given as:

$$\Phi\left(r,s,t\right)=\sum_{\mathrm{I}=1}^{\mathrm{N}}h_{\mathrm{I}}\boldsymbol{\Phi}^{\mathrm{I}}, \tag{18}$$

or in matrix form,

$$\Phi=\mathbf{H}\boldsymbol{\Phi}, \tag{19}$$

where

$$\mathbf{H}=\left[h_1 \quad h_2 \quad \ldots \quad h_{\mathrm{N}}\right], \tag{20}$$

$$\boldsymbol{\Phi}^{\mathrm{T}}=\left[\Phi^1 \quad \Phi^2 \quad \ldots \quad \Phi^{\mathrm{N}}\right], \tag{21}$$

are row matrix of interpolation functions and column matrix of nodal potentials, respectively.

Applying the partial integration and Gauss theorem on the first integral in (17), the following is obtained

$$\begin{aligned}&\int_{\mathrm{V}}\left[h_{\mathrm{I}}\sum_{\mathrm{j}=1}^{3}\frac{\partial}{\partial x_{\mathrm{j}}}\left(\varepsilon_{\mathrm{j}}h_{\mathrm{J,j}}\right)\right]\mathrm{d}V\Phi^{\mathrm{J}}=\\&=-\int_{\mathrm{V}}\left(\sum_{\mathrm{j}=1}^{3}\varepsilon_{\mathrm{j}}h_{\mathrm{I,j}}h_{\mathrm{J,j}}\right)\mathrm{d}V\Phi^{\mathrm{J}}+\int_{\mathrm{S}}\left[h_I^{\mathrm{s}}\sum_{\mathrm{j}=1}^{3}\varepsilon_{\mathrm{j}}\frac{\partial\Phi}{\partial x_{\mathrm{j}}}n_{\mathrm{j}}\right]\mathrm{d}S\end{aligned}. \tag{22}$$

When element surface heat flux q_{n} is given and based on, the following can be written

$$\int_{\mathrm{S}}\left[h_{\mathrm{I}}^{\mathrm{s}}\sum_{\mathrm{j}=1}^{3}\varepsilon_{\mathrm{j}}\frac{\partial\Phi}{\partial x_{\mathrm{j}}}n_{\mathrm{j}}\right]\mathrm{d}S=\int_{\mathrm{S}}h_{\mathrm{I}}^{\mathrm{s}}q_{\mathrm{n}}\mathrm{d}S=\mathrm{Q}_{\mathrm{I}}^{\mathrm{q_n}}, \tag{23}$$

where $\mathrm{Q}_{\mathrm{I}}^{\mathrm{q_n}}$ are electric charge density column matrix components and $h_{\mathrm{I}}^{\mathrm{s}}$ are interpolation functions for nodes on surface S_2.

Using (22)-(23), (17) and (18), the system of equations of the following form is obtained

$$\mathbf{K}\boldsymbol{\Phi}=\mathbf{Q}, \tag{24}$$

where matrix components for K and column matrix Q are determined as

$$\mathbf{K}_{\mathrm{IJ}}=\mathbf{K}_{\mathrm{IJ}}^{\varepsilon}+\mathbf{K}_{\mathrm{IJ}}^{\sigma}, \tag{25}$$

$$\mathbf{Q}_{\mathrm{I}}=\mathbf{Q}_{\mathrm{I}}^{\mathrm{q}}+\mathbf{Q}_{\mathrm{I}}^{\mathrm{q_n}}+\mathbf{Q}_{\mathrm{I}}^{\sigma}. \tag{26}$$

Coefficients of electric permittivity matrix $\mathrm{K}_{\mathrm{IJ}}^{\varepsilon}$ are given by

$$\mathbf{K}_{\mathrm{IJ}}^{\varepsilon}=\int_{\mathrm{V}}\left(\sum_{\mathrm{j}=1}^{3}\varepsilon_{\mathrm{j}}h_{\mathrm{I,j}}h_{\mathrm{J,j}}\right)\mathrm{d}V=\int_{\mathrm{V}}\left(\varepsilon_{\mathrm{x}}h_{\mathrm{I,x}}h_{\mathrm{J,x}}+\varepsilon_{\mathrm{y}}h_{\mathrm{I,y}}h_{\mathrm{J,y}}+\varepsilon_{\mathrm{z}}h_{\mathrm{I,z}}h_{\mathrm{J,z}}\right)\mathrm{d}V, \tag{27}$$

where derivatives of interpolation functions are given by $h_{\mathrm{I,x}}=\partial h_{\mathrm{I}}/\partial x,\ldots,h_{\mathrm{J,z}}=\partial h_{\mathrm{J}}/\partial z$. By using interpolation matrix H, defined by row matrix according to(20), matrices in (24) can be written in a next form

$$\mathbf{K}^{\varepsilon}=\int_{\mathrm{V}}\mathbf{B}^{\mathrm{T}}\varepsilon\mathbf{B}\mathrm{d}V, \tag{28}$$

$$\mathbf{K}^{\sigma}=\int_{\mathrm{S}}\mathbf{H}^{\mathrm{sT}}\varepsilon\mathbf{H}^{s}\mathrm{dS}, \tag{29}$$

$$\mathbf{Q}^{\mathrm{q}}=\int_{\mathrm{V}}\rho\mathbf{H}^{\mathrm{T}}\mathrm{d}V, \tag{30}$$

$$\mathbf{Q}^{\mathrm{q_n}}=\int_{\mathrm{S}}\sigma\mathbf{H}^{\mathrm{sT}}\mathrm{d}S. \tag{31}$$

Row matrices H^{s} contain interpolation functions $h_{\mathrm{I}}^{\mathrm{s}}$ for the surfaces. The matrix $\mathbf{B}$ in (28) has a next form like

$$\mathbf{B}=\begin{bmatrix}\mathbf{B}^{1} & \mathbf{B}^{2} & \ldots & \mathbf{B}^{\mathrm{N}}\end{bmatrix}, \tag{32}$$

where, the submatrix for the node $\mathbf{I}$ consist of derivatives of interpolation functions with respect to coordinates x, y and z

$$\mathbf{B}^{\mathrm{I}}=\begin{bmatrix}h_{\mathrm{I,x}}\\ h_{\mathrm{I,y}}\\ h_{\mathrm{I,z}}\end{bmatrix}. \tag{33}$$

Equation (24) represents energy balance equation for 3D finite element. Total number of equations is equal to number of nodes. One potential value corresponds to each node. In case of 2D, previous expressions remain unchanged, except that integrals over a volume V are practically reduced to integrals over surface S of the finite element, as shown in [2]. Interpolation functions h_{I} have appropriate forms for 2D problem.

To solve the balance equation of the structure, we observe steady electric field in most general case when material constants depend on the electric potential. The implicit iterative scheme for solution of system equations (24) is analog to developed in the literature [1], [2] and [3].
Iterative procedure is continued until potential increment at nodes is not sufficiently low, what can be expressed in the following form

$$\left\|\Delta\boldsymbol{\Phi}^{(i)}\right\| \leq \varepsilon_a , \tag{34}$$

or

$$\frac{\left\|\Delta\boldsymbol{\Phi}^{(i)}\right\|}{\left\|\Delta\boldsymbol{\Phi}^{(1)}\right\|} \leq \varepsilon_r , \tag{35}$$

where ε_a and ε_r are selected absolute and relative tolerances and $\left\|\Delta\boldsymbol{\Phi}^{(i)}\right\|$ is electric potential increment norm.

4. Example: Capacitor with a Square Cross-Section

This example will show analyzing of a capacitor with a square cross-section. The geometry studied is a symmetric quadrant of a plane capacitor having a rectangular hole in inner plate. The outer square has a 40 mm size and the inner square has a 20 mm size, as shown below in Figure 2. The geometry extends for 1000 mm in the *into-the-page* direction. Because of the symmetry, only one quarter of the device need be modeled.

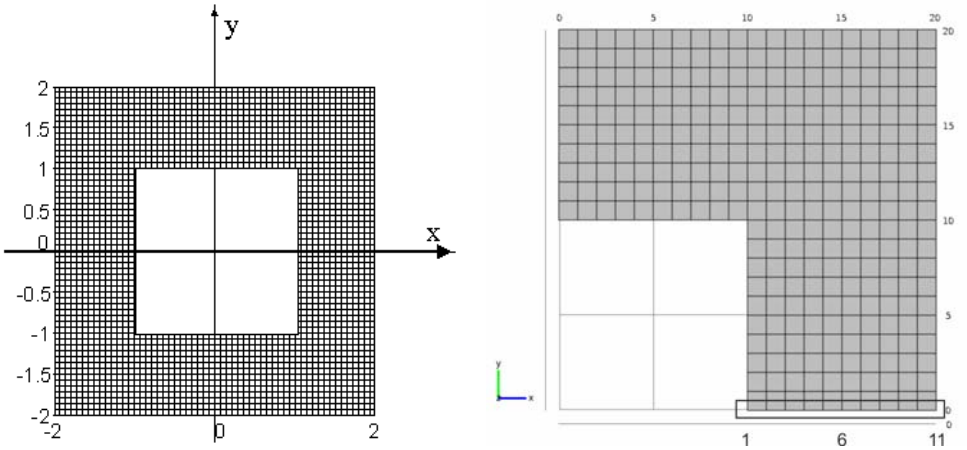

Figure 2. Square Capacitor Cross-Section and Computational mesh used in simulations.

Finite element model was created in the software Femap [11]. The dielectric between the plates is air, with unit electrical permittivity. Inner conductor (nodes at lines x=10mm and y=10mm) is at the potential of 1V and outer conductor (nodes at lines x=20mm and y=20mm) is grounded. Nodes at lines x=0 and y=10 have symmetry as boundary condition. The model consists of 300 elements and 341 nodes. The finished, ready for analysis model, looks like as pictured in Figure 2.

5. Results of calculations

PAK-E numerical results of previously described example are compared with the results obtained by COMSOL Multiphysics. COMSOL Multiphysics [10] is a software environment for the modeling and simulation of any physics-based system. A particular strength is its ability to account for multiphysics phenomena. Optional modules add discipline-specific tools for acoustics, batteries & fuel cells, chemical engineering, earth science, electromagnetic (linear/nonlinear magnetostatic problems, linear/nonlinear time harmonic magnetic problems, linear electrostatic problems), fluid dynamics, heat transfer, MEMS, plasma, and structural analysis. Software is composed of an interactive shell encompassing graphical pre- and post-processing; a mesh generator; and various solvers.
Post-processing of the PAK-E calculation results is performed in software FEMAP. Interface between the FEM solver PAK-E and software for results post-processing FEMAP has been made through *.neu file [8], [9].
Figure 3 shows the scalar field of electric potential numerically calculated by software COMSOL Multiphysics. Figure 4 shows the scalar field of electric potential numerically calculated by software PAK-E.
Comparison of the numerical analysis results (Figure 5) was done by the potential values observationat the nodes numbered 1 to 11 in Figure 2. There are insignificant differences in numerical results available in the third decimals, which can be attributed to numerical error. Developed software gives excellent results compared to the world's leading software for solving coupled problems COMSOL Multiphysics [10].

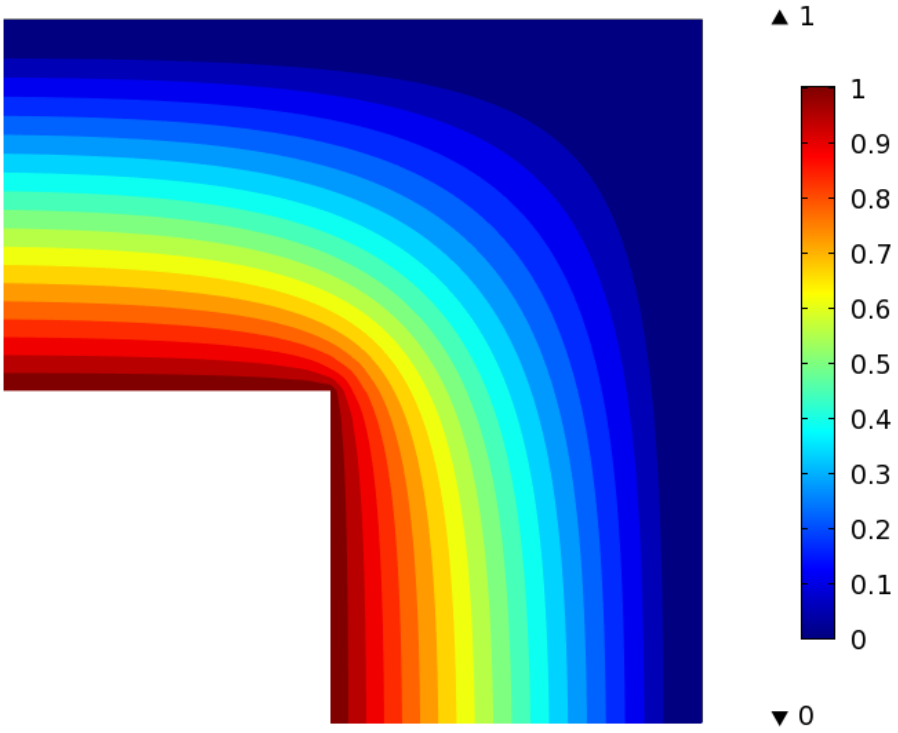

Figure 3. Solution to the example calculated by solver COMSOL.

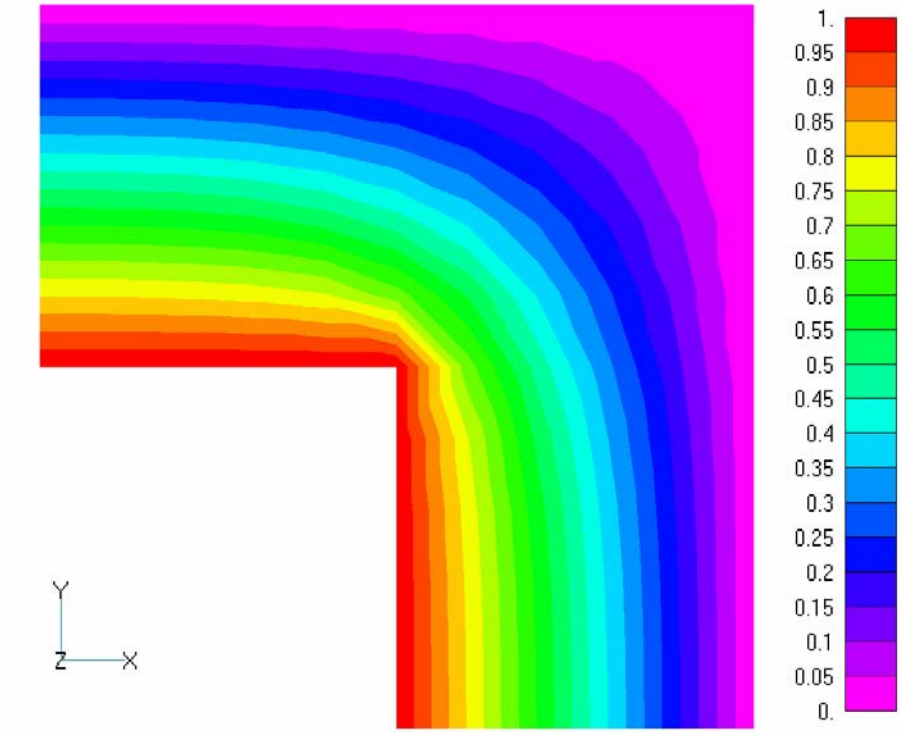

Figure 4. Solution to the example calculated by solver PAK.

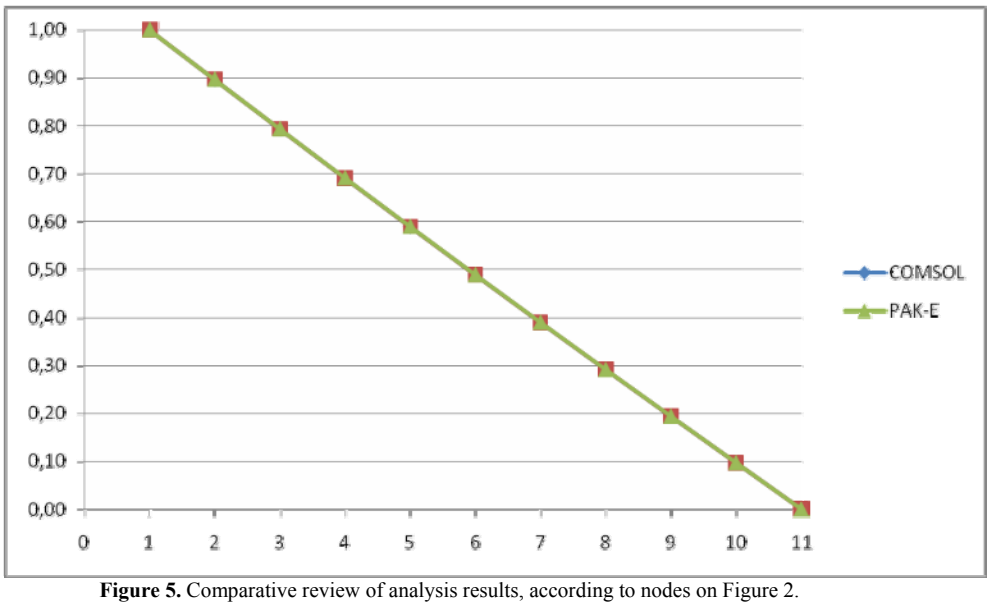

Figure 5. Comparative review of analysis results, according to nodes on Figure 2.

6. Conclusion

There are two conditions that quantities describing electric field must obey. The first condition is the differential form of Gauss' Law, which says that the flux out of any closed volume is equal to the charge contained within the volume. The second is the differential form of Ampere's loop law. Displacement and field intensity are related to one another via the constitutive relationship. The program employs the electric scalar potential Φ to simplify the computation of fields. The program solves for potential Φ over a user-defined domain with user-defined sources and boundary conditions.
PAK-E can perform linear and nonlinear electrostatic analysis for 2-D, axisymmetric and 3D models. Following options are available for electrostatic analysis: (a) Material properties: orthotropic materials with constant and variable permittivity ε, (b) Loading sources: voltages V, and electric charge density ρ, (c) Boundary conditions: prescribed potential values (voltages), prescribed values for surface charges, and prescribed constraints for constant potential boundaries with given total charges, (d) Post-processing results: voltages, electric fields, gradients of electric field, flux densities (electric displacements) and surface charges.
This case presents solving for electric potential. Electrostatic potential in linear dielectric material and in conducting medium is calculated. Various field variables as well as physical parameters can be calculated based on the potential. The setting of this kind can be used to study the effects of geometrical features on the capacitance and on the electrostatic force, which both are meaningful quantities for further coupled simulations in e.g. micro-electro-mechanical systems.
Compared with most of academic software that solves these types of problems, program PAK-E has considerably more advanced features (3D elements, surface charges distribution as function of position, nonlinear analyses…). Solution calculated by in-house software PAK-E is equivalent to solutions of world leading software.

Acknowledgement. The part of this research is supported by Ministry of Education and Science, Republic of Serbia, Grant TR32036.

References

[1] Živković M, Nikolić A, Slavković R, Živić F (2011) Nonlinear Transient Heat Conduction Analisis of Insulation Wall ot Tank for Transportation of Liquid Aluminium, Thermal Science, Vol.14, No. 3, pp. 00-00, ISSN 0354-9836, Doi 10.2298/TSCI100506029Z,
[2] Kojić M, Slavković R, Živković M and Grujović N (1998) Finite element method I – Linear analysis, Faculty of Mechanical Engineering in Kragujevac, University of Kragujevac, Kragujevac.
[3] Bathe K J (1996) Finite Element Procedures, Prentice Hall, amazon.com
[4] Lewis W R, Nithiarasu P, Seetharamu N K (2005) Fundamentals of the Finite Element Method for Heat and Fluid Flow, John Wiley & Sons, Ltd.
[5] Rothwell J E, Cloud J M (2001) Electromagnetics, CRC Press.
[6] Meeker D (2010) Finite Element Method Magnetics, Version 4.2, User's Manual.
[7] QuickField™, Finite Element Analysis System, Version 5.8, User's Guide, Tera Analysis Ltd.
[8] Rakić D, Nikolić A, Živković M, Slavković R (2008) GID-PAK Interface, Proceedings of the 4th Conference on Advances and Applications of GiD, 2008, May.
[9] Rakić D, Nikolić A, Čukanović D (2008) PAK-T interface for software GID, YU INFO 2008 - 14th Conference on information and technology communications, Kopaonik, Serbia, 2008, 09th - 12th March 2008, pp. 91, ISBN 978-86-85525-03-2
[10] http://www.comsol.com/
[11] http://www.plm.automation.siemens.com/en_us/products/velocity/femap/index.shtml

DETERMINATION OF MINIMAL ROLL RATE FOR GYRO STABILIZED PROJECTILE

Zoran Gajić[1], Milan Milošević[2], Srđan Stojković[3]

[1] Military technical institute, Belgrade,
Ratka Resanovića no. 1, Belgrade
e-mail: zoran.gajic52@gmail.com
[2] Military technical institute, Belgrade,
Ratka Resanovića no. 1, Belgrade
e-mail: marija.m@beotel.net
[3] Military technical institute, Belgrade,
Ratka Resanovića no. 1, Belgrade
e-mail: ssdmb@scnet.rs

ABSTRACT. In this paper, based on mathematical model of projectile flight with 6DoF, the effect of various angles of installed rocket motors nozzles to the gyro-stabilized projectile roll rate was analyzed. The dynamic stability and dissipation of hits on the target place in the range and direction was analyzed. For the particular projectile it was solved a problem due to wrench of warhead as a result of excessive rotation. The minimal roll rate around the projectile longitudinal axis, from the standpoint of the rocket dynamic stability was determined.

1. Introduction

Statically unstable projectiles can be stabilized on the trajectory by the rotation around its longitudinal axis. One possibility to achieve this is to mount rocket motor nozzles at an angle φ, as it was shown in Fig.1.

In the pre-project phase for the active-reactive projectiles it is necessary to prescribe minimal roll rate around the longitudinal axis, which ensure stable flight in both phases: **active phase** – with the thrust, and the **passive phase** – without the thrust.

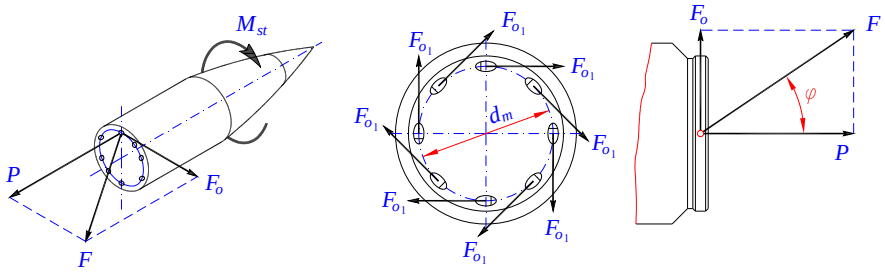

Fig. 1 Projectile rotation caused by the angled nozzles

In the first assumption we can consider that stability is guaranteed towards whole trajectory if the minimal roll rate is achieved [3]:

$$n_{\min} = \frac{2 \cdot \sqrt{R \cdot I_x \cdot e}}{I_y}$$

where :
R – resultant aerodynamic force,
e – distance between the center of inertia and the thrust center,
I_x , I_y - projectile longitudinal and transverse moments of inertia.

During the flight along the trajectory, projectile changes its speed, intensity and position of aerodynamic force R. This type of stabilization provides only the oscillatory nature of change of cinematic quantities of disturbed movement. Decrease or increase of the amplitude of oscillatory movement is related for the problems of dynamic stability, and it depends on the forces and moments acting the projectile – mainly on the damping and Magnus moment.
In the passive phase of the flight projectile acceleration (slowdown) is small, so the changes of dynamic coefficients in the equations of motion are also small.
In the active phase of the flight, due to the large changes of the flight speed, dynamic coefficients changes notable. This system is significantly unsteady, so that considerably complicates the study of stability.

2. Factors affecting the projectile movement

We considered the projectile as a rigid body in the space with six degrees of freedom of motion, with changeable mass, and forces and moments acting on it, changes in relation of its speed. So they are defined in the function of Mach number.

2.1. Coefficients of reactive moment due to angled nozzles

Stabilizing moment from *n* nozzles, according the Fig. 1 can be presented as:

$$M_{st} = F_{o1} \cdot \frac{d_m}{2} \cdot n \qquad (1)$$

F_{o1} - tangential force at one nozzle,

d_m - mean diameter at which there are nozzles,

$P = I_t / t_a$

$F_o = P \cdot tg\varphi$ - total axial and tangential forces of all nozzles,

$I_t = \int_0^{t_a} P \cdot dt$ - rocket motor total impulse,

t_a - rocket motor burn-out time.

Reactive moment from nozzles can be defined through the coefficient of reactive moment m_{xr}, and than we have:

$$M_{xr} = m_{xr} \cdot l_{ref} \cdot P \tag{2}$$

By equating expressions (1) and (2), we get:

$$m_{xr} = \frac{d_m \cdot tg\varphi}{2 \cdot l_{ref}}$$

and it is function of a nozzle geometry.

2.2 Aerodynamic forces and moments

For the stabilization of statically unstable projectiles we need a high spin and therefore in the equations for the total force and moment Magnus force and moment must be included. Calculation of these quantities is very complicated process with unreliable outputs with regard to the fact that this phenomenon is manifested in the boundary layer.
In the [1] a detail theoretical analysis of Magnus effects, for the configuration of cylindrical body with ogive nose, was presented. This analysis was also verified experimentally.
Theory presented in [1] predicts a sudden increase of Magnus coefficient in transonic region which leads to the unstable projectile flight as a consequence. It was shown that the Magnus coefficient is directly proportional to the boundary layer thickness.
Forming of the vortices on the downstream side of the cylindrical projectile body generates nonlinearity of Magnus moment versus angle of attack.

Moments in the pitching and yaw planes are:

$$M = M_\alpha \cdot \alpha + M_q \cdot q + M_{p\beta} \cdot p \cdot \beta \qquad \text{pitching}$$

$$N = N_\beta \cdot \alpha + N_r \cdot r + N_{p\alpha} \cdot p \cdot \alpha \qquad \text{yawing}$$

where:

$$M_{p\beta} = \frac{\partial^2 M}{\partial_p \partial_\beta} = \frac{\partial^2 c_m}{\partial_\beta \partial (p \cdot l_{ref} / 2 \cdot u)} \cdot \frac{q_\infty \cdot S \cdot l_{ref}^2}{2 \cdot u} = c_{m_{p\beta}} \cdot \frac{q_\infty \cdot S \cdot l_{ref}^2}{2 \cdot u}$$

The last terms in the above equations for the moments are Magnus coefficients with respectively changed indexes.

2.2.1 Coefficients of Magnus moment $C_{Mp\alpha}$ *and force* $C_{Np\alpha}$

For the symmetrical projectiles there are relations between aerodynamic coefficients in the fixed and aero-ballistic coordinate systems, so we have:

$$C_{Mp\alpha} = C_{\square mp\beta} = C_{\tilde{n}p\alpha}$$

According to the [2], coefficients of Magnus moment and force, determinated by the experiment, are shown in the Fig. 2 and Fig. 3.

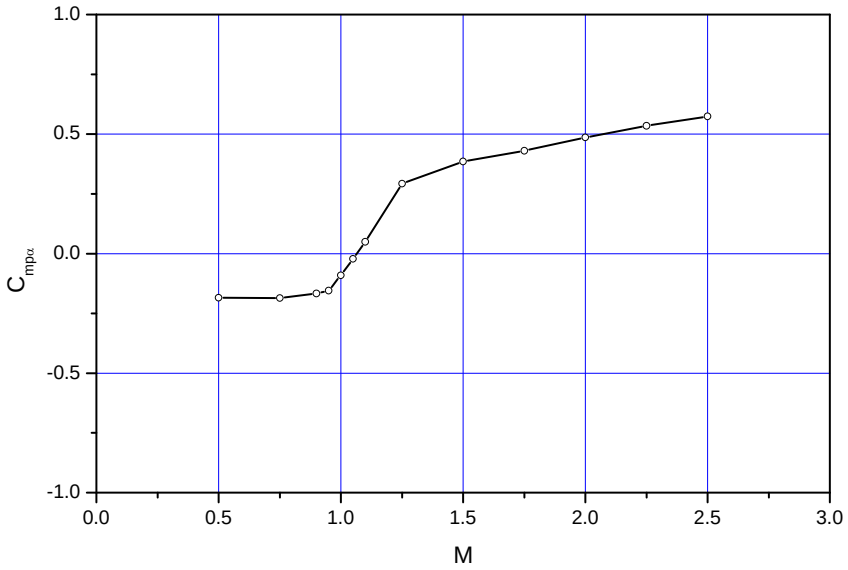

Fig. 2 Coefficient of Magnus moment

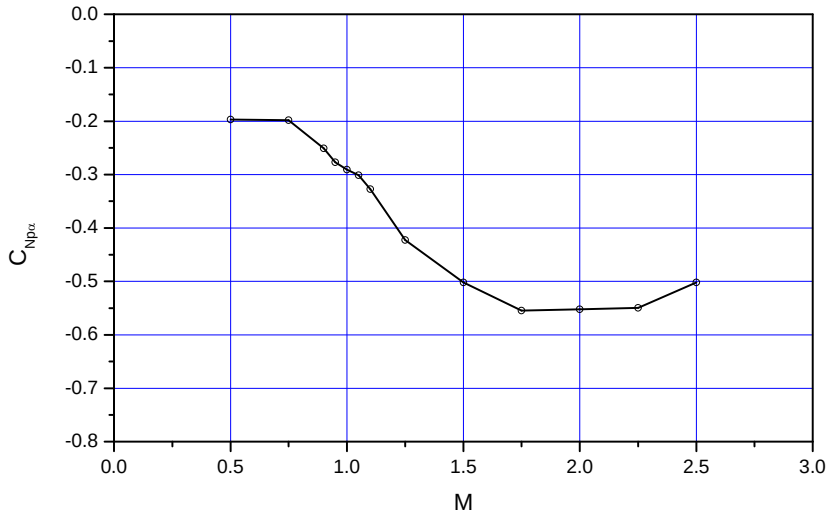

Fig. 3 Coefficient of Magnus force

3. Gyroscopic and dynamic stability

The limit curve of the gyroscopic and dynamic stability for a stable flight in the passive phase is shown in Fig. 5 (solid line) [2]. The criterion is derived from the linearized equation of projectile motion in the side plane versus complex angle of attack.

In the classical ballistic the factor of gyroscopic stability S_g is defined as:

$$S_g = \frac{I_x{}^2 \cdot p^2}{2 \cdot \rho \cdot I_y \cdot S \cdot d \cdot V^2 \cdot C_{m\alpha}} > 1 \tag{3}$$

while the dynamic stability factor S_d is:

$$S_d = \frac{2\left(C_{L\alpha} + k_x{}^{-2} \cdot C_{mp\alpha}\right)}{C_{L\alpha} - C_D - k_y{}^{-2}\left(C_{mq} + C_{m\dot{\alpha}}\right)} \tag{4}$$

where:

$k_x{}^{-2} = \frac{m \cdot d^2}{I_x}$, $k_y{}^{-2} = \frac{m \cdot d^2}{I_y}$,

$C_{L\alpha}$ - derivative of normal force coefficient with angle of attack,

C_D - axial force coefficient at zero angle of attack,

$\left(C_{mq} + C_{m\dot{\alpha}}\right)$ - derivatives of pitching moments coefficients due to pitch rate and due to , shown in Fig.4.

These two derivatives are difficult to separate even in the experiment.

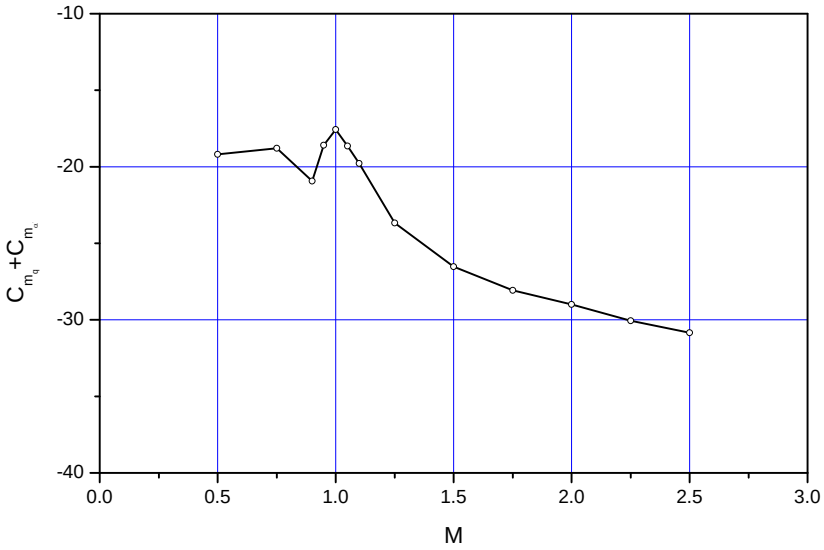

Fig. 4 Derivatives of pitching moments

For the statically unstable projectiles gyroscopic stability is a necessity but not a sufficient condition to be dynamically stable. In other words, gyroscopic stable projectile may be or may be not dynamically stable, but gyroscopic unstable projectile is always dynamically unstable. From this it follows:

1. If the dynamic stability factor S_d is inside the range $0 < S_d < 2$, a statically unstable projectile can be always stabilized by the rotation.
2. If the dynamic stability factor S_d is outside of this range, statically unstable projectile could not be dynamically stabilized at any level of rotation.

Previous statements can be presented by next relation:

$$S_g > \frac{1}{S_d\left(2 - S_d\right)} \tag{5}$$

by other words, coefficient S_d must be within boundary curve defined by this inequality.

If the coefficient S_d is inside the range $0.8 < S_d < 1.2$, and if $S_g > 1$ this is sufficient condition for the projectile to be stable by both criteria.

4. Numerical simulation and experiment

For the particular projectile, with the nozzle mounting angle of $\varphi = 14^{\circ}$, the experiment was carried out by the shooting at the test field. Several projectiles had a lot shortened trajectory compared to the calculated trajectory, which generate suspicion that some anomalies arises. The check out of dynamic stability was done, and it is shown in Fig.5. According to the analysis, in the one small part, the experimental curve S_g - S_d (red line) is

outside of the boundary curve (black line, generated by the equation 5). This is understandable because that section is related to the active phase of the flight, and a criterion was derived for passive phase of the flight. In the Fig. 6 it is shown that projectile accomplish the condition 1 - $0 < S_d < 2$, for the dynamic stability.

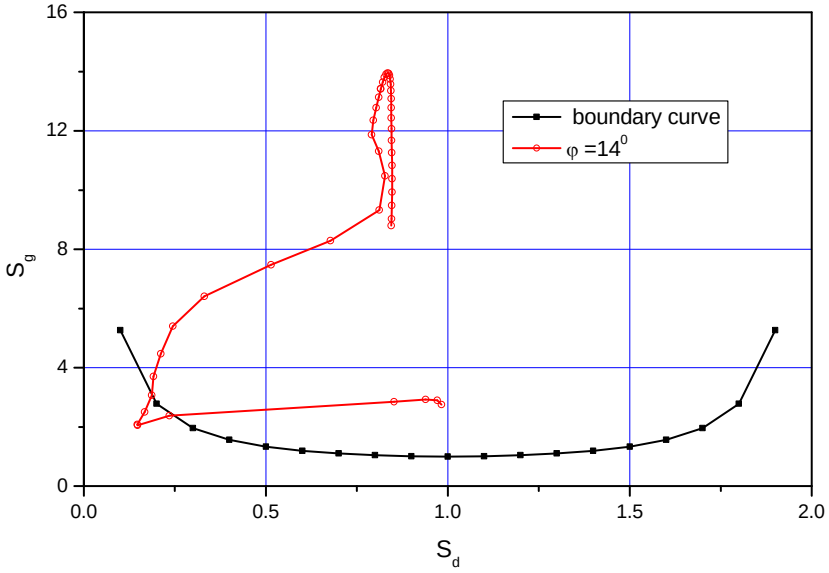

Fig. 5 Gyroscopic stability factor S_g versus dynamic stability factor S_d

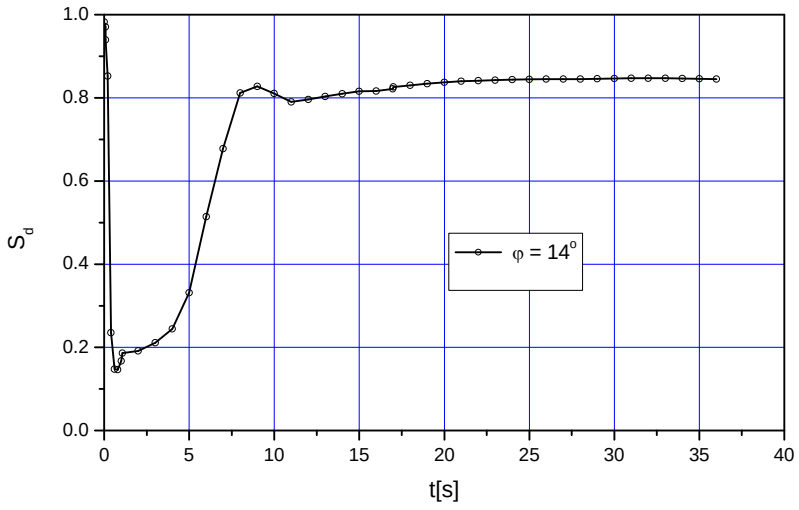

Fig. 6 Dynamic stability factor S_d

Next step was checking out the values of Magnus moment coefficient. By numerical simulation, this coefficient was hypothetically increased for 20%. This change caused significant decrease of range and increase of angle of attack, up to $\alpha = 15^{\circ}$. With the respect to the fact that unguided projectiles regularly fly with:

$$(\alpha, \beta) \leq 1.5^{\circ} \tag{6}$$

this case was dismissed.

5. The selection of the minimal nozzle mounting angle

According to the equation (2) stabilized – reactive moment is directly proportional to the nozzle mounting angle. In order to choose the minimal mounting angle of nozzle which accomplish stability criteria and condition given by (6), the various angles were used in numerical simulations: $\varphi = 10^{\circ}, 11^{\circ}, 12^{\circ}, 14^{\circ}$.

5.1 Dynamical behavior of projectile

For the different values of nozzle mounting angle, obtained results by numerical simulation are presented in the diagram S_g versus S_d. It was shown in the Fig. 7.

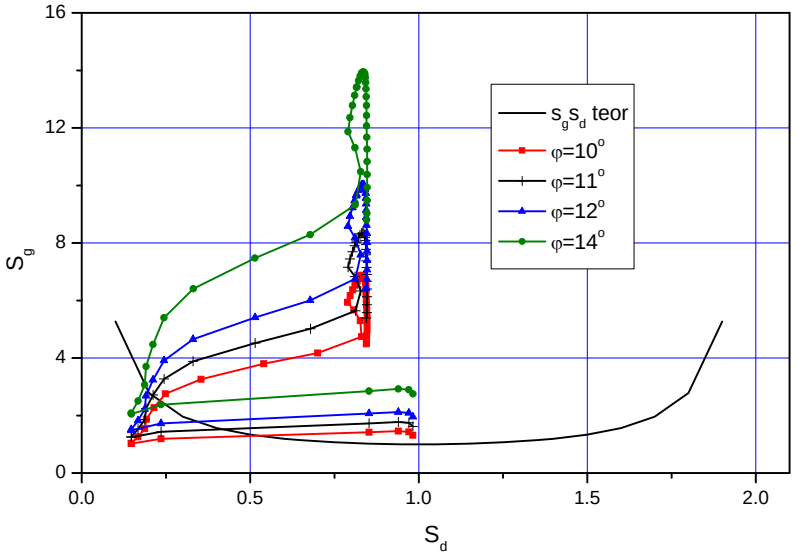

Fig. 7 Stability factors for the various nozzle mounting angles

According to the diagrams in the Fig. 7, all varied mounting angles produce rotation that satisfies conditions for projectile to be gyroscopically and dynamically stable.

Also, it is necessary to analyze the change of the angle of attack α and slide angle β, to see behavior of the projectile and damping during the flight.

For all variants of nozzle mounting angle we have restriction (6). The simulation results are shown in Fig. 8 and Fig. 9.

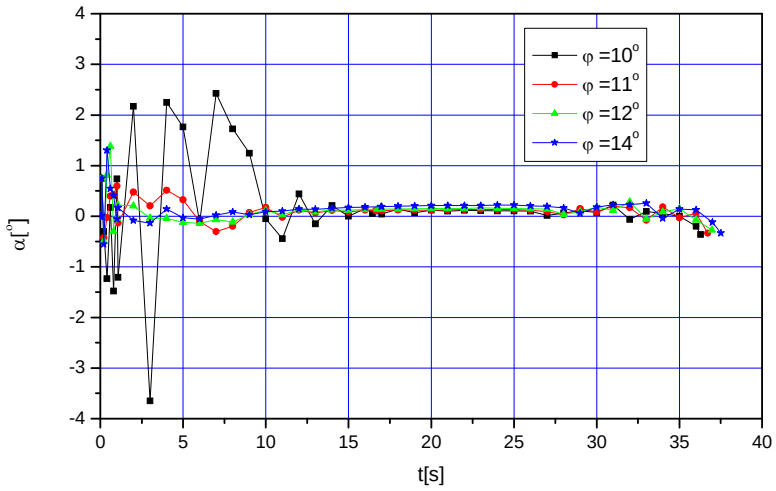

Fig. 8 The change of the angle of attack during the flight

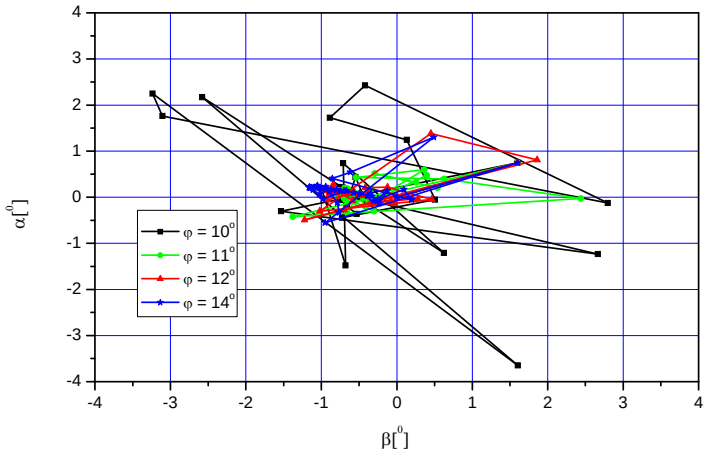

Fig. 9 Angle of attack versus slide angle for various nozzle mounting angles

With the nozzle mounting angle of $\varphi = 10^{\circ}$ projectile achieve to the too high angle of attack and slide angle, and later becomes stable. Therefore this variant does not satisfy condition (6).

Minimal nozzle mounting angle that satisfy conditions of stable flying is $\varphi = 11^{\circ}$.

6. Conclusion

By the numerical simulation of projectile flight, with the model of 6DoF, we get next results. With decreasing nozzle mounting angle from $\varphi = 14^{\circ}$ to $\varphi = 11^{\circ}$ we obtained:

- reducing the roll rate for 7000 min^{-1}, and by this avoided unnecessary additional mechanical security of the warhead – rocket motor assemble,
- solving problem due to wrench of warhead during the flight,
- reducing projectile diversion due to derivation for amount of 250 m at the maximal range,
- increasing the maximal range for 1.2% due to saving rotation energy,
- insignificant contribution to the dispersion of the hits at the target place.

Reference

[1] Vaughn H. R. and Reist G. E (1973) A Magnus Theory, *AIAA Journal*, **V11**, $N^{0}10$.

[2] McCoy L. Robert (1998) *Modern Exterior Ballistics, Modern Launch and Flight Dynamics of Symmetric Projectiles*, Schiffer Military History.

[3] Куров В. Д., Должанскии ИО. М. Основи проектированија порохових ракетних снарјадов, Москва 1961, Научно- техническое издателство.

GUIDED EARTH TO EARTH MISSILE IMPACT POINTS DISPERSION DUE TO COMMERCIAL IMU MEASUREMENT ERRORS

Mandić Slobodan[1], Vukmirica Vladimir[2], Stojković Srdjan[3]

[1] Military Technical Institute
Ratka Resanovica 1, Belgrade, Serbia
e-mail: msmanda@open.telekom.rs
[2] Military Technical Institute,
Ratka Resanovica 1, Belgrade, Serbia
e-mail: div1@ptt.rs
[3] Military Technical Institute,
Ratka Resanovica 1, Belgrade, Serbia
e-mail: ssdmb@scnet.rs

ABSTRACT. The guidance law of the ground-to-ground missile guidance system is based on the deviation of the actual trajectory from the nominal ballistic trajectory. Estimation of the missile trajectory parameters the navigation algorithm in spherical axis system is developed with assumption that specific forces and angular rates of the missile in body axis system is known. The measurement errors of the accelerometers and rate gyros are modeled as a function of the scale factor, bias instability, dead band and noise. These measurement parameters for commercial IMU ADIS16365 are determined in laboratory. IMU measurement errors are dominant for impact point dispersion of the guided surface-to-surface missile. There is no practical influence of the external disturbances to the impact points dispersion. The imapct point dispersion of the guided surface-to-surface missile is one fifth of the dispersion of the unguided ballistic missile of the same range.

1. Introduction

Basic requirements for the ground-to-ground rockets are increase of the range and increase of the accuracy. In order to minimize the influence of disturbances to the impact points dispersion, extensive study is oriented to the development of a cost effective guidance and control system which can be added to the ground-to-ground rockets [1],[2],[3],[4].
Elimination of the disturbances to the ground-to-ground missile is achieved by guidance law which relates flight path angle correction to the deviation of the disturbed trajectory from nominal trajectory (calculated ballistic trajectory without disturbances) [5]. The same guidance law is valid for vertical and horizontal plane.

$$\Delta\gamma_c(x) = -\frac{\partial\gamma_c}{\partial h}(x)\,\Delta h(x) - \frac{\partial\gamma_c}{\partial V}(x)\,\Delta V(x)\,. \tag{1}$$

where: $\Delta\gamma_c$ - flight path angle correction in vertical plane, Δh - trajectory deviations in vertical plane from nominal trajectory, ΔV - missile velocity deviation from nominal

value, $\frac{\partial \gamma_c}{\partial h}$ partial derivatives of the flight path angle relative to the trajectory deviation, and $\frac{\partial \gamma_c}{\partial V}$ - partial derivatives of the flight path angle relative to the velocity deviation.

Desired flight path angle in vertical plane (γ_c) is obtained by adding the corrections $\Delta\gamma_c$ to the nominal value of the flight path angle (γ).

$$\gamma_c(x) = \gamma(x) + \Delta\gamma_c(x) \tag{2}$$

The flight path guidance system with synthetic pitch autopilot with accelerometer and rate gyro is used to steer the rocket to the target (Fig. 1). The procedure of the guidance loop Synthesis and normal acceleration autopilot design is given in [6],[7],[8].

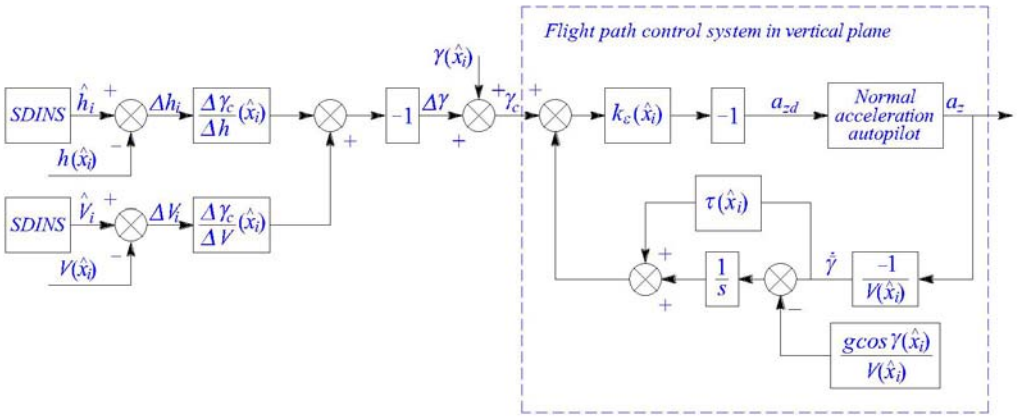

Figure 1. Guidance loop in the vertical plane

Analysis of the guidance law efficiency is done with assumption that the there is no IMU measurement errors.

Estimation of the rocket position in the space is done by SDINS (Strap Dawn Inertial Navigation System) which is composed of Inertial Measurement Unit (IMU) and Navigation Algotitham.

The purpose of this paper is to analyze of the mathematical model of SDINS navigation algorithm, IMU Analog Devices ADIS 16365 accelerometers and rate gyros measurements errors and influence of the IMU measurement errors and disturbances to the guided ground-to-ground missile impact points dispersion.

2. SDINS Mathematical Model

2.1 Mathematical Model of Navigation Algorithm

Strap-down inertial system (SDINS) navigation is widely used for estimation of the rocket position and velocity. Block diagram of the general navigation algorithm is given in Fig. 2 [9]. Position and velocity estimation is based on the known initial position and initial velocity, and on measured specific forces and angular rates. Navigation algorithm includes correction of the measured acceleration by gravity and Coriolis acceleration.

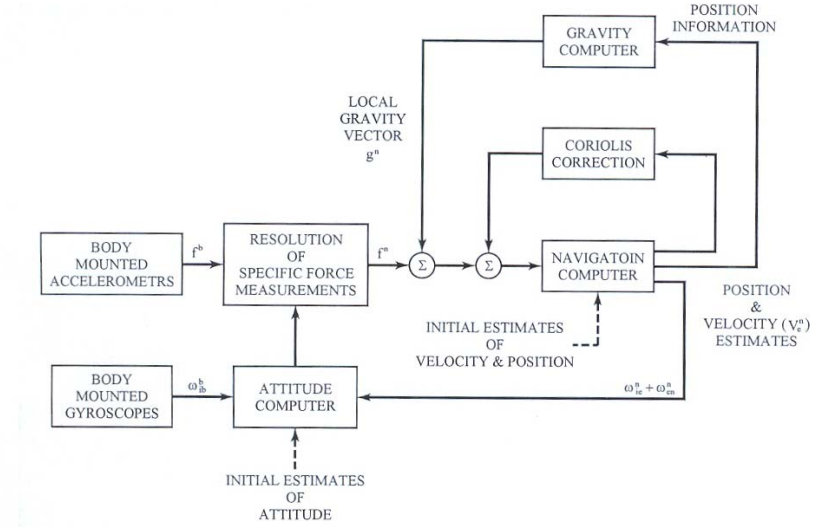

Figure 2. Guidance loop in the vertical plane

Differential equation of the rocket velocity in arbitrary navigation axis system [9] is

$$\dot{\mathbf{v}}_e^n = \mathbf{f}^n - \left[2\boldsymbol{\omega}_{ie}^n + \boldsymbol{\omega}_{en}^n\right] \times \mathbf{v}_e^n + \mathbf{g}_l^n \tag{3}$$

Position of the target relative to the launching position is defined by the basic axis system which is Earth fixed axis system (F_0). The origin of the basic axis system coincides with the launch point. Ox_0 axis is directed to the target. The plane Ox_0y_0 is tangent to the Earth's surface and the axis Oz_0 is directed vertically down (along the gravity vector). The position of F_0 is determined by the azimuth angle A_0 with respect to the local Earth fixed reference frame F_{le} (Fig. 3) [10].

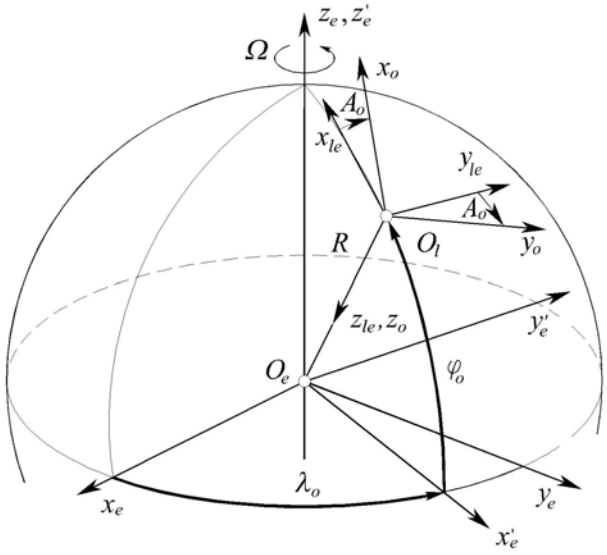

Figure 3. Basic and Local Earth fixed and basic axis system

Since guidance of the ground to ground rockets requires correction of the rocket position relative to the ballistic trajectory, the spherical axis system (F_S) is used for navigation system. Position of the spherical axis system relative to the basic axis system is defined by range angle σ_y and deviation angle σ_x (Fig. 4).

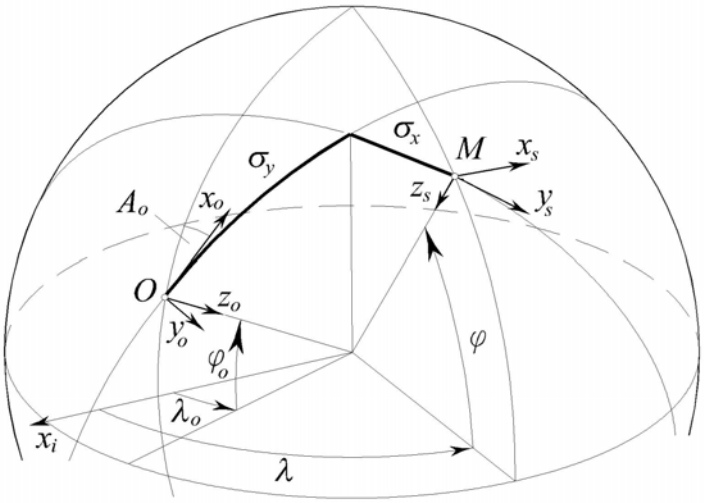

Figure 4. Spherical axis system

Differential equation of the kinematic velocity in arbitrary navigation can be applied to the spherical axis system.

$$\dot{\mathbf{v}}_e^s = \mathbf{f}^s - \left[2\boldsymbol{\omega}_{ie}^s + \boldsymbol{\omega}_{es}^s\right] \times \mathbf{v}_e^s + \mathbf{g}_l^s \tag{4}$$

where $\mathbf{v}_e^s$ is kinematic velocity of the rocket in spherical axis system

$$\mathbf{v}_e^s = \begin{bmatrix} v_{x_s} & v_{y_s} & v_{z_s} \end{bmatrix}^T \tag{5}$$

Angular rate of the Earth relative to the inertial axis system in spherical axis system ($\boldsymbol{\omega}_{ie}^s$) can be obtained by multiplication of the angular rate of the Earth in Earth axis system $\boldsymbol{\omega}_{ie}^e = \begin{bmatrix} 0 & 0 & \Omega \end{bmatrix}^T$ and transformation matrix from Earth axis system to spherical axis system.

$$\boldsymbol{\omega}_{ie}^s = \mathbf{C}_0^s \mathbf{C}_l^0 \mathbf{C}_e^l \boldsymbol{\omega}_{ie}^e = \mathbf{C}_e^s \boldsymbol{\omega}_{ie}^e \tag{6}$$

Angular rate of the spherical axis system relative to the basic axis system is defined by two angular rates $\dot{\sigma}_x$ and $\dot{\sigma}_y$. These two angular rates depends on rocket velocity relative to Earth in spherical axis system v_{x_S}, v_{y_S} and rocket altitude h.

$$\boldsymbol{\omega}_{0s}^s = \begin{bmatrix} 0 & \dot{\sigma}_y & \dot{\sigma}_x \end{bmatrix}^T = \begin{bmatrix} 0 & \dfrac{v_{x_S}}{R_0 + h} & \dfrac{-v_{y_S}}{R_0 + h} \end{bmatrix}^T \tag{7}$$

Specific force in spherical axis system $\mathbf{f}^s$ is determined by specific force in body axis system $\mathbf{f}^b$ and transformation matrix from body to spherical axis system $\mathbf{C}_b^s(\psi,\theta,\phi)$.

$$\mathbf{f}^s = \mathbf{C}_b^s(\psi,\theta,\phi)\,\mathbf{f}^b \tag{8}$$

Gravity has only the components in z_s direction of the spherical axis system

$$\mathbf{g}^s = \begin{bmatrix} 0 & 0 & g(h) \end{bmatrix}^T \tag{9}$$

where $g(h)$ depends on rocket altitude (h) and gravity acceleration on Earth surface $g_0(\varphi)$.

$$g(h) = \frac{g_0(\varphi)}{(1+h/R_0)^2} \tag{10}$$

where φ is latitude.

Rate of change of direction cosine matrix $\dot{\mathbf{C}}_b^s$ depends on angular rate of the body relative to spherical axis system in body axis system $\boldsymbol{\omega}_{sb}^b$.

$$\dot{\mathbf{C}}_b^s = \mathbf{C}_b^s\left(\boldsymbol{\omega}_{sb}^b \times\right) \tag{11}$$

where $\left(\boldsymbol{\omega}_{sb}^b \times\right)$ is skew symmetric matrix of $\boldsymbol{\omega}_{sb}^b$ which is function of angular rate in body axis system $\boldsymbol{\omega}_{ib}^b$.

$$\boldsymbol{\omega}_{sb}^b = \boldsymbol{\omega}_{ib}^b - \mathbf{C}_s^b\left[\boldsymbol{\omega}_{ie}^s + \boldsymbol{\omega}_{0s}^s\right] \tag{12}$$

Position of the rocket in basic axis system is defined by kinematic velocity of the rocket in spherical axis system.

$$\begin{bmatrix} \dot{x} & \dot{y} & \dot{h} \end{bmatrix}^T = \begin{bmatrix} \dfrac{v_{x_S}}{1+\dfrac{h}{R_0}} & \dfrac{v_{y_S}}{1+\dfrac{h}{R_0}} & -v_{z_S} \end{bmatrix}^T \tag{13}$$

2.2 Mathematical model of the accelerometer and rate gyro measurements error

Specific forces $\mathbf{f}^b$ and angular rates ($\boldsymbol{\omega}_{ib}^b$) of the rockets are measured by accelerometers and rate gyros. The outputs of the accelerometers ($\mathbf{f}_{\text{acc}}$) and rate gyros ($\boldsymbol{\omega}_{\text{r.g}}$) can be expressed mathematically in terms of the input values and errors of measurements (Fig. 5) [9].

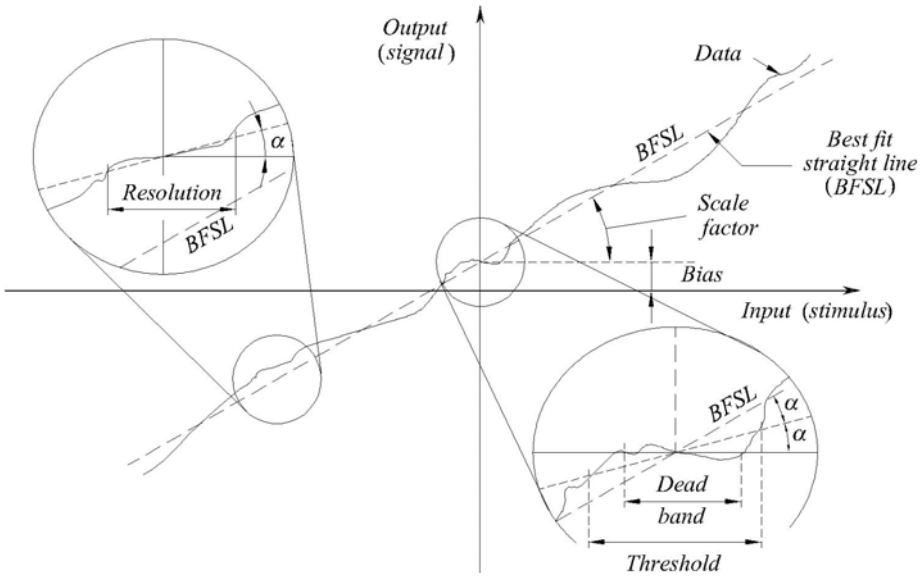

Figure 5. Measurement model

If cross-coupling coefficients and vibro-pendulous coefficients are neglected, the simplified mathematical model of measurements are function of scale factor ($\mathbf{S}$), residual fixed bias ($\mathbf{B}$), random bias error ($\mathbf{n}$) and noise ($\mathbf{w}$).

$$\mathbf{f}_{\text{acc}} = (\mathbf{I} + \mathbf{S}_{\text{acc}})\mathbf{f}^b + \mathbf{B}_{\text{acc}} + \mathbf{n}_{\text{acc}} + \mathbf{w}_{\text{acc}} \tag{14}$$

$$\mathbf{f}_{\text{acc}} = \mathbf{w}_{\text{acc}} \text{ for } \mathbf{f}_{\text{acc}} < \mathbf{f}_{\text{d.b}} \tag{15}$$

$$\boldsymbol{\omega}_{\text{r.g}} = (\mathbf{I} + \mathbf{S}_{\text{r.g}})\boldsymbol{\omega}_{ib}^b + \mathbf{B}_{\text{r.g}} + \mathbf{n}_{\text{r.g}} + \mathbf{w}_{\text{r.g}} \tag{16}$$

$$\boldsymbol{\omega}_{\text{r.g}} = \mathbf{w}_{\text{r.g}} \text{ for } \boldsymbol{\omega}_{\text{r.g}} < \mathbf{w}_{\text{d.b}} \tag{17}$$

where $\mathbf{f}_{\text{d.b}}$ - dead band of the accelerometers and $\mathbf{w}_{\text{d.b}}$ - dead band of rate gyros. For compensated accelerometers and rate gyros residual fixed bias is equal zero ($\mathbf{B}_{\text{acc}} = 0$, $\mathbf{B}_{\text{r.g}} = 0$).

The calculated values of the acceleration $\mathbf{f}_{\text{acc}}$ (14) and angular rates $\boldsymbol{\omega}_{\text{r.g}}$ (16) must be included in navigation algorithm in order to analyze influence of the IMU measurement errors to the estimation of the missile position and velocity. The specific force $\mathbf{f}^b$ in (8) is replaced by $\mathbf{f}_{\text{acc}}$ and angular rate in body axis system $\boldsymbol{\omega}_{ib}^b$ in (12) is replaced by $\boldsymbol{\omega}_{\text{r.g}}$.

$$\mathbf{f}^s = \mathbf{C}_b^s(\psi, \theta, \phi)\,\mathbf{f}_{\text{acc}} \tag{18}$$

$$\boldsymbol{\omega}_{sb}^b = \boldsymbol{\omega}_{\text{r.g}} - \mathbf{C}_s^b\left[\boldsymbol{\omega}_{ie}^s + \boldsymbol{\omega}_{0s}^s\right] \tag{19}$$

3. Parameters of IMU Measurment Errors

Inertial measurement unit (IMU) consists of three mutually perpendicular gyroscopes and three mutually perpendicular accelerometers. The increased accuracy of IMU based on MEMS technology permits to use them in guidance system of the ground-to-ground missile.

Investigation of the possibility to use low cost IMU based on MEMS technology for ground-to-ground missile guidance system requires determination of the IMU measurement errors to the missile impact point dispersions.

The low cost IMU Analog Device ADIS 16365 is taken as representative for analysis of ground-to-ground missile impact point dispersion due to IMU measurement errors. The gyroscopes measurement range are $\pm 300\,^{\circ}/s$ and accelerometers measurement range are $\pm 10g$. The shock survivability of this device is $2000g$. Considering accelerations and angular rates of the ground-to-ground missile, this type of IMU can not be used for measurement of the axial acceleration of the missile. Axial acceleration of the missile can be done by single accelerometer with higher range of measurement ($50g$).

The catalog characteristics of the IMU Analog Device ADIS 16365 are verified in labarotary in order to define measurement errors [8]. Measurements of the ADIS16365 sensor parameters are done on two-axis test table CARCO T-922 with following characteristics: minimum angular rate $0.0001\,^{\circ}/s$, maximum angular rate $999\,^{\circ}/s$, velocity resolution $0.0001\,^{\circ}/s$, position accuracy 0.0001° and position resolution 0.0001°.

3.1 Random bias instability

Two methods, Allan variance and Power spectral density, are used to determine velocity random walk and bias instability of the Analog Device ADIS 16365 gyroscopes and accelerometers [8]. It is shown that the better results, close to the catalog values, are obtained by Allan variance method.

Random bias instability of the accelerometers ($\mathbf{n}_{\text{acc}}$) and rate gyros ($\mathbf{n}_{\text{r.g}}$) are determined from diagram of Allan variance. Diagram of the standard deviation of Allan variance of the measured specific force f_x for three sampling rates $\Delta t = 0.01, 0.1, 3.6\ s$ and of the measured angular rate ω_x for four sampling rates $\Delta t = 0.01, 0.1, 1.0, 3.6\ s$ are given in Fig. 6.

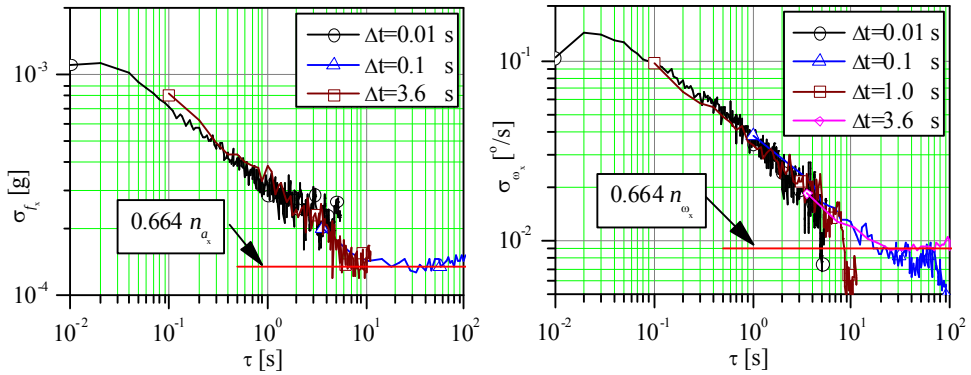

Figure 6. Standard deviations of accelerations and angular rates along x axis

The similar diagrams are obtained for the other two accelerometers and rate gyros of the Analog Device ADIS 16365. The 0.664 of the bias instability value is equal to the stationary value of the standard deviation at higher sampling rates. The bias instability of the Analog Device ADIS 16365 accelerometers and rate gyros are given in Table 1.

Table 1

Axis	Accelerometers	Rate gyros
	$n_{acc}\ [g]$	$n_{rg}\ [^\circ/s]$
x	0.00021	0.0135
y	0.00031	0.0105
z	0.00026	0.0121

3.2 Output noise

The noise of the accelerometers and rate gyros are determined from the measured specific forces and angular rates for zero demanded values. Diagrams of the measured specific forces and angular rates along x axis with sampling interval 10 *ms* are given in Fig. 7.

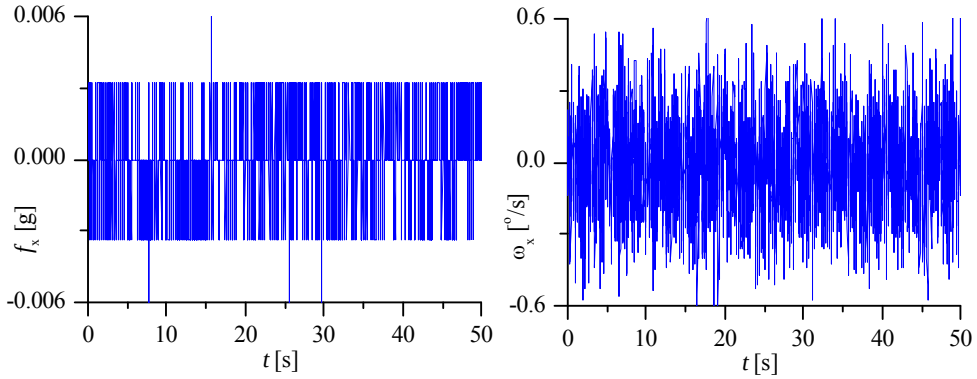

Figure 7. Measured specific forces f_x and angular rates ω_x for zero demanded values

Standard deviations (σ) of the all IMU accelerometers and rate gyros noise (Table 2) are calculated by formula $\sigma = \sqrt{\sum_{i=1}^{N}\left(x_i - \overline{x}\right)^2 \Big/ \left(N-1\right)}$ where x_i is measured values, N is number of measured values and $\overline{x} = \sum_{i=1}^{N} x_i \Big/ N$ is mean values of the measurements.

Table 2

Axis	Accelerometers	Rate gyros
	σ_{acc} [g]	σ_{rg} [°/s]
x	0.001613	0.191961
y	0.002193	0.169030
z	0.002130	0.190003

3.3 Dead band

Dead band of the accelerometers ($\mathbf{f}_{d.b}$) and rate gyros ($\mathbf{w}_{d.b}$) are determined from the diagram of the measured specific forces and angular rates in function of required specific forces and required angular rates. The diagrams of the measured specific forces in function of required specific forces and measured angular rates in function of required angular rates along x axis with designated area of dead band are given in Fig. 8.

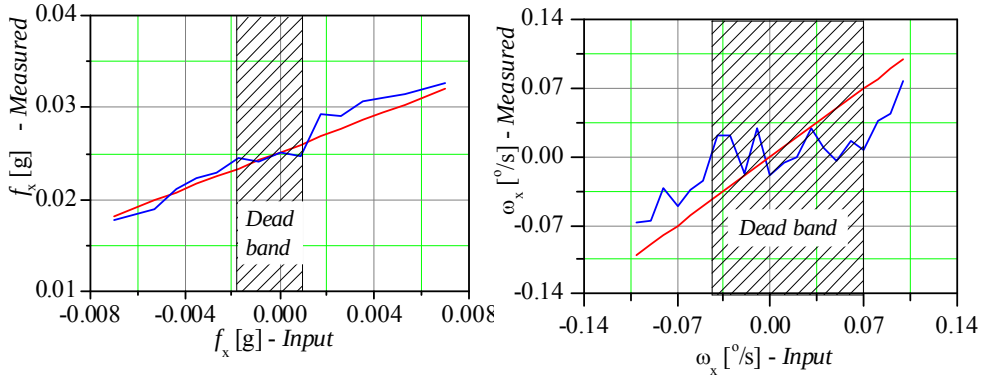

Figure 8. Dead band of accelerometer and rate gyro

Applying the same procedure all three IMU accelerometers and rate gyros, the determined dead band are given in Table 3.

Table 3

Axis	Accelerometers	Rate gyros
	$f_{db}\,[g]$	$n_{rg}\left[^{\circ}/s\right]$
x	-0.0017 ÷ 0.00087	-0.05 ÷ +0.07
y	-0.0052 ÷ 0.0052	-0.09 ÷ +0.07
z	-0.0035 ÷ 0.00698	-0.05 ÷ +0.07

4. Numerical simulation

In order to verify the influence of the IMU accelerometers and rate gyros measurement errors to the accuracy of the ground-to-ground missile guidance system, the complex software for missile guidance is built. It is composed of following modules: 6 DOF mathematical model of the missile flight, SDINS navigation algorithm, and mathematical model of the IMU measurement errors, guidance system of the ground-to-ground missile with lateral acceleration autopilot in the inner loop and CEP calculation of the impact points dispersion by Monte Carlo simulation.

The most dominant external disturbances (thrust deviation, thrust excentrity and wind) are considered for analysis of the guidance system accuracy:

- Variation of the thrust has normal Gaussian distribution low $\mathcal{N}(F_N, \sigma(F))$ where $\sigma(F)/F_N = 0.5\%$,
- Variation of the thrust excentrity magnitude (ε_F) has normal normal Gaussian distribution low $\mathcal{N}(0, \sigma(\varepsilon_F))$. Usual value of $\sigma(\varepsilon_F) = 1.0\,mrad$. Angular position

of the lateral thrust has uniform distribution $\varphi_{\varepsilon_F} = U(0, 2\pi)$ in the plane normal to the longitudinal axis,

– Axial and lateral wind has normal distribution $\mathcal{N}(0, \sigma_w)$ with zero mean values and standard dispersion $\sigma_{w_x} = \sigma_{w_y} = 1.0\ m/s$.

Without loosing generality of the problem it is taken that the parameters of accelerometers and rate gyros measurements are the same for all three axis (Table 4).

Table 4

	Accelerometer	Rate gyros
Scale factor	$s_{acc} = 0.1\,\%$	$s_{r.g} = 0.1\,\%$
Random bias instability	$n_{acc} = 0.002\ mg$	$n_{rg} = 0.008\ ^\circ/s$
Noise	$\sigma_{acc} = 9.0\ mg$	$\sigma_{rg} = 1\ ^\circ/s$
Dead band	$f_{d.b} = 0.005\ mg$	$\omega_{d.b} = 0.07\ ^\circ/s$

It is shown in [7] that ground-to-ground missile guidance system can compensate all external disturbances without miss of the target. In order to verify the influence of IMU measurement errors to the missile trajectory parameters estimation and to the guidance system accuracy, the numerical simulation of the guided ground-to-ground missile is done with IMU measurement error parameters (Table 4) and without external disturbances. The impact points dispersion of the guided ground-to-ground missile at the range of $40.0\,km$ with IMU measurement errors only (Fig. 10) is obtained by Monte Carlo simulation of 100 trajectories.

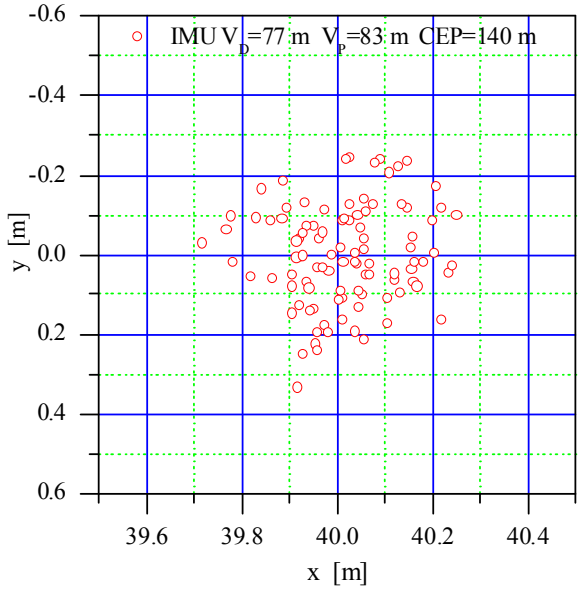

Figure 10. Impact point dispersion due to IMU measurement errors

When the external disturbances are included in numerical simulation the impact points dispersion are equal to the impact points dispersion due to errors IMU measurement unit (Fig. 11).

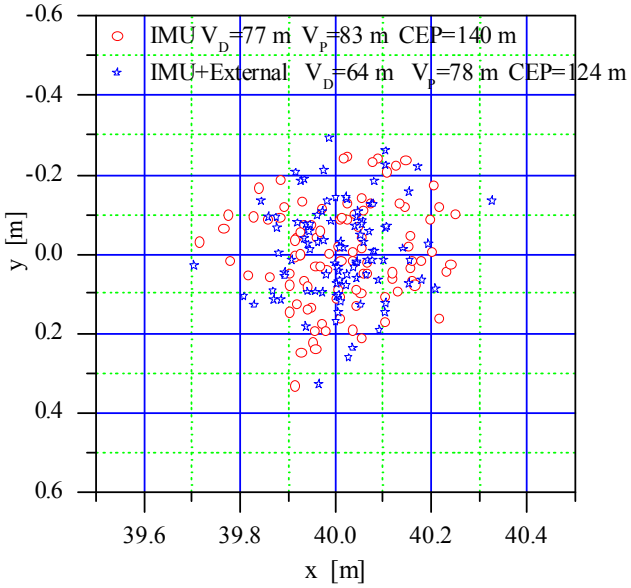

Figure 11. Influence of the external disturbances to the impact points dispersions

Efficiency of the ground-to-ground missile guidance system with IMU ADIS16365 is obtained by comparing impact points dispersion of the guided surface-to-surface missile relative to the impact points dispersion of the unguided ballistic flight with the same external disturbances (Fig. 12)

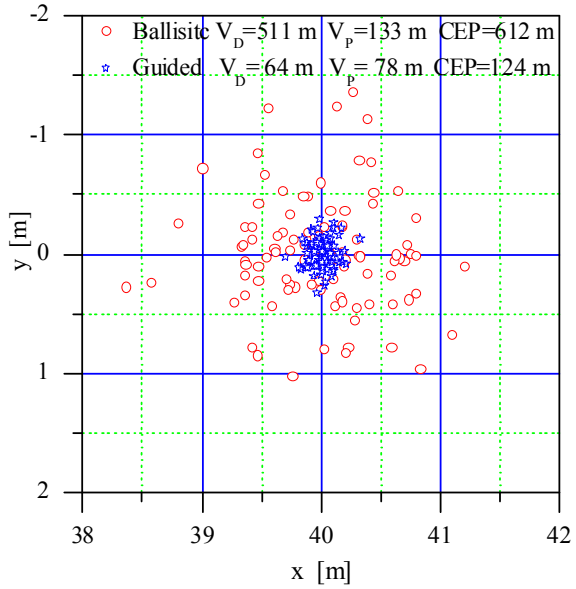

Figure12 Impact points dispersion of due to external disturbances

5. Conclusion

The guidance law of the ground-to-ground missile guidance system is based on the deviation of the actual trajectory from nominal ballistic trajectory. In order to estimate missile trajectory parameters the navigation algorithm in spherical axis system is developed with assumption that specific forces and angular rates of the missile in body axis system is known. Since the specific forces are measured by accelerometers and angular rates by rate gyros, the accelerometers and rate gyros measurement errors are modeled as a function of the scale factor, bias instability, dead band and noise. These measurement parameters for commercial IMU ADIS16365 are determined in laboratory.

Efficiency of the surface-to-surface missile guidance system with commercial IMU ADIS16365 is analyzed by numerical simulation. It is shown that IMU measurement errors are dominant for impact point dispersion of the guided surface-to-surface missile. There is no practical influence of the external disturbances to the impact points dispersion.

It is also shown that the guidance system of the ground-to-ground missile with commercial IMU ADIS16365 can increase accuracy by five times relative to the ballistic missile of the same range.

References

[1] Gregor Gregoriou (1988) CEP Calculation for a Rocket with Different Control System, *J. Guidance*, Vol. 11, No. 3, May-June.
[2] A.E. Gamble, P.N. Jenkins: Low Cost Guidance for the Multiple Launch Rocket System (MLRS) Artillery Rocket, *IEEE AES System Magazine*, January 2001.
[3] Siouris,M.G (2004) *Missile Guidance and Control Systems*, Springer-Verlag, New York.
[4] Ćuk D., Mandić S. (2006) Guidance and Control Laws Design, *Theoretical Manual*, MTI, Belgrade.
[5] Mandić S (2009) Guidance of Ground to Ground Rockets Using Flight Path Steering Method, *Scientific Technical Review*, Vol.LIX, No.3-4, Belgrade, pp. 3-11.
[6] Garnel P (1980) *Guided Weapon System*, Pergamon Press, New York.
[7] Blakelock,J.H. (1991) *Automatic Control of Aircraft and Missiles*, John Willy and Sons.
[8] Ćuk D., Ćurčin M., Mandić S. (2004) Autopilot Design, *Theoretical Manual*, MTI, Belgrade.
[9] D.H. Titterton, J.L.Weston (2009) *Strapdown Inertial Navigation Tehnology*, American Institute of Aeronautics and Astronautics, Inc, 2009.
[10] Ćuk D. (2008) GMTC-6D, *Theoretical Manual*, MTI, Belgrade.
[11] Vukmirica V., Trajkovski I., Asanović N., 2010, Two Method for Inertial Seneors Parameters Determination, *Scientific Technical Review*, Vol.LX, No.3-4, pp., ISSN 1820-0206, Belgrade
[12] Six Degrees of Freedom Inertial Sensor ADIS16360/16365, ANALOG DEVICES.
[13] IEEE Std 528-1994, IEEE Standard for Inertial Sensor Terminology, IEEE 1994.
[14] IEEE Std 1293-1996, IEEE Standard Specification Format Guide and Test Procedure for Linear, Single –axis, Nongyroscopic Accelerometers, IEEE 1996.

THE OPTIMIZATION OF LAUNCHING CADENCES FROM SELF-PROPELLED MULTIPLE LAUNCHERS

Milan Milošević[1], Dragoslav Živanić[2], Vlado Đurković[3]

[1] Military Technical Institute, Belgrade,
Ratka Resanovića. 1, Belgrade
e-mail: marija.m@beotel.net
[2] Military Technical Institute, Belgrade,
Ratka Resanovića. 1, Belgrade
e-mail: dragoslav@ptt.rs
[3] Military Academy,Belgrade,
Pavla Jurišića Šturma 33, Belgrade
e-mail: svskom@scnet.rs

Abstract. Based on mechanical and mathematical model of missile launcher, the influential parameters which launcher device transmits to the wrap-around cruciform unguided missile at the moment of leaving the launching tube were analyzed in this paper. The ballistic module for determining firing elements based on six degrees of freedom motion was presented. The launcher displacements were taken as initial conditions for the missile flight. The analysis of optimization of the launching cadence and dispersion of the hits, at the place of the target, was shown in this paper. It was also shown the partial CEP due to the interaction launcher – missile, for the multiple missile launcher BM-21.

Key words: missile launcher, missile, missile dispersion, oscillation, trajectory.

1. Introduction

The development of missile systems, both in history and in the new era, the missile has always been at the center of attention, and all other elements of the system were neglected and stayed in the background. Only after the appearance of multi tubes "Katyusha", on the battlefield of the Second World War, the perception had changed and come to affirm the launcher as a weapon, we can see their significant role in achieving efficiency. Scientifically and by experiments it was proved that the accuracy and precision of unguided missiles can be quite close to conventional systems, with a perspective to reach this level. A prerequisite for this is the equal study of the entire missile system in which launchers have an important role.

2. Mechanical- mathematical model of missile launcher

Mechanical model of multi tubes missile launcher displayed on the Fig.1 that is suggested, consists of stiff bodies (point mass) and deformable elastic damping elements with connections reference [1,3,4]. The mechanical model of missile launcher presents the launcher missile that consists of special purpose vehicles (position 1), launcher device

(position 2), the device for elastic system disconnection (position 3), the traversing mechanism and the elevating mechanism (position 4) and ammunition (missiles) (position 5). The bearing or the lower part of the vehicle and the vehicle frame has two longitudinal reinforced box profile fixed with the cross elements of great stiffness. The system for the elastic disconnection of the vehicle is detached to the frame of the vehicle and it consists of four legs supported on the ground. Legs are represented as the elastic damping support, the stiffness of the springs equals the reduced stiffness of support and ground.

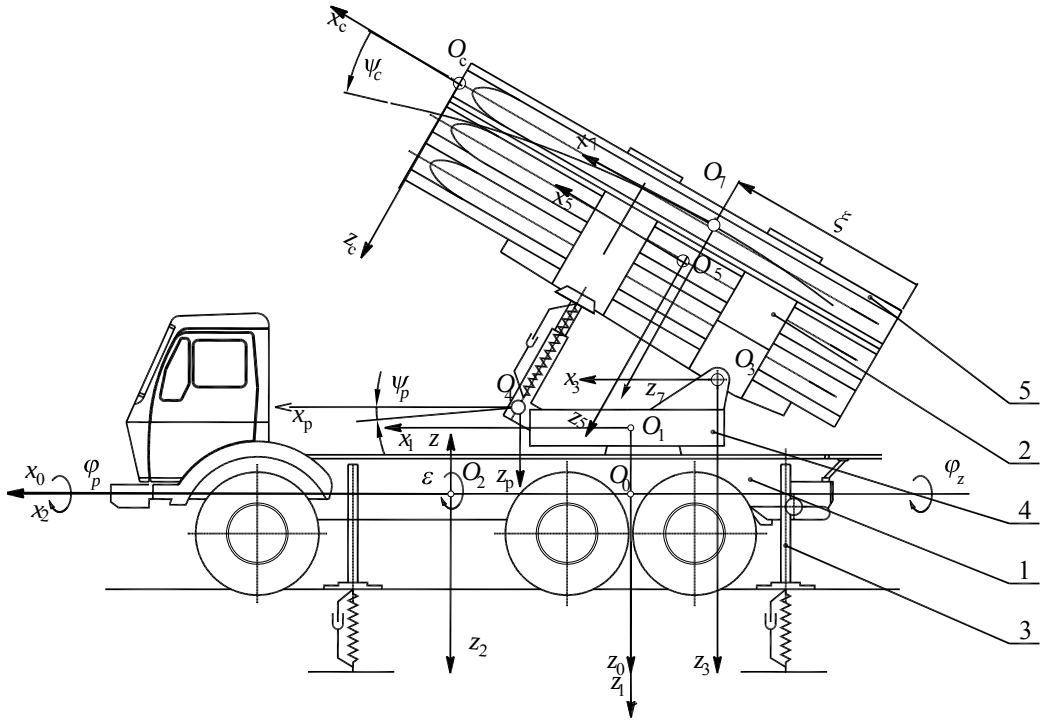

Fig. 2 - Mechanical model multi tube missile launcher

According to the given model missile launcher, during the movement of the missile in the tube and after its release we define the displacement from eight generalized coordinates:

- z - vertical displacement of the vehicle frame,
- ε - rotation of the vehicle frame around transversal axis,
- φ_z - rotation of the rear part of the frame around longitudinal axis,
- φ_p - rotation of the front part of the frame around longitudinal axis,
- ψ_p - the angle move of the elevation support due to the bending of direction console,
- θ - rotation of the launcher around the rotational axis of the device elevation,
- ψ_c - angle displacement of the muzzle launcher tube and tube due to the bending and

- ξ - movement of missile in launcher tube during firing.

2.1. The kinetic energy of self-propelled missile launcher

It is accepted that the model of the self-propelled multiple missile launcher has the following characteristics: it is non-conservative i.e. its work is accompanied by dissipation of energy, all the constraints are holonomic i.e. finite and with no derivate, stationary, does not depend on the time except in the case of this analysis in movement disorders of missile through the tube and the ideal-that is delayed i.e. the sum of all the works of reactive power on a virtual displacement is zero.
The elasticity of missile, internal friction in the bearings and construction, the gaps in gearboxes and other power transmission, torsional oscillations of a launching device horizontal and undercarriage are neglected, as it is considered that those are the sizes of the second order.
Kinetic energy of the system is represented as the sum of the kinetic energy of vehicles and the kinetic energy of a launching device with missiles.

2.1.1. The kinetic energy of vehicle

The kinetic energy of the vehicle, on which the launch facility is built, is equal to the sum of kinetic energy components and it is represented

$$E_{kV} = \frac{1}{2}\left[m_1 v_1^2 + J_{1x_1}\dot{\varphi}_z^2 + J_{1y_1}\dot{\varepsilon}^2 + m_2 v_2^2 + J_{2x_2}\dot{\varphi}_p^2 + J_{2y_2}\dot{\varepsilon}^2 + m_4 v_4^2 \right]. \quad (1)$$

where:

m_1 – mass of the rear of the vehicle with the leveling mechanism, the lower part of the direction and elevation,

m_2 – mass of the front part of the vehicle,

m_4 – mass of consoles of the moving part of the direction i.e. of the cradle,

J_{1x}, J_{1y} – principal central moment of inertia of the rear of the vehicle and associated components,

J_{2x}, J_{2y} – principal central moment of inertia of the front part of the vehicle,

2.1.2. The kinetic energy of a launching device

With the kinetic energy of pipes we assume that only the tube nosing out the front panel participates in the moving while the parts of the tube between the boards and back behind the rear panel do not participate in the movement so the kinetic energy of the tube is reduced to the top tube. This assumption can be taken with sufficient reliability since the barrels are much more rigid between the front and back panel of the launching device.

$$E_{kLU} = \frac{1}{2}\left[\begin{array}{l} m_R v_R^2 + J_{Rx_7} p^2 + J_{Ry_7} q^2 + J_{Ry_1}\dot{\varepsilon}^2 + J_{Ry_3}\dot{\theta}^2 + J_{Rx_1}\dot{\varphi}_z^2 + \\ m_5 v_5^2 + J^*_{5x_1}\dot{\varphi}_z^2 + J^*_{5y_1}\dot{\varepsilon}^2 + J_{5y_3}\dot{\theta}^2 + m_6 v_6^2 \end{array} \right] \quad (2)$$

where:

m_5 – current mass of launching device (empty launching device and missile that do not move)

m_6 – mass of front part tube (console part),

m_R – missile mass,

J_{5x}^*, J_{5y}^*, J_{5y} – principal central moment of inertia of a launching device,

J_{Rx}, J_{Ry} – principal central moment of inertia of the missile,

v_1, v_2, v_4, v_5, v_6 – absolute speed of the corresponding points (concentrated masses),

v_R – axial speed of the missile,

$\dot{\varphi}_z$ – angular speed of the rear of the vehicle and components around its longitudinal axis of inertia, O_1y_1,

$\dot{\varphi}_p$ – angular velocity of the front of the vehicle around its longitudinal axis of inertia, O_2y_2,

$\dot{\varepsilon}$ – angular velocity of the vehicle around its transverse axis of inertia, O_1x_1,

$\dot{\theta}$ – angular velocity launching device around the rotational axis of elevation, O_3x_3,

p – spin of missile (angular velocity around the longitudinal axis O_7x_7),

q – pitch rate (angular velocity around the horizontal axis O_7y_7)

2.2. Potential energy of the missile launcher

The potential energy of a given mathematical mechanical model Multiple Barrel Missile Launcher is the sum of potential energy of the vehicle and a launching device.

According to the given mathematical model, all mass in the position of static equilibrium are balanced with elastic forces in the spring, so the differential equations of motion will be placed on the equilibrium position.

2.2.1 Potential energy of vehicle

Potential energy of the vehicles can be seen as the sum of potential energy of legs and frame of the vehicle.

- *Potential energy of the legs and support surfaces*

The proposed mathematical mechanical model consists of four legs and the potential energy will be presented

$$E_{pSP} = \frac{1}{2}\left[c_{11}\left(\lambda_{11} + p_{11}\right)^2 + c_{12}\left(\lambda_{12} + p_{12}\right)^2 + c_{21}\left(\lambda_{21} + p_{21}\right)^2 + c_{22}\left(\lambda_{22} + p_{22}\right)^2 \right] \tag{3}$$

with:

$c_{ij}\left(i, j = 1,2\right)$ - reduced stiffness of legs and support surfaces,

$\lambda_{ij}\left(i, j = 1,2\right)$ - static strain of legs and support surfaces,

$p_{ij}\left(i, j = 1,2\right)$ - reduced dynamic strain of legs and support surfaces,

Reduced dynamic strain of legs and support surfaces according to the [7] can be represented

$p_{11} = z_1 + l_1\varepsilon - l_3\varphi_z$, $p_{12} = z_1 + l_1\varepsilon + l_3\varphi_z$,

$$p_{21} = z_1 - l_2\varepsilon - l_4\varphi_p \,,\; p_{22} = z_1 - l_2\varepsilon + l_4\varphi_p \,. \tag{4}$$

- *The potential energy of the vehicle frame*

Frame of vehicle (reinforced chassis of vehicle) is discretized with two masses and is represented as a torsion beam with reduced torsion stiffness c_φ and moving mass (m_1, m_2) for angular φ_z, φ_p . So the potential energy of the frame can be represented

$$E_{PR} = \frac{1}{2} c_\varphi \left(\varphi_z - \varphi_p\right)^2 \tag{5}$$

2.2.2. Potential energy of the launching device

Potential energy of a launching device can be viewed as the sum of potential energy of the console of the upper frame direction, elevation, leveling mechanisms and tube deformation from which missiles are fired.

- *Potential energy of the movable frame of mechanisms direction*

Rotating frame direction so-called cradle direction participate in the potential energy with its console and its bending angle ψ_4 . Bending stiffness of the cradle console is marked with c_3 . Potential energy is shown in next equation,

$$E_{PK} = \frac{1}{2} c_3 \psi_4{}^2 \,. \tag{6}$$

- *Potential energy mechanisms of elevation*

Potential energy of the mechanism of elevation i.e. the mechanism for operating a launching device according to the height determined from the deformation of a triangle whose two nods represent the connection of the pickup device with the cradle and the launcher and the third nod represent the rotational point of the elevation of the launching device. Tensile or compression of the stick elevation of stiffness c_4 can be written as $\Delta l = e\theta + d\psi_4$ where θ and ψ_4 represent the change of the angle of elevation and the bending angle of the console cradle. Potential energy is represented by

$$E_{PE} = \frac{1}{2} c_4 \left(e\theta + d\psi_4\right)^2 \tag{7}$$

- *Potential energy of the tube deformation*

As it was assumed that the most important muzzle tube i.e. the tube overhang in front of the front panel, potential energy of the tube can be written

$$E_{pC} = \frac{1}{2} c_5 \psi_6^2 \tag{8}$$

where the c_5 and ψ_6 are the stiffness i.e. the angular deformation of the muzzle tube

2.3. Differential equations of the missile launcher oscillations

For the deduction of the differential equations that describe the oscillation of missile launcher it was used the Lagrange equations of the second order whose general form is shown in equation

$$\frac{d}{dt}\left(\frac{\partial E_k}{\partial \dot{q}_r}\right) - \frac{\partial E_k}{\partial \dot{q}_r} + \frac{\partial E_p}{\partial q_r} = Q_r^n \,. \tag{9}$$

where: E_k - the kinetic energy of the systems, E_p - the potential energy of the system, Q_r^n - generalized non-conservative force, q_r - generalized coordinates and $\dot{q}_r$ - generalized velocity, $r = 1, 2, 3...n$ generalized coordinates, i.e. number of degrees of freedom with which this system is represented here and it is 8 as defined in the previous point.
So the mathematical model of the system of eight no homogeneous, nonlinear differential equations of the second-order. In matrix form the system can be presented according to equation:

$$\mathsf{A} \cdot \ddot{\mathbf{q}} + \mathsf{B} \cdot \dot{\mathbf{q}} + \mathsf{C} \cdot \mathbf{q} = \mathsf{D}, \qquad (10)$$

Where the corresponding matrices A, B, C and D functions of the generalized coordinates and velocity.
Matrix A is the matrix of inertia, matrix B is damping matrix, matrix C is stiffness matrix and matrix D is the matrix of the perturbation.
Numerical analysis of this problem is performed for the concrete construction of missiles and missile launcher.
This system of differential equations is solved by the usage of the Runge –Kutta - Fehlberg with the software package LANS [5].

3. A mathematical model of missile flight

Equations of the missile motion in space with 6 degrees of freedom are discussed in various references and here is the model used by the reference [6]. In the deduction of the equations of motion of missile it is assumed that the missile is absolutely rigid and that the elastic oscillations of the body and wings are neglected. This assumption greatly simplifies the equations of motion as it allows the missile to be present in the form of ordinary differential equations. The assumption of infinite stiffness is permissible as the frequency of elastic oscillations is ten times larger than the frequency of the oscillations of missile as a rigid body. Missile with cruciform configuration, that is dealt with in this the paper has a central and axial symmetry and the symmetry of the same forms of penance and the mass distribution of certain elements of missile construction. In this case, the ellipsoid of inertia of missile becomes spheroid as the right axis of any coordinate system starting at the center of inertia of the missile, which as one of its axis has the axis of symmetry, are the main and central axis of symmetry.
To determine the position of missiles in space it is enough to know the change of coordinates of the center of inertia as a function of time and reverse of the missile in relation to the center of inertia. Next equations in matrix form define the movement of missile in space.

3.1 Translation of the center of inertia

Translational movement of the center of inertia can be displayed by

$$\begin{bmatrix} \Sigma F_x + F_{gx} \\ \Sigma F_y + F_{gy} \\ \Sigma F_z + F_{gz} \end{bmatrix} = m \begin{bmatrix} \dot{u} \\ \dot{v} \\ \dot{w} \end{bmatrix} + m \begin{bmatrix} 0 & -r & q \\ r & 0 & -p \\ -q & p & 0 \end{bmatrix} \begin{bmatrix} u \\ v \\ w \end{bmatrix} \qquad (11)$$

with:

ΣF_x, ΣF_y, ΣF_z - the sums of projections of external forces influencing the missile, such as aerodynamic and thrust along the axis *x*, *y* and *z* in a fixed coordinate system [N]

F_{gx}, F_{gy}, F_{gz} - the projection of the gravitational force along the axis x, y and z in a coordinate system related to [N]

$\dot{u}$, $\dot{v}$, $\dot{w}$ - acceleration along the axis x, y and z in a coordinate system related to [m/s^2],

u, v, w - velocity along the axis x, y and z in a coordinate system related to [m/s],

p, q, r - angular velocity along the axis *x*, *y* and *z* in a coordinate system related to [rad/s].

3.2 Rotation around the center of inertia

Rotation around the center of inertia can be shown

$$\begin{bmatrix}\Sigma M_x\\ \Sigma M_y\\ \Sigma M_z\end{bmatrix}=[J]\begin{bmatrix}\dot{p}\\ \dot{q}\\ \dot{r}\end{bmatrix}+\begin{bmatrix}0 & -r & q\\ r & 0 & -p\\ -q & p & 0\end{bmatrix}[J]\begin{bmatrix}p\\ q\\ r\end{bmatrix} \tag{12}$$

with:

$[J]=\begin{bmatrix}J_{xx} & -J_{xy} & -J_{xz}\\ -J_{yx} & J_{yy} & -J_{yz}\\ -J_{zx} & -J_{zy} & J_{zz}\end{bmatrix}$ - matrix moment of inertia of missiles,

ΣM_x, ΣM_y, ΣM_z - the sum of all external moments (of the thrust and aerodynamic forces) projected on the axis x, y and z in a coordinate system related to [Nm]

$\dot{p}$, $\dot{q}$, $\dot{r}$ - angular acceleration along the axis *x*, *y* and *z* in a coordinate system [rad/s^2],

J_{xx}, J_{yy}, J_{zz} - the main moments of inertia along the axes *x*, *y* and *z* in a coordinate system [kgm^2],

J_{xz}, J_{xy}, J_{yz} - centrifugal moments of inertia in [kgm^2].

3.3 The initial conditions for the missile flight

All disturbances to announce missile launch facility at the time of separation from the missile launch tubes are the initial conditions for further flight missiles. These initial conditions are derived from previously described mathematical model.

Initial conditions, the half bound coordinate system, the missile will perform at a time when missiles loses contact with the launch facility and they are:

t_0 - the time when missile leaves from launching tube,

$x_{0,}$ $y_{0,}$ h_0 - coordinates of center of gravity missile when missile leaves from launching tube,

V_0 - missile velocity when missile leaves the launching tube,

γ_0 - angle of inclination of the axis missiles towards the horizon when missile leaves the launching tube,

χ_0 - the angle of direction when missile leaves the launching tube,

α_0 - angle of attack when missile leaves the launching tube,

β_0 - slip angle when missile leaves the launching tube,

ϕ_0 - roll angle when missile leaves the launching tube,

$p_{0,}\ q_{0,}\ r_0$ - angular velocity around the axis x, y, z when missile leaves the launching tube.

Depending on the type of the start i.e. of the way of guiding the missile through the launch tube this moment in time without the contact is different. With classic multi tubes of launch device we have tip-off from tube and it is considered that it is the position when the missile leaves the muzzle tube. This term tip-off refers to the angular momentum acquired by a missile due to the action of gravity when the forward missile supports leave the launcher before the aft supports.

4. Numerical example MLRS BM-21 "Grad"

For the analysis the self-propelled multiple missile launcher MLRS BM-21 "GRAD" [8] was selected. Launching device is filled with 40 missiles. The trajectory of which are elements of fire is analyzed:

- angle of elevation $\alpha_0 = 30^\circ$
- angle of direction $\theta = 90^\circ$ and
- without brake ring

from which the range $D = 17740\ m$ is derived.

4.1. Inertial and geometric characteristics MLRS BM-21 "Grad"

Mass and geometric interpretation is given in Fig. 2

a = 2500 [mm].
l_1 = 1200 [mm].
l_2 = 2600 [mm].
l = 3800 [mm].
d = 200 [mm].
b = 800 [mm].
e = 1400 [mm].
f = 600 [mm].
c = 800 [mm].
l_3 = 500 [mm].
l_4 = 1000 [mm].

m = 13800 [kg] - total weight BM-21 122mm filled with 40 missiles,
m_1 = 5800 [kg] - mass of the rear of the launcher,
m_2 = 8000 [kg] - mass of the front of the launcher,
m_4 = 300 [kg] - mass of console of cradle,
m_5 = 4500 [kg] - mass of filled launching device,
m_5' = 1500 [kg] - mass of empty launching device.

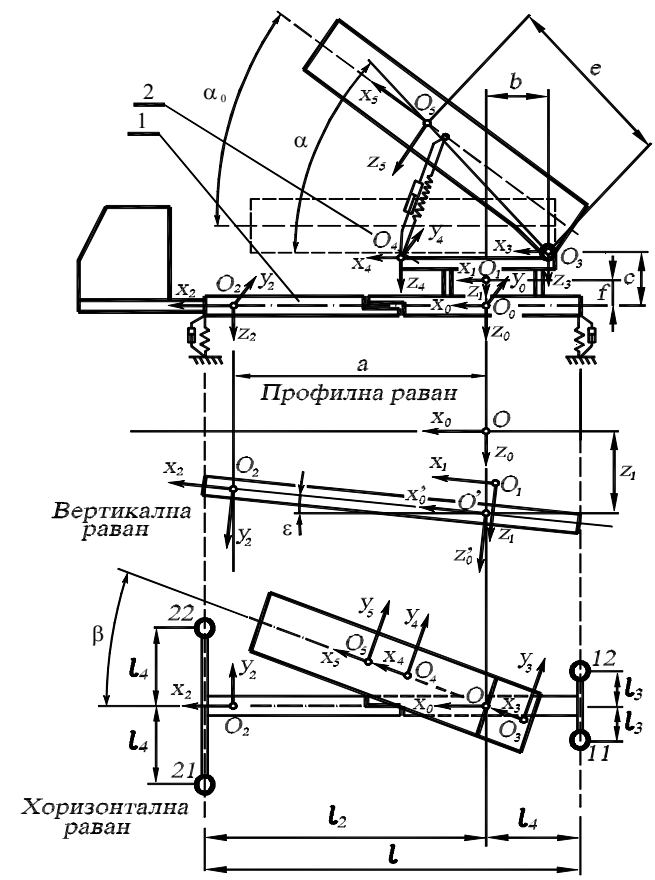

Fig. 2 - Geometric interpretation of a launching system BM-21 122mm

5. Analysis of launcher oscillations and impact point missiles at the target

5.1. Analysis of burst firing

By solving the system equation (10) for numerical example the displacement and velocity oscillation missile launcher are obtained. The diagram Fig.3 shows the second period of free oscillation of vertical missile launcher after firing the first missile (curve line h_L). This period lastes from 0.9 [s] to 1.4 [s]. On the same curve line, squares mark the time of the firing of the second missile, and they are: t_L = 0.94, 1.05; 1.1; 1.14; 1.17, 1.2, 1.23, 1.3, 1.33, 1.4 [s].
Time moments of the second missile firing were chosen for the following cases:

- when the launch tube displacement equals zero $h_L = 0$,

- extreme values of displacements (the minimum and maximum) of the muzzle launching tube and
- the mean displacement of the launch tube between the zero displacement and the extreme positions.

The range missiles have been calculated by the usage of program (PUTNPV3) based on a model missile flight with 6 degrees of freedom [4].

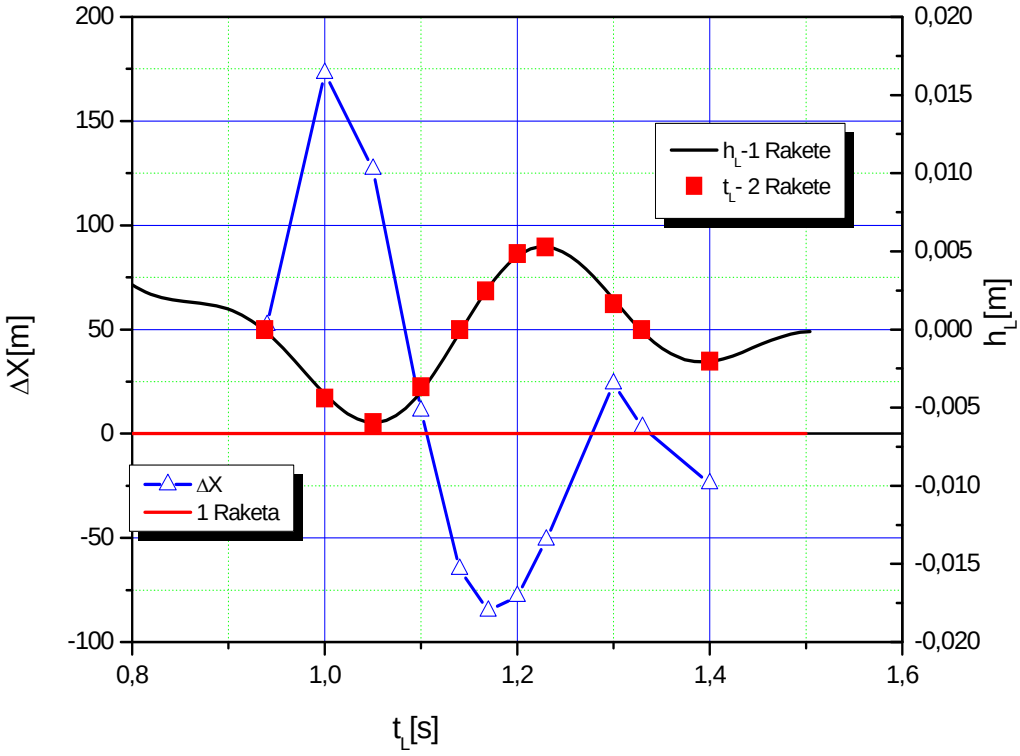

Fig.3 The second period of oscillation of launchers after firing the first missile

The second curve on the same diagram Δx (marked with triangles) represents the difference range of the second missile comparing to the first missile range.

The range of the second missile was obtained after ingestion of a new initial disturbances that missile launcher announces to another missile in the selected point in time.

For initial disturbances of missile were taken disturbances that missile launcher announces at the muzzle in this model those are:

- the initial angle of attack α_0
- initial angular velocity missile (pitch rate) q_0, and
- change the initial angle of launch γ_0.

The diagram Figure 4 shows the path end at the target of the first missile, and every second missile that was fired at different instants from $t = 0.94 - 1.33s$. The diagram shows that the second missile reaches 17,655 to 17,913 m. It also shows that for $t_L = 1.0; 1.3; 1.33\ s$, the second missile has a minimum distribution comparing to the first missile. Firing of the second and each subsequent missile should be chosen for one of these three times.

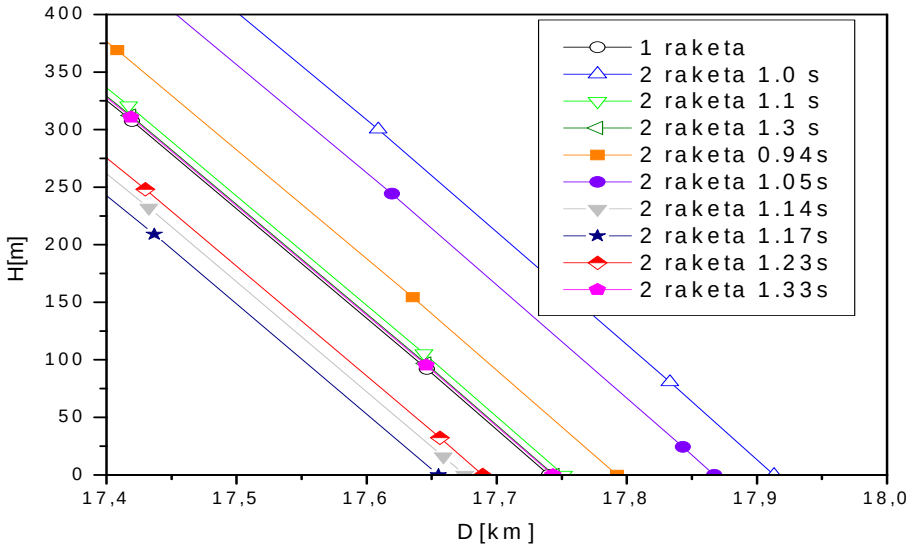

Fig.4 The ends of the path 2. missile

The diagram Fig.5 shows three groups of graphics:

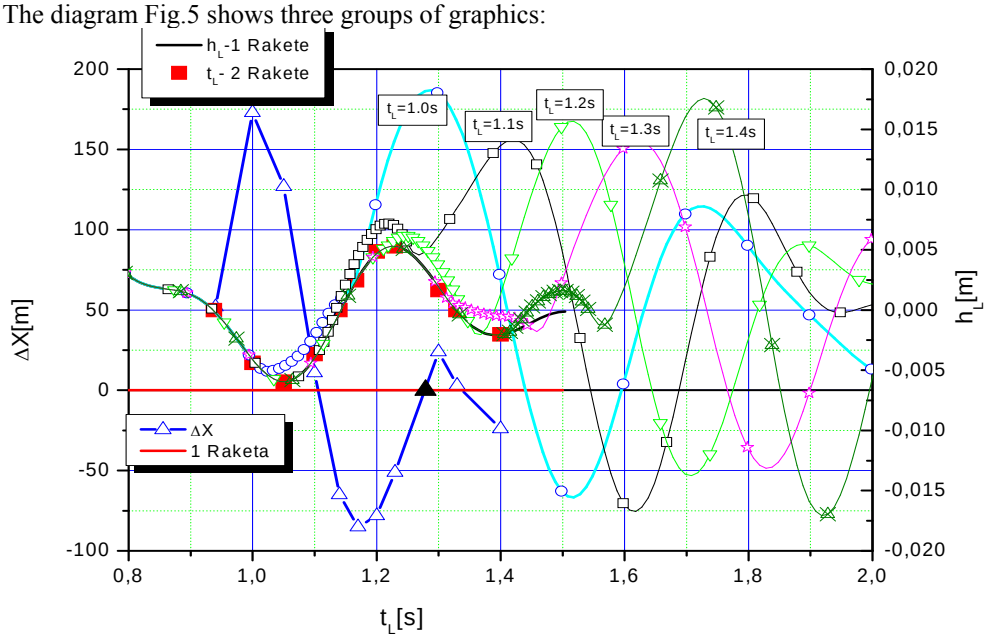

Fig.5 The movements and distribution of the launcher to the firing 2. missile

1 - The line oscillation of launchers after firing the first missile h_L , is given and time-tested the second missile firing moments are marked on it. Moments of time firing the second missiles have been selected when moving of the launchers are zero, maximum, minimum and mean between zero and extremes.

2 - The differences in range of the second missiles Δx compared to the first range missiles as a function of time t_L are shown. The same diagram shows that the range of variation is zero at points t_L = 1.106 and 1.279 s. From the point of zero deviation range missile in the target it might be the time to launch the second missile.
3 - The third group are the curves representing the vertical displacement launch tube after the firing of the second missile.

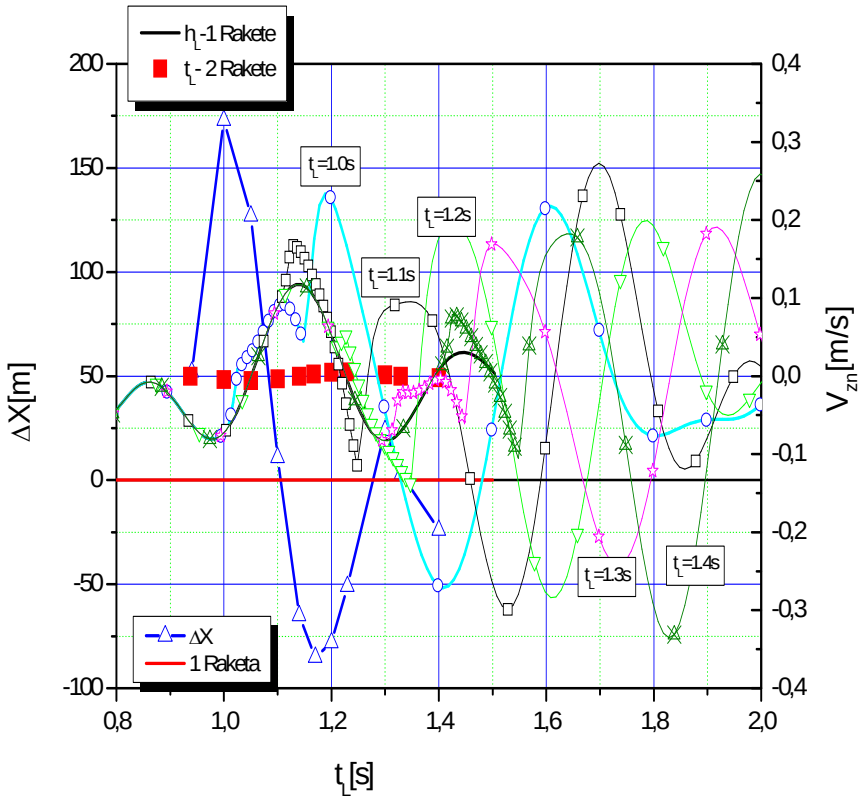

Fig.6 Velocity of muzzle tube and of the missile impact point distribution on target to the firing 2. missile

The diagram Fig.6 shows the speed of the muzzle tube moving normal to the axis of tube.
For the analysis of the second period of oscillation launcher after firing the first missile is selected because the displacement and velocity of the muzzle tube (Fig.5 and Fig.6) are lower than in the first periods of oscillation.
Firing of the second missile is shown after $t_L = 0.9\,s$. We can see that the maximum deviation range is up to 175m at the range of 17740m. Maximum speed of oscillation of the muzzle tube equals 0.3 m/s.

5.2. Partial CEP of missile dispersion on the target

Circular error probable (CEP) is the most widely used measure of dispersion for determining missile accuracy for two-dimensional distribution. The CEP is defined as the

radius of a circle within which one-half of the values are expected to fall. The center of the circle is the mean of the values.

The diagram shows in Fig.6 CEP hits on the target, as a result of the interaction missile-launcher, and is 59.5 [m]. Probable deviation distance is Vd = 56 [m] and the direction Vp = 12 [m]. These values for the partial CEP are less than the total CEP when considered various deviations the missile. The deviation of the missile in the direction of dispersion is caused by the rotation of the missile around the longitudinal axis. The diagram shows the mean hit and the ellipse of distribution hits at the target. The same diagram shows the deviation distance for each missile Δx given in a percentage of the range. The missile number 4, 9 and 10 have the least the distribution, which corresponds to the time of the launch of the second missile $t_L = 1.0; 1.3; 1.33\ s$.

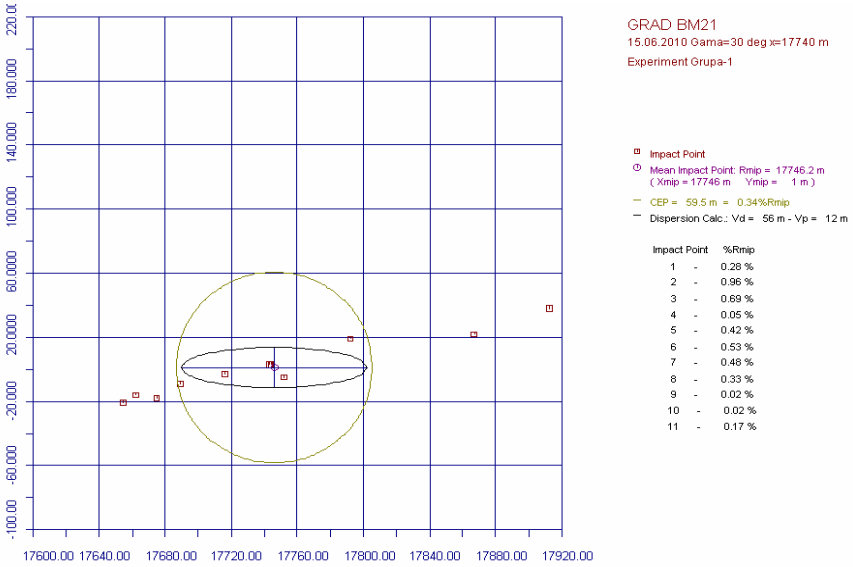

Fig.6 CEP at burst fire

6. The conclusion and the selection of optimal launch cadences

From the numerical results and diagrams of oscillation Fig.3 to Fig.5 we can derive the following conclusions:

1. Time of complete damping i.e. cessation of oscillation of full and empty launcher is approximately 3.5 s.
2. Maximum amplitude, displacement the muzzle tube in a vertical plane perpendicular to the axis of tube for the launcher loaded with 40 (39) missiles is 15[mm] and for launcher loaded with one missile (blank) is 17[mm].

The criteria for choice of optimal firing time of the second missile and all the other missiles at the following burst fire are subject to two requirements:

- displacement of the muzzle tube at the second firing missile must be less or equal to displacement of the muzzle tube at the first firing of missile and
- the minimum difference in range of the second missile compared to the first missile.

Optimal cadence should be sought to meet these two often conflicting demands.

If, as a basic criterion for choice of launching time of the second i.e. of all other missiles in a burst we take distribution size at the target, then from the diagram Fig.7, can be separated intervals $t_1 = 1.1s$, $t_2 = 1.279s$ and $t_3 = 1.33s$.

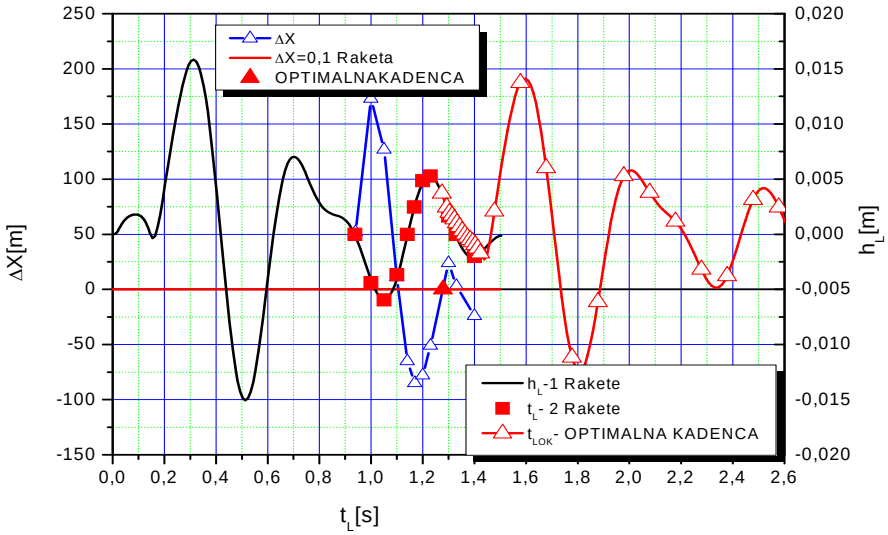

Fig.7 Optimal cadence launching 2.missile

Due to the requirement that the size of the launcher disorder that causes the second i.e. any subsequent missile in burst to be the smallest, the best time for launching the next missile is $t_2 = 1.279s$.

Analyzing the nature of the oscillation muzzle tube, Fig.7, it can be concluded that it is the period of time when the tube has a tendency to move towards "down" after reaching the maximum amplitude.

References

[1] Milošević, M., Đurković, V., Živanić, D., Analysis of influential parameters interaction Launcher-missiles and their contribution to the hit dispersion on the target, 2nd International Congress of Serbian Society of Mechanics (IConSSM 2009), Palić (Subotica), Serbia, 1-5 June 2009.
[2] Đurković, V. Contributes to finding the optimal parameters of launching missiles, Ph.D. thesis, VA VJ, Belgrade, 2001.
[3] Živanić D., Effect of self-oscillation multi tubes missile launchers to missile and scatter cadency Launches, Master thesis. Faculty of Mechanical Engineering, Belgrade, 1990.
[4] Ćurčin, M., Computer program for calculation unguided missile trajectory PUTNPV3, VTI, Belgrade 2008.
[5] Milošević, M., Computer program for the analysis of oscillation multi tubes missile launchers, LANS-M, VTI, Belgrade 2010.
[6] MIL-HDBK-762 (MI), Design of aerodynamically stabilized free Missiles, 17 July 1990.
[7] Živanić D., Đurković V., Milošević M: "Stability of selfpropeled multitube missile launcher during and just after a missile's starting", 2nd International Congress of Serbian Society of Mechanics (IConSSM 2009),Palić (Subotica), Serbia, 1-5 June 2009.
[8] Firing tables of the 122 mm M-21OF High-explosive Missile artillery combat vehicle, 1969.

ANALYSIS OF TRAFFIC INDUCED BUILDING VIBRATIONS USING SPECTRAL ELEMENT METHOD

Marija Nefovska-Danilović[1], Mira Petronijević[2], Marko Radišić[3]

[1] Faculty of Civil Engineering,
University of Belgrade, Bulevar kralja Aleksandra 73, 11000 Beograd
e-mail: marija@grf.bg.ac.rs
[2] Faculty of Civil Engineering,
University of Belgrade, Bulevar kralja Aleksandra 73, 11000 Beograd
e-mail: pmira@grf.bg.ac.rs
[3] Faculty of Civil Engineering,
University of Belgrade, Bulevar kralja Aleksandra 73, 11000 Beograd
e-mail: marko.radisic@gmail.com

Abstract. In this paper, the effects of traffic induced ground vibrations on the three frame buildings of different height are analyzed. The structures are subjected to horizontal and vertical ground vibrations which were measured in Belgrade, along the route of future metro line. Dynamic analysis including soil-structure interaction is carried out in frequency domain, using substructure approach. The dynamic response of frames is obtained using the Spectral Element Method (SEM) for frame elements **Error! Reference source not found.**and relevant impedance functions for foundation. Displacement fields of spectral element are exact solutions of the beam's partial differential equations of motion for axial deformation and bending. It results in the exact form of the interpolation functions, which can be presented as trigonometric or hyperbolic functions. Impedance functions of the soil are calculated using Integral Transform Method (ITM). Based on theoretical considerations, the numerical analysis has been performed in order to determine dynamic responses and maximum vibration levels of investigated frames. Numerical results are compared with allowable vibration levels according to British Standard: 6472.

1. Introduction

Rapid urbanization has led to building construction near the roads, highways and railways. Moreover, new technology of production of stronger materials have resulted in higher, lighter and more flexible buildings, which made them more sensitive to traffic-induced vibration. Numerous investigations have shown that traffic-induced vibrations rarely cause damage of the surrounding structures and buildings, but they produce annoyance of building residents, as well as normal functioning of sensitive equipment, [1-4].

The main source of traffic vibrations in the cities are passage of buses, trucks, and trams, as well as subway. Vibrations are mostly generated due to road/track irregularities and vehicle imperfections. They induce waves in the soil that propagate in all directions and affect the surrounding buildings causing their vibrations. Dynamic response of building depends on the dynamic properties of the building – foundation - subsoil system. Therefore, both the structure and the soil region have to be properly modeled.

Contemporary soil-structure-interaction (SSI) analyses are based on substructure approach: FEM is usually used for structural modeling, while soil region can be modeled using FEM, Boundary Element Method (BEM), [5], Thin Layer Method (TLM), [6] or Integral Transform Method (ITM), [7], [8].

As an alternative to the Finite Element Method for structural modeling in dynamic analysis, so called Spectral Element Method (SEM) can be used, which significantly decrease the

number of elements compared with FEM. Displacement field of spectral element is obtained solving the partial differential equation of motion. It results in the exact form of the interpolation functions, which contain trigonometric or hyperbolic functions. Therefore, only one element can exactly represent dynamic behavior of a beam. Interpolation functions and dynamic stiffness matrix of spectral element are frequency dependent.
In this paper, the effects of traffic-induced ground vibrations on dynamic response of concrete frame buildings of different heights are analyzed, including soil-structure interaction. Numerical analysis is carried out in frequency domain using substructure approach. For this analysis a special computer code in Matlab has been developed. Frame structure is modeled using Spectral element Method. It is assumed that frame structure is founded on rigid rectangular foundations on homogeneous elastic half-space. Dynamic stiffness matrix of the rigid foundation has been calculated using ITM, [8]. The structures are subjected to horizontal and vertical ground vibrations measured in Belgrade in 2006, along the route of future metro line, [9]. These ground vibrations were generated by tram and heavy truck crossing a rubber obstacle on the road. Influence of soil stiffness on dynamic response of frame structures subjected to traffic-induced ground vibrations has been obtained and discussed. Numerical results are compared with allowable vibration levels according to British standard BS: 6472, [12]. The allowable vibration levels are defined in terms of the peak particle velocity (PPV).

2. Structural modeling using Spectral Element Method

Conventional finite element analysis has been widely used for solving different kind of structural static and dynamic problems. Displacement fields of each finite element are given as polynomial functions. The structure is meshed in order to represent the geometry, boundary conditions, mass and applied loads. Generally, in dynamic analysis more finite elements are required than in the static analysis. The number of finite elements is also influenced by the highest frequency in the analysis. As an alternative to the Finite Element Method in dynamic analysis, so-called Spectral Element Method (SEM) can be used. Doyle proposed this method to analyze wave propagation in frame structures, [10]. Displacement field of spectral element is obtained solving the partial differential equation of motion. It results in the exact form of the interpolation functions, which contain trigonometric or hyperbolic functions. Therefore, only one element can exactly represent dynamic behavior of a beam. Interpolation functions and dynamic stiffness matrix of spectral element are frequency dependent. Consequently, dynamic response analysis needs to be carried out in frequency domain, using discrete Fourier transform, [11]. The usage of spectral elements reduces the number of unknowns and increases the accuracy of the numerical results.

2.1 Interpolation functions

Bar element. Bar element assumes only longitudinal wave motion. Equation of motion for bar element can be obtained from the balance of forces including inertial force:

$$EA\frac{\partial^2 u}{\partial x^2} = \rho A\frac{\partial^2 u}{\partial t^2} \tag{1}$$

where E, A, ρ, $u = u(x, t)$ are, respectively, Young's modulus, cross-sectional area, mass density and displacement in x direction of bar. A bar element with nodal displacements and

corresponding forces is given in Figure 1. Introducing spectral representation of displacement *u(x, t)* as

$$u(x,t) = \sum \hat{u}(x,\omega) e^{i\omega t}, \tag{2}$$

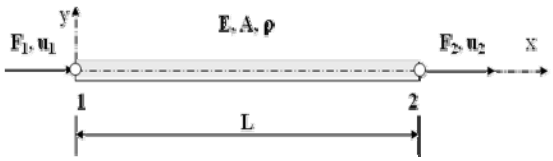

Figure 1. Bar spectral element

where ω is angular frequency, Fourier transform of Equation (1) can be expressed as

$$\frac{\partial^2 \hat{u}}{\partial x^2} + k^2 \hat{u} = 0, \tag{3}$$

where $k^2 = \omega^2 \frac{\rho A}{EA}$ is wave number. General solution of differential equation (3) can be given as

$$\hat{u}(x,\omega) = C_1 e^{-ikx} + C_2 e^{ikx}. \tag{4}$$

Integration constants C_1 and C_2 are obtained from boundary conditions, setting:

$$\hat{u}(0) = \hat{u}_1, \quad \hat{u}(L) = \hat{u}_2. \tag{5}$$

From Equations (4) and (5) the displacement in longitudinal direction at an arbitrary point in the bar axis can be written as:

$$\hat{u}(x,\omega) = \hat{N}_1(x)\hat{u}_1 + \hat{N}_2(x)\hat{u}_2, \tag{6}$$

or in matrix form:

$$\hat{u}(x,\omega) = \mathbf{N}\mathbf{q}, \tag{13}$$

where $\hat{N}_1(x)$ and $\hat{N}_2(x)$ are frequency dependant interpolation functions, **N** is matrix of interpolation functions and **q** vector of nodal displacements of beam spectral element.

Beam element. Dynamic stiffness matrix of beam element for flexural motion, given in Figure 2, can be derived in similar way as for bar element. Differential equation of motion for Euler-Bernoulli beam is

$$EI \frac{\partial^4 w}{\partial x^4} = -\rho A \frac{\partial^2 w}{\partial t^2} \tag{7}$$

where *I, w = w(x, t)* are, respectively, second moment inertia of cross-section and transverse displacement of beam.

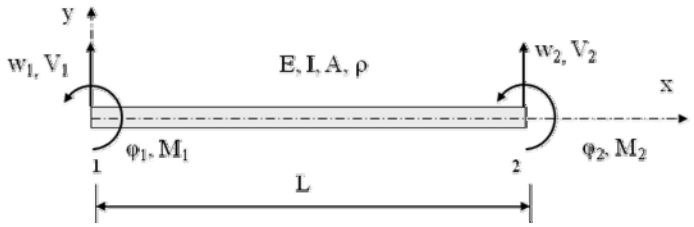

Figure 2. Beam spectral element

Introducing spectral representation of displacement *w(x, t)* as

$$w(x,t) = \sum \hat{w}(x,\omega) e^{i\omega t}, \tag{8}$$

where ω is angular frequency, Fourier transform of Equation (7) can be expressed as

$$\frac{\partial^4 \hat{w}}{\partial x^4} - k^4 \hat{w} = 0, \tag{9}$$

where $k^4 = \omega^2 \frac{\rho A}{EI}$ is wave number. General solution of differential equation (9) is

$$\hat{w}(x,\omega) = C_1 e^{-ikx} + C_2 e^{ikx} + C_3 e^{-kx} + C_4 e^{kx}. \tag{10}$$

Integration constants C_1, C_2, C_3 and C_4 are obtained from boundary conditions, setting:

$$\hat{w}(0) = \hat{w}_1, \quad \hat{\varphi}(0) = \hat{\varphi}_1, \quad \hat{w}(L) = \hat{w}_2, \quad \hat{\varphi}(L) = \hat{\varphi}_2. \tag{11}$$

From Equations (10) and (11) the displacement in transverse direction at an arbitrary point in the beam axis can be written as:

$$\hat{w}(x,\omega) = \hat{N}_1(x)\hat{w}_1 + \hat{N}_2(x)\hat{\varphi}_1 + \hat{N}_3(x)\hat{w}_2 + \hat{N}_4(x)\hat{\varphi}_2, \tag{12}$$

or in matrix form:

$$\hat{w}(x,\omega) = \mathbf{Nq}, \tag{13}$$

where $\hat{N}_1(x)$, $\hat{N}_2(x)$, $\hat{N}_3(x)$ and $\hat{N}_4(x)$ are frequency dependent interpolation functions, **N** is matrix of interpolation functions and **q** vector of nodal displacements of beam spectral element.

2.2 Dynamic stiffness matrix

Dynamic stiffness matrix of spectral element with defined degrees of freedom can be developed using principle of virtual work, [16]:

$$\delta W = \delta W_{ext} + \delta W_{\text{int}} = 0, \tag{14}$$

where δW_{ext} is the virtual work done by external forces and δW_{int} is virtual work done by internal forces of a solid body. In case of elastic deformable body, the term δW_{int} is the work due to the elastic body deformation, i.e.

$$\delta W_{\text{int}} = -\delta U = -\int_V \boldsymbol{\sigma}^T \boldsymbol{\varepsilon} dV \,, \tag{15}$$

where U is potential energy. In order to take into account the time dependence of all variables, D'Alembert's principle will be used. Then, the virtual work of external forces can be written as:

$$\delta W_{ext} = \int_S f^S \delta u dS + \int_V f^b \delta u dV - \int_V \rho \ddot{u} \delta u dV \,, \tag{16}$$

where the first term is work done by external surface forces, the second term is work done by body forces and the third term accounts for inertial forces of a solid body. Using kinematic and constitutive relations:

$$\begin{aligned} \varepsilon &= \mathbf{L}u = \mathbf{LNq} = \mathbf{Bq} \\ \boldsymbol{\sigma} &= \mathbf{E}\varepsilon = \mathbf{EBq} \end{aligned} \,, \tag{17}$$

where **L** is an operator matrix and **E** is matrix of elastic constants, from Equations (14)-(16) follows:

$$\begin{gathered} \left(\int_V \mathbf{B}^T \mathbf{E} \mathbf{B} dV - \omega^2 \int_V \rho \mathbf{N}^T \mathbf{N} dV \right) \mathbf{q} = \int_V \mathbf{N}^T f^b dV + \int_S \mathbf{N}^T f^s dS \\ \mathbf{K}_{D_e} \mathbf{q} = \mathbf{P} \end{gathered} \,, \tag{18}$$

where $\mathbf{K}_{D_e}$ is dynamic stiffness matrix of spectral element. For bar element dynamic stiffness matrix derived from Equation (18) is:

$$\mathbf{K}_{D_e} = \left(\int_l \mathbf{N}'^T EA \mathbf{N}' dx - \omega^2 \int_l \rho A \mathbf{N}^T \mathbf{N} dx \right), \tag{19}$$

while for beam element dynamic stiffness matrix is:

$$\mathbf{K}_{D_e} = \left(\int_l \mathbf{N}''^T EI \mathbf{N}'' dx - \omega^2 \int_l \rho A \mathbf{N}^T \mathbf{N} dx \right), \tag{20}$$

3. Equation of motion for soil-structure system

Soil-structure model consists of two sub-structures, described in Figure 3. It is assumed that the system is subjected to horizontal and vertical traffic-induced ground motion. Nodes at the soil-structure interface are defined as interaction nodes (index *i*), while remaining nodes of the structure are defined as structural nodes (index *s*).
Equation of motion of soil-structure system in frequency domain can be written as:

$$\begin{bmatrix} \mathbf{K}_{ss}^S & \mathbf{K}_{si}^S \\ \mathbf{K}_{is}^S & \mathbf{K}_{ii}^S + \mathbf{K}_{ii}^F \end{bmatrix} \begin{bmatrix} \hat{\mathbf{u}}_s \\ \hat{\mathbf{u}}_i \end{bmatrix} = \begin{bmatrix} 0 \\ \mathbf{K}_{ii}^F \hat{\mathbf{u}}_i' \end{bmatrix}, \tag{21}$$

where $\mathbf{K}_{ii}^F$ is dynamic stiffness matrix of the soil-structure interface, $\mathbf{K}_{ss}^S$, $\mathbf{K}_{si}^S$, $\mathbf{K}_{is}^S$ are dynamic stiffness sub-matrices of the structure obtained using SEM, $\hat{\mathbf{u}}_s$ and $\hat{\mathbf{u}}_i$ are displacements at structural and interaction nodes, respectively, while $\hat{\mathbf{u}}_i'$ is vector of traffic-induced ground motion.

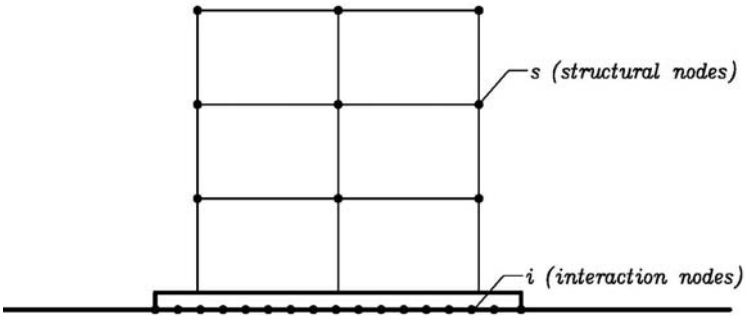

Figure 3. Soil-structure system

Dynamic stiffness matrix (impedance matrix) of the soil is defined as dynamic stiffness matrix of the interaction nodes at the soil-structure interface. It is calculated by the following procedure:
The region of the foundation is discretized by a set of interaction points *i*. At each point a unit point load in horizontal and vertical direction is applied and corresponding displacements of the soil are calculated using ITM, [8]. Calculated displacements form dynamic flexibility (compliance) matrix **F**. Size of the flexibility matrix is *2N*x*2N*, where *N* is number of interaction nodes. Dynamic stiffness matrix of the soil $\mathbf{K}_{ii}^{F}$ is obtained inverting the flexibility matrix:

$$\mathbf{K}_{ii}^{F} = \mathbf{F}^{-1}. \tag{22}$$

4. Dynamic stiffness matrix for rigid foundations

We consider a rectangular massless rigid foundation resting on the soil surface, excited by harmonic force, Figure 4. Motion of the rigid basement can be described by the displacement vector $\hat{\mathbf{u}}_o$ at the center of the base interface (point O). For 2D problems, displacement vector $\hat{\mathbf{u}}_o$ consists of two translations (horizontal-u and vertical-v) and one rotation-φ. The corresponding force vector acting at the point O is $\mathbf{P}_o$. Since dynamic properties of the foundation depend on the frequency of excitation, force-displacement relation is given in frequency domain through dynamic stiffness matrix of the foundation:

$$\hat{\mathbf{P}}_\mathbf{O} = \mathbf{K}_\mathbf{O}\hat{\mathbf{u}}_\mathbf{O}, \tag{23}$$

where:

$$\hat{\mathbf{P}}_\mathbf{O} = \begin{bmatrix} \hat{P}_x \\ \hat{P}_y \\ \hat{M}_z \end{bmatrix}, \quad \hat{\mathbf{u}}_\mathbf{O} = \begin{bmatrix} \hat{u} \\ \hat{v} \\ \hat{\varphi} \end{bmatrix}, \quad \mathbf{K}_\mathbf{O} = \begin{bmatrix} k_h & 0 & k_{hr} \\ 0 & k_v & 0 \\ k_{rh} & 0 & k_r \end{bmatrix}. \tag{24}$$

For surface foundations, coupling terms k_{hr} can be neglected.
If $\hat{\mathbf{u}}_i$ is displacement vector of interaction nodes, the relation between $\hat{\mathbf{u}}_i$ and $\hat{\mathbf{u}}_o$ is given through kinematic matrix **a**:

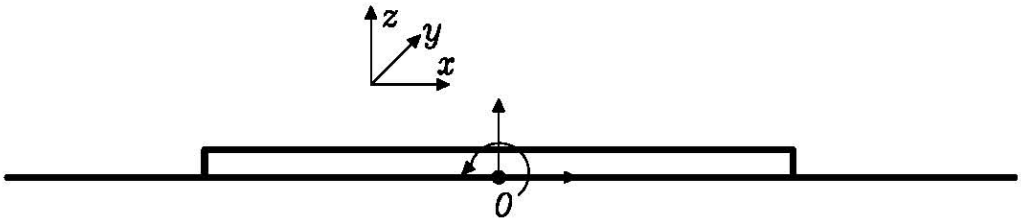

Figure 4. Surface rigid foundation, degrees of freedom

$$\hat{\mathbf{u}}_{\mathrm{i}} = \mathbf{a}\hat{\mathbf{u}}_{\mathrm{o}}\,,\ \mathbf{a} = \begin{bmatrix} \mathbf{a}_1 \\ \cdots \\ \mathbf{a}_i \\ \cdots \\ \mathbf{a}_N \end{bmatrix}_{2Nx3}, \quad \mathbf{a}_i = \begin{bmatrix} 1 & 0 & -y_i \\ 0 & 1 & x_i \end{bmatrix}. \tag{25}$$

where (x_i , y_i) are coordinates of the interaction nodes. Equating the deformation energy for flexible and rigid foundation, dynamic stiffness matrix of rigid foundation is given as:

$$\mathbf{K}_{\mathrm{o}} = \mathbf{a}^T \mathbf{K}_{ii}^F \mathbf{a}\,. \tag{26}$$

5. Traffic-induced ground vibrations

Measurement of traffic-induced vibrations was carried out on 52 buildings along the future metro line in Belgrade in 2006. The buildings were representative of several combinations of building types, importance (historical, institutional, office, and residential buildings) and site conditions. The scope of investigation was to evaluate the vibration level caused by existing road and tram traffic, with reference to the potential building damage and the human annoyance, using existing standards. The investigation work was done for the Belgrade Land Development Public Agency, by the Geological Institute of Serbia, Geophysical Institute -NIS and the Faculty of Civil Engineering University of Belgrade, [9]. Measurements were carried out by the Geophysical Institute - NIS using I/O System One that consists of 5 three-component geophones. The velocities were measured simultaneously in three orthogonal directions: vertical direction - V, horizontal direction parallel to the road - H1 and horizontal direction perpendicular to the road - H2, at five different points: 1 - on the sidewalk about 1 m from the road/track, 2 – on the ground at the external foundation wall, 3 – in the basement of building close to the external wall, at the top floor at the corner – 4 and midpoint of the floor – 5.

Vibrations were generated by the following sources:

- ambient sources,
- truck weighted approximately 14 tons at speed 50 km/h,
- truck :14 tons, speed 50 km/h, crossing 3 cm thick rubber obstacle,
- articulated bus or tram.

During the measurements, a large amount of data had been collected and processed. It was found out that the highest vibration levels were generated by tram and heavy truck

crossing 3cm thick rubber obstacle. Therefore, the ground vibrations induced by these two vibration sources, at the site with high vibration level, will be used as input ground motion for dynamic response analysis of frame structures.

Time histories and power spectra for horizontal and vertical ground vibrations measured in King's Alexander Boulevard in Belgrade are presented in Figures 5-8. Measurement point was approximately at 11 m from the road/track on the ground surface. In the case of tram traffic, predominant frequency range is between 15 and 27 Hz for horizontal vibrations and between 13 and 27 Hz for vertical vibrations, whereas for road traffic induced by heavy truck crossing a rubber obstacle predominant frequency range is between 2 and 6 Hz for both horizontal and vertical vibrations. Higher vibration levels are obtained for vertical vibrations. The ground displacements obtained from integrating ground velocities, are presented in Figures 9-12.

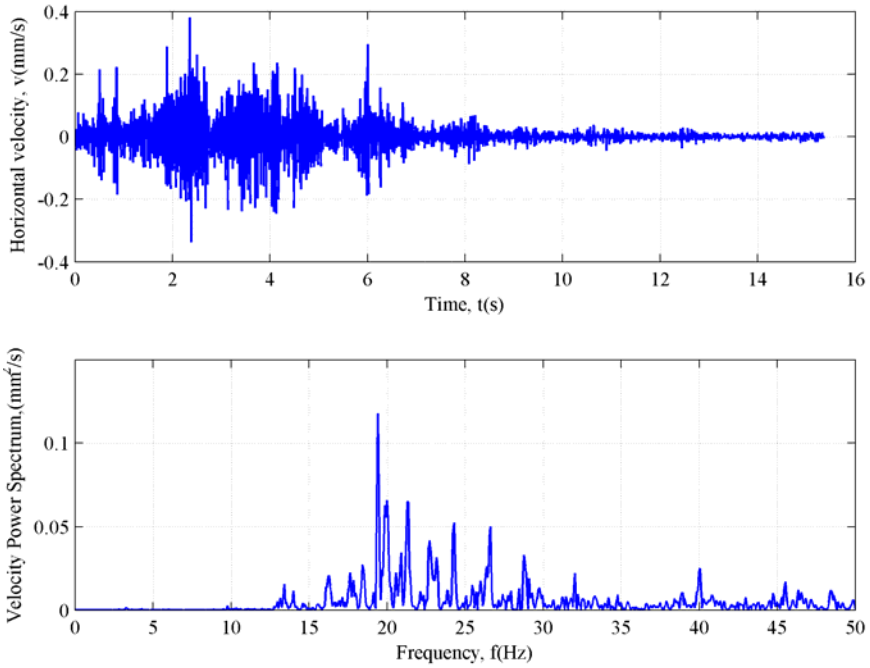

Fig. 5 Time history and Power spectrum of horizontal ground velocity (tram, v=20 km/h, distance to track 11 m)

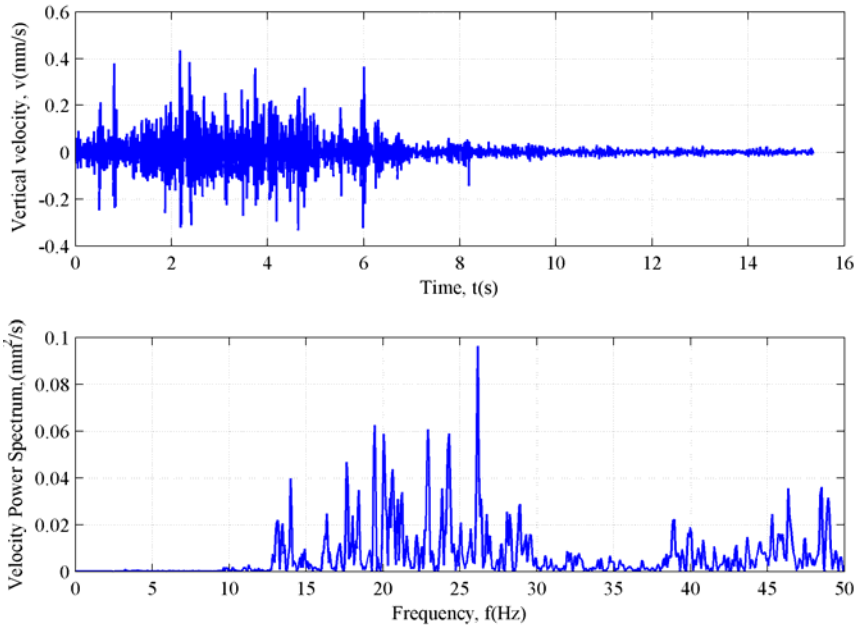

Fig. 6 Time history and Power spectrum of vertical ground velocity (tram, v=20 km/h, distance to track 11 m)

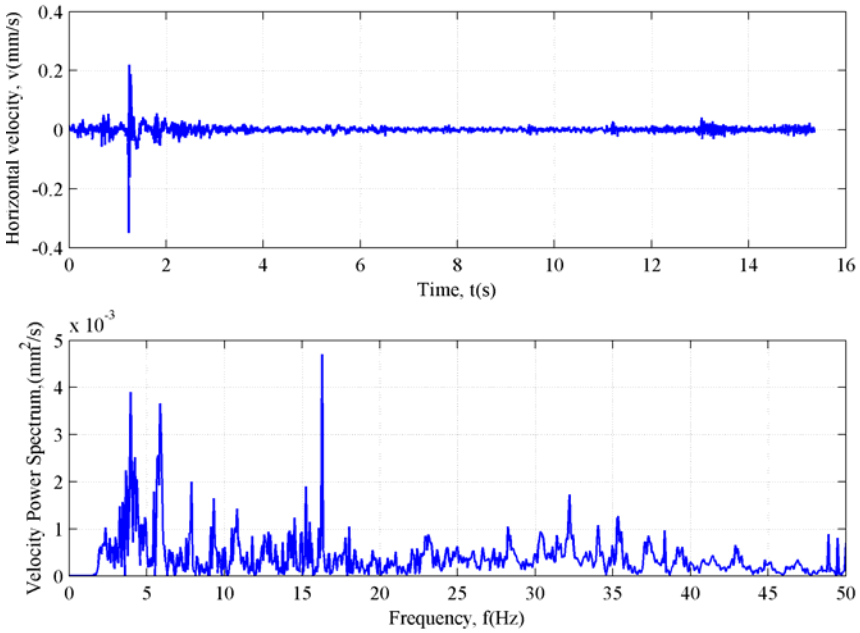

Fig. 7 Time history and Power spectrum of horizontal ground velocity (truck crossing rubber obstacle, v=50 km/h, distance to road 11 m)

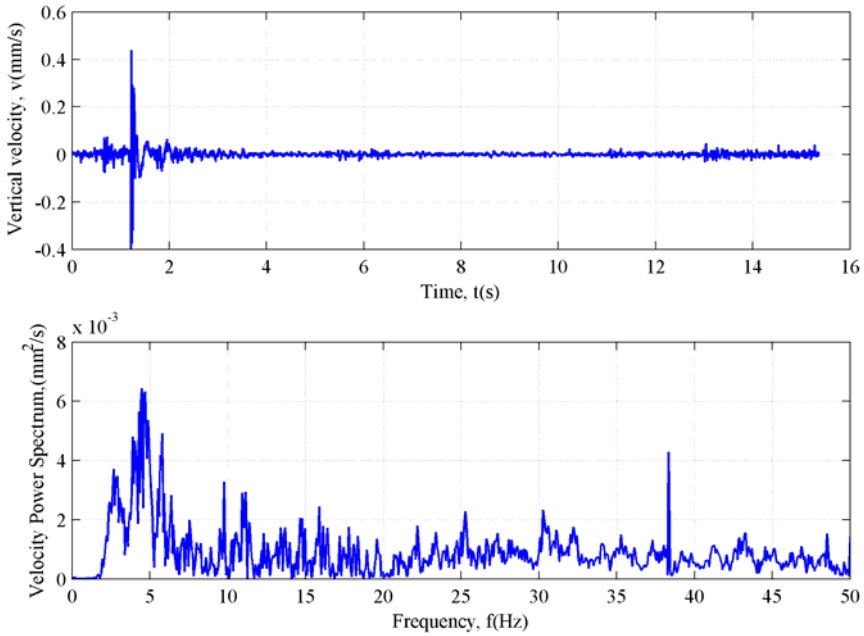

Fig. 8 Time history and Power spectrum of vertical ground velocity (truck crossing rubber obstacle, v=50 km/h, distance to road 11m)

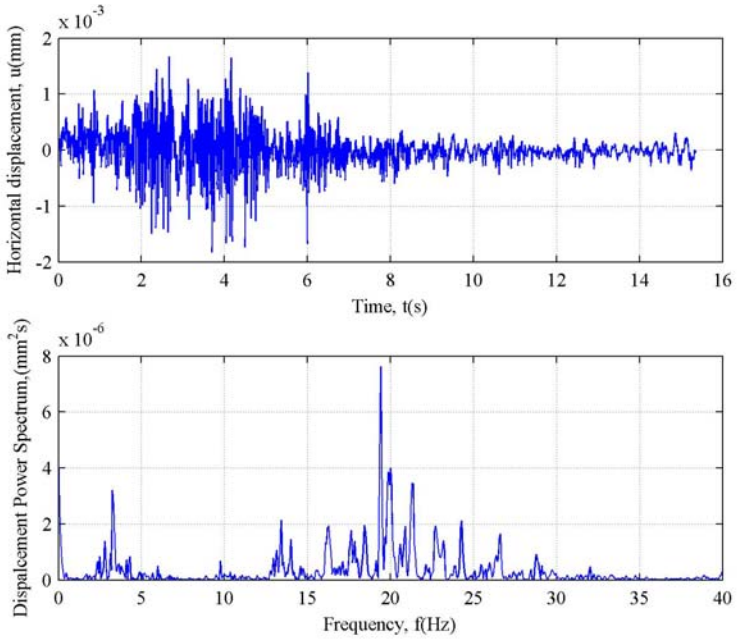

Fig. 9 Time history and Power spectrum of horizontal ground displacement (tram, v=20 km/h, distance to track 11 m)

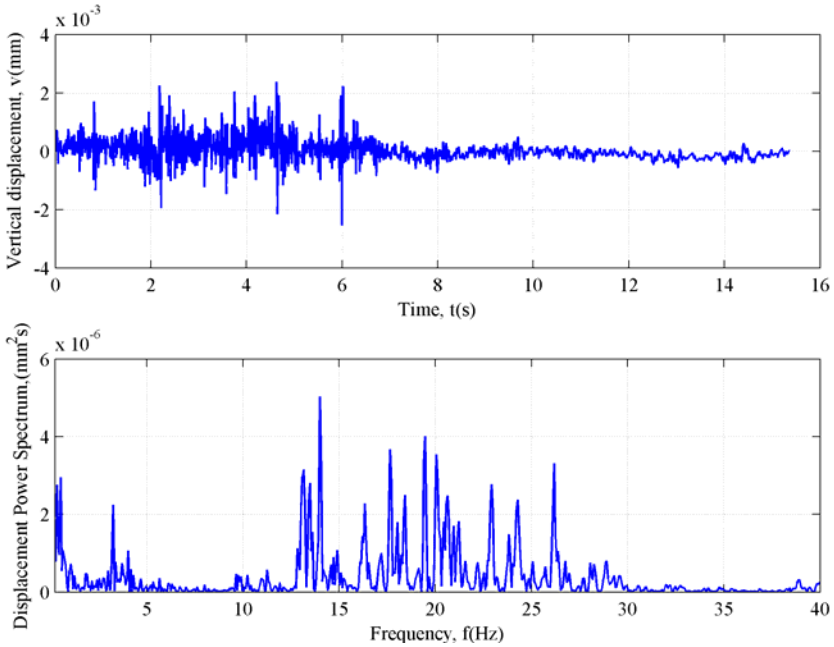

Fig. 10 Time history and Power spectrum of vertical ground displacement (tram, v=20 km/h, distance to track 11 m)

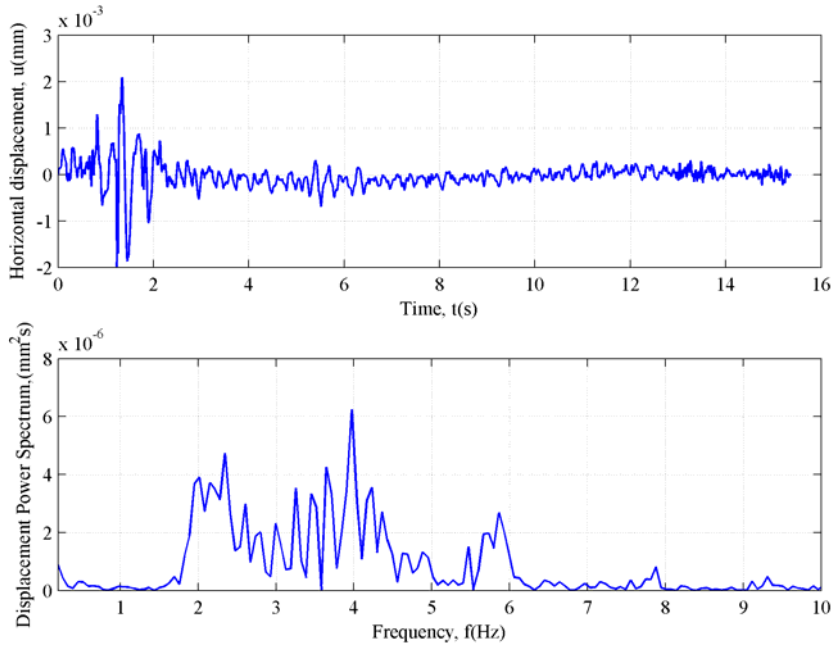

Fig. 11 Time history and Power spectrum of horizontal ground displacement (truck crossing rubber obstacle, v=50 km/h, distance to road 11 m)

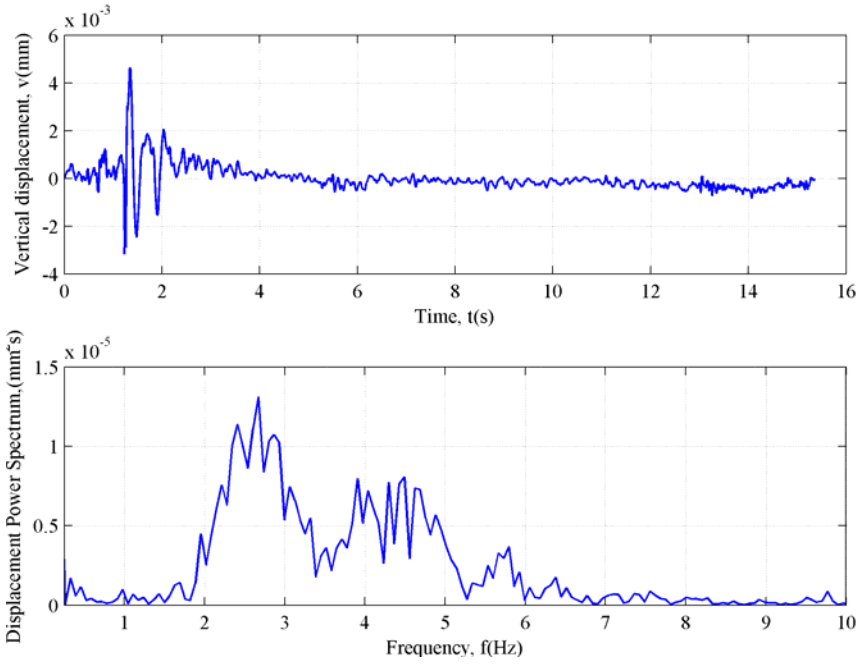

Fig. 12 Time history and Power spectrum of vertical ground displacement (truck crossing rubber obstacle, v=50 km/h, distance to road 11 m)

6. Numerical results

Three concrete two bay frames of different heights (two-storey, six-storey and twelve-storey) are subjected to traffic-induced horizontal and vertical ground motion. Bay width is 4 m. Story height is 3 m, except for the first floor – 3.5 m. Mass of each floor is 9 t, which is continuously distributed as additional mass along each beam. Geometrical properties of frame members are given in Table 1. Structural damping coefficient is 5%.
The frames are founded on rigid and massless rectangular footings with a length 2 m and a width 2 m. The footings rest on elastic homogeneous half space. Material properties of the half space are:

- mass density: 2000 kg/m^3,
- shear waves velocity : 100 m/s,
- Poisson's ratio: 0.33.

In order to calculate dynamic response of investigated frames, a computer program using Matlab was developed for dynamic analysis of 2D frame structures in frequency domain, including soil-structure interaction. The structure is modeled using SEM, while ITM is used for calculation of dynamic stiffness matrix of the subsoil, [8]. Natural frequencies for horizontal and vertical mode shapes are given in Tables 2 and 3, respectively.

In order to emphasize the effect of soil-structure interaction on dynamic response, analysis has also been carried out for the corresponding fixed-base frames. Displacement and velocity envelopes of the investigated frames subjected to traffic-induced ground vibrations are presented in Figures 13-18, whereas displacement response spectra are given in Figures 19-22. Natural frequencies of investigated frames decrease when soils stiffness is

accoutered for, which is especially pronounced for vertical vibration modes, as vertical frame stiffness-vertical soil stiffness ratio is much larger than corresponding horizontal stiffness ratio. Consequently, vertical dynamic responses of fixed base frames are quite different than the dynamic responses when SSI is taken into account, especially for tram – induced traffic vibrations.

Table 1 Geometrical properties of investigated frames

Frame	*Columns*		*Beams*
	external	*Internal*	
Two storey	20x30 cm	25x30 cm	23x40 cm
Six storey	20x30 cm	25x50 cm (1-2 floor) 25x40 cm (3-5 floor) 25x30 cm (6th floor)	
Twelve storey	25x40 cm (1-5 floor) 20x35 cm (6-8 floor) 20x30 cm (9-12 floor)	25x80 cm (1-2 floor) 25x70 cm (3-4 floor) 25x60 cm (5-7 floor) 25x50 cm (8-10 floor) 25x40 cm (11-12 floor)	

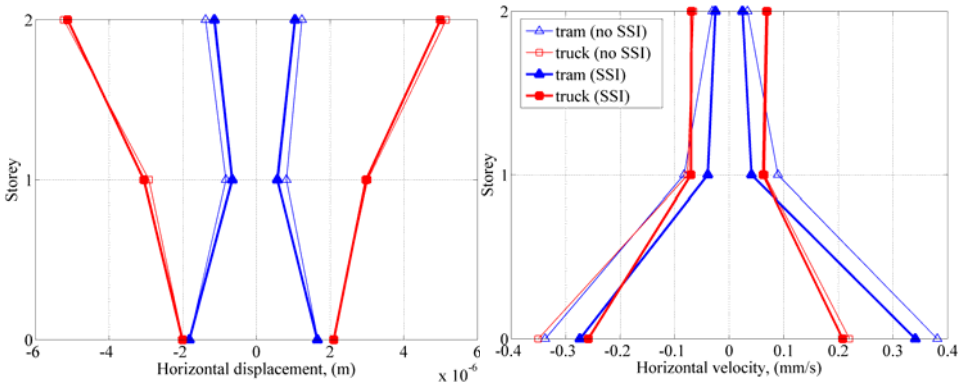

Fig. 13 Horizontal displacement and velocity envelopes of two-storey frame

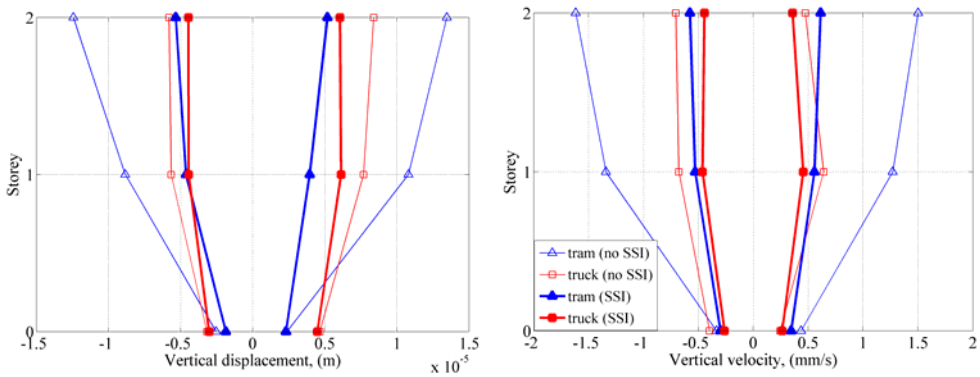

Figure 14. Vertical displacement and velocity envelopes of two-storey frame (middle point on the beam)

Table 2 Natural frequencies for horizontal mode shapes

Frame storey	*Natural frequencies (fixed-base frame), Hz*					*Natural frequencies with SSI, Hz*				
	Mode 1	Mode 2	Mode 3	Mode 4	Mode 5	Mode 1	Mode 2	Mode 3	Mode 4	Mode 5
2	2.37	7.49				2.29	7.40			
6	1.08	3.22	5.48	7.95	10.71	1.01	3.11	5.36	7.81	10.55
12	0.62	1.81	3.21	4.7	6.34	0.56	1.74	3.11	4.55	6.14

Table 3 Natural frequencies for vertical mode shapes

Frame storey	*Natural frequencies (fixed-base frame), Hz*					*Natural frequencies with SSI, Hz*				
	Mode 1	Mode 2	Mode 3	Mode 4	Mode 5	Mode 1	Mode 2	Mode 3	Mode 4	Mode 5
2	15.79	18.06	19.31	22.21	39.53	15.44	21.68	50.8	57.5	63.0
6	12.22	13.41	16.68	18.34	19.25	10.55	12.8	16.24	18.09	18.94
12	8.11	13.83	16.74	18.13	18.83	7.9	11.58	13.57	15.93	16.61

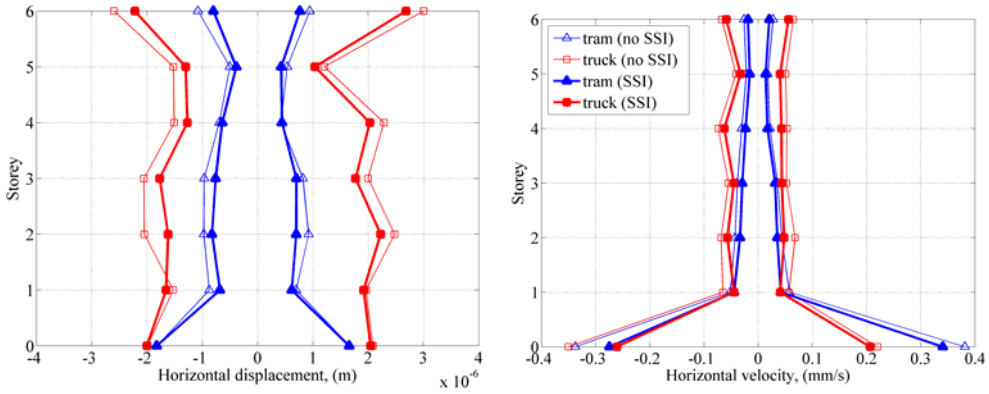

Figure 15. Horizontal displacement and velocity envelopes of six-storey frame

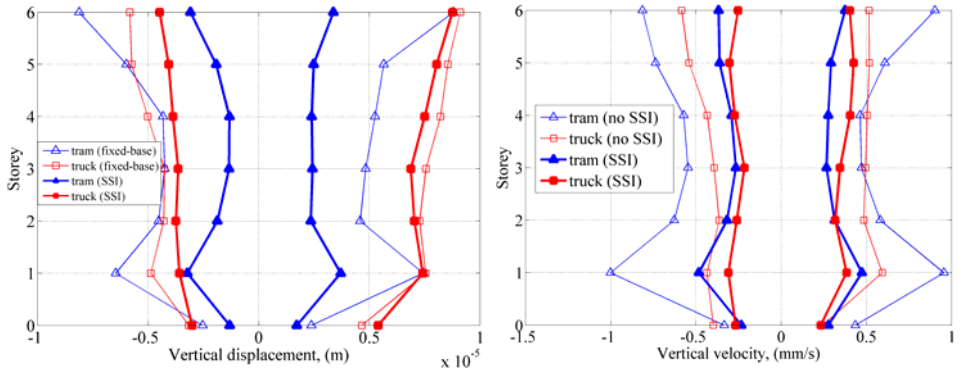

Figure 16. Vertical displacement and velocity envelopes of six-storey frame (middle point on the beam)

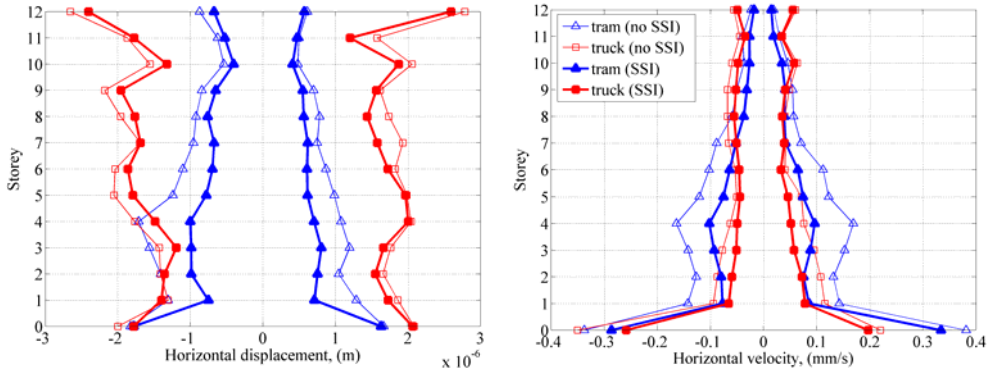

Figure 17. Horizontal displacement and velocity envelopes of twelve-storey frame

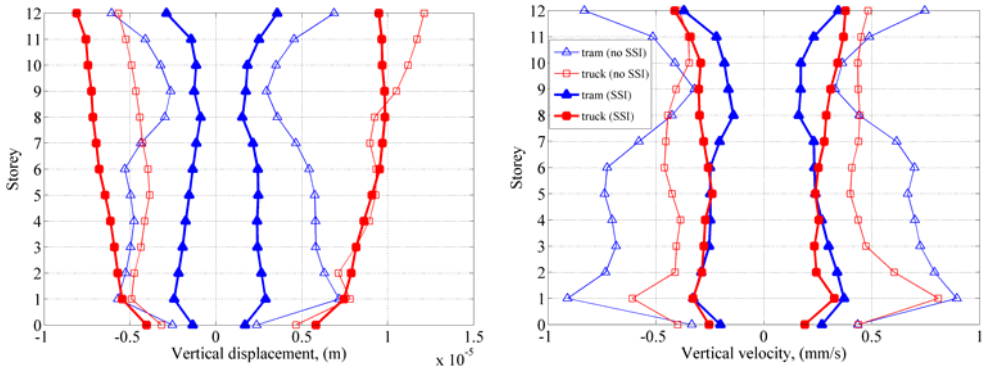

Figure 18. Vertical displacement and velocity envelopes of twelve-storey frame (middle point on the beam)

Horizontal vibrations: Truck crossing a rubber obstacle induces larger horizontal vibrations than tram traffic for all frames, since the dominant horizontal vibration modes fall into the dominant frequency range for truck traffic (2-5 Hz). Two-storey frame experiences the largest horizontal displacements and twelve-storey frame the lowest horizontal displacements due to truck induced ground motion. Main reason for that lays in fact that fundamental vibration mode of two-storey frame (2.37 Hz) falls in the dominant frequency range for truck induced horizontal ground vibrations. Consequently, horizontal displacement of the top floor of two-storey frame is highly amplified.

Vertical vibrations: The largest vertical displacements occur at the midpoint of the beam on the top floor of the investigated frames. Vertical dynamic responses of all frames are influenced by lower vertical vibration modes. Two-storey frame undergoes the largest vertical displacements and velocities for tram traffic as natural frequencies fall into the range of predominant frequencies for tram vertical vibrations (13-20 Hz). Predominant frequency range for truck traffic (2-6 Hz) is much lower than fundamental frequency of vertical vibration mode for all investigated frames. Consequently, truck traffic induces lower vertical vibration levels and lower amplification factors. Taking into account soil – structure interaction in the analysis can significantly alter dynamic response of frames. Vertical displacements and velocity envelopes have much lower values than corresponding values for fixed base frames due to radiation damping, which are more pronounced for tram traffic.

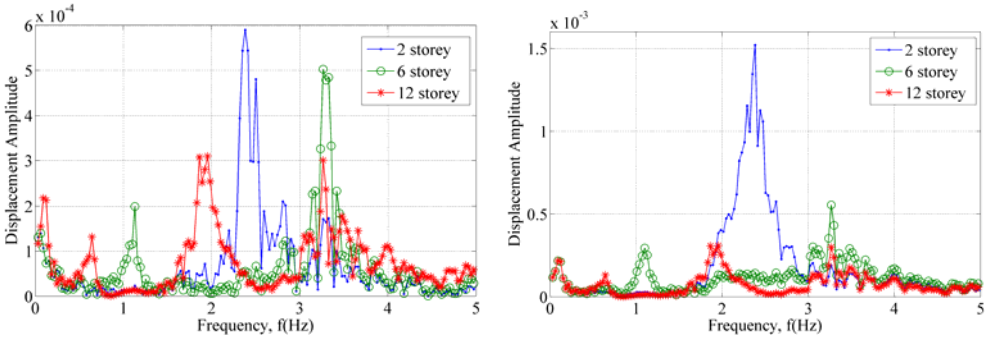

a) b)

Figure 19. Response spectra for horizontal displacement of top floor: a) tram traffic, b) truck traffic, without SSI

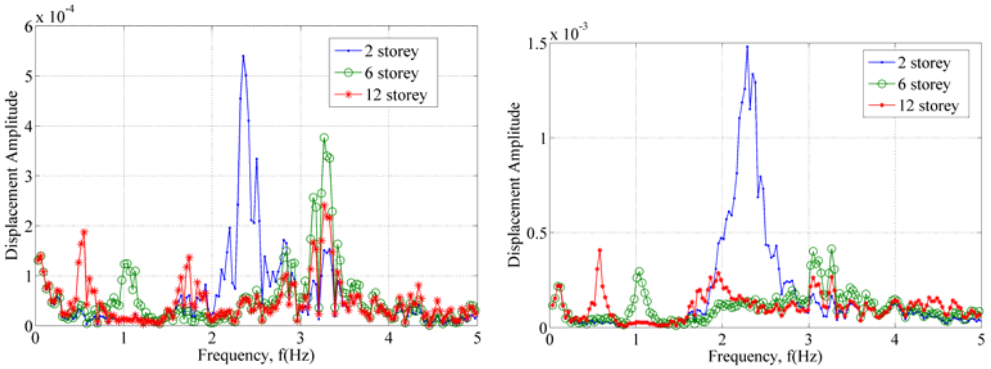

a) b)

Figure 20. Response spectra for horizontal displacement of top floor: a) tram traffic, b) truck traffic, including SSI

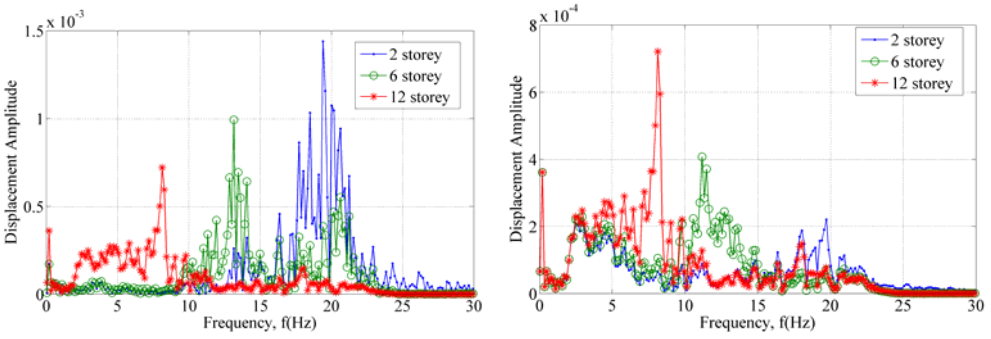

a) b)

Figure 21. Response spectra for vertical displacement of top floor (middle point of beam): a) tram traffic, b) truck traffic, without SSI

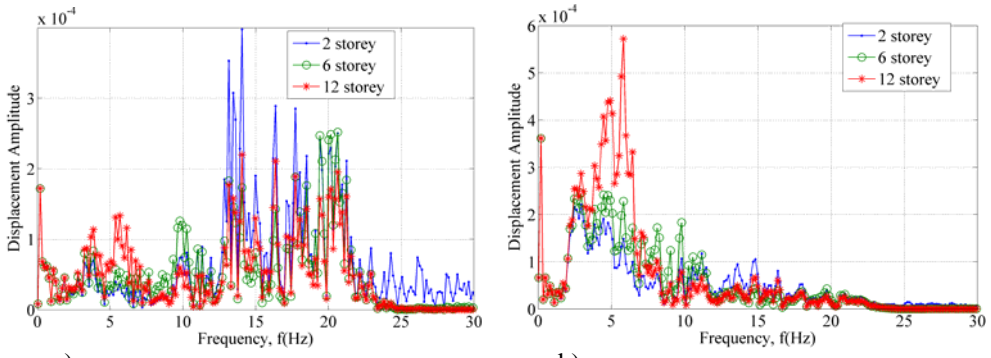

Figure 22. Response spectra for vertical displacement of top floor (middle point of beam): a) tram traffic, b) truck traffic, including SSI

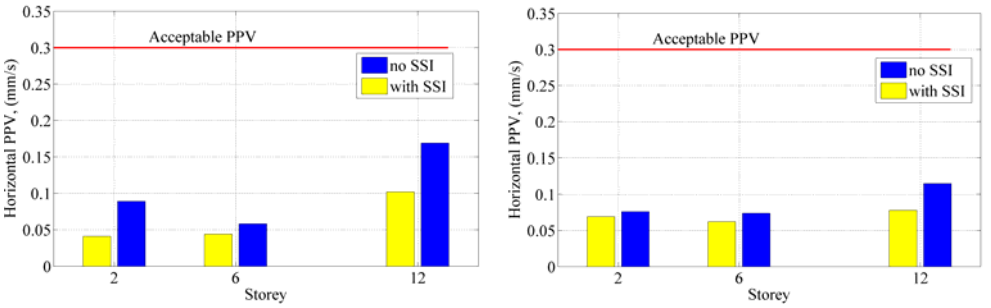

Figure 23. Peak particle velocities for horizontal traffic induced vibrations: a) tram traffic, b) truck traffic

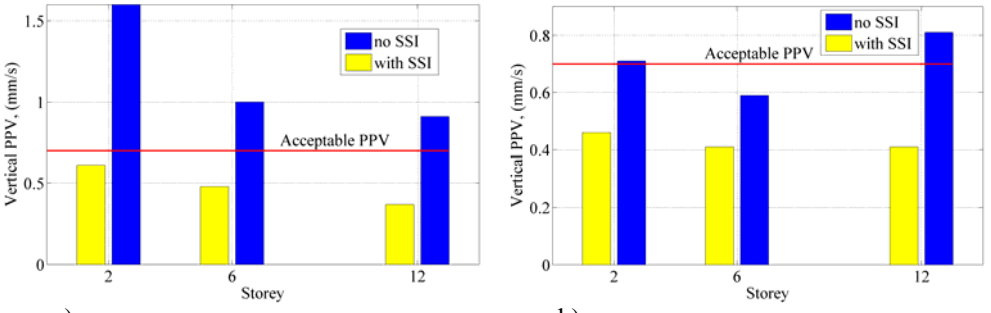

Figure 24. Peak particle velocities for vertical traffic induced vibrations: a) tram traffic, b) truck traffic

Maximum horizontal and vertical velocities of all frames are presented in Figures 23 and 24. Horizontal vibrations do not exceed the acceptable limits in terms of peak particle velocity (PPV), according to BS: 6472, [8]. Unlike horizontal vibrations, vertical vibrations for fixed base frames are 2-5 times larger than acceptable vertical vibration limits. Vertical peak particle velocities for investigated frames are significantly decreased when SSI is taken into account, and put below the acceptable level according to BS.

7. Conclusions

Traffic induced ground vibrations were measured along the future metro line in Belgrade. Vibrations induced by the existing tram traffic and heavy truck crossing 3 cm thick rubber obstacle were analyzed. These vibrations were used as input ground motion in order to obtain dynamic response of three frame structures of different heights, including soil-structure interaction. Numerical analysis was carried out in the frequency domain using Spectral Element Method. Based on the theoretical considerations a computer program using Matlab was developed for dynamic response analysis of 2D frame structures in the frequency domain.

Soil-structure interaction can significantly alter the dynamic response of frame structures. Higher structural stiffness-soil stiffness ratio more pronounces the effect of SSI.
For all frames, tram induces larger vertical vibrations than truck, while truck induces larger horizontal vibrations. Vertical dynamic responses for all frames including SSI are lower than the corresponding responses in case of fixed base frames. Calculated horizontal vibrations are less than the allowable vibration limits according to BS. Although the measured vertical traffic induced vibrations are not strong enough to cause any damage to the investigated fixed base frame structures, they are annoying to building occupants, since they are higher than the threshold values.

Acknowledgement. This research is carried out within the Project TR 36046 supported by the Ministry of Science and Technology, Republic of Serbia.

References

[1] Clemente P, Rinaldis D (1998) Protection of a Monumental Building Against Traffic-Induced Vibrations, *Soil Dynamics and Earthquake Engineering*, Vol.17, pp. 289-296

[2] Al-Hunaidi M, Rainer J H (1996) Control of Traffic-Induced Vibration in Buildings Using Vehicle Suspension Systems, *Soil Dynamics and Earthquake Engineering*, Vol. 15, pp. 245-254

[3] Crispino M, D'apuzzo M (2001) Measurement and Prediction of Traffic-Induced Vibrations in a Heritage Building, *Journal of Sound and Vibration*, Vol. 246 (2), pp. 319-335

[4] Hong Hao, T C Ang, Jay Shen (2001) Building Vibration to Traffic-Induced Ground Motion*, Building and Environment*, Vol. 36, pp. 321-336

[5] Dominguez J (1993) *Boundary Elements in Dynamics*, Computational Mechanics Publications, Boston

[6] Lysmer J, Ostadan F, Tabatabaie M, Tajirian F, Vahdani S (1999) *SASSI 2000, Theoretical Manual*

[7] Rastandi J I (2003) *Modelization of Dynamic Soil-Structure Interaction Using Integral Transform-Finite Element Coupling*, Lehrstuhl für Baumechanik der Technischen Universität München

[8] Radišić M, Nefovska-Danilović M, Petronijević M (2011) Application of integral transform method to calculate impedance functions, *Third Sebian Congress on*

Theoretical and Applied Mechanics, Vlasina Lake, 5-8 July (accepted for publication)

[9] Petronijević M, M Nefovska-Danilović (2006) *Geodinamička analiza osetljivosti objekata na dejstvo postojećih vibracija prema postojećim standardima i procena njihove osetljivosti na dejstvo lakog metroa*, GEOZAVOD i Građevinski fakultet Univerziteta u Beogradu

[10] J F Doyle (1997) *Wave Propagation in Structures*, Springer-Verlag, New York, Second edition

[11] Ronald N Bracewell (2000) *The Fourier Transform And Its Applications*, McGraw-Hill, Third Edition

[12] British Standard Institution (1992) *Guide to evaluation of human exposure to vibration in buildings* (1-80 Hz): BS6472:1992, London

[13] Penava D, Sigmund V, Petronijević M, Schmid G (2008) Vibration analysis of frame structure excited with Rayleigh waves using spectral elements, *International Scientific Symposium MODELING OF STRUCTURES*, Mostar13-15.11.2008, Croatia, pp. 545-558, (ISSN 1512-9322)

[14] Šavija Branko, Marija Nefovska-Danilović, Mira Petronijević (2010) Modalna analiza ramovskih konstrukcija primenom metode spektralnih elemenata, *Zbornik radova 13. kongresa DGKS,* Zlatibor-Čigota, 22-24.09.2010. s. 365-372, ISBN 978-86-85073-09-0

[15] Šavija Branko (2009) *Dinamička analiza ramovskih konstrukcija u frekventnom domenu primenom metode spektralnih elemenata*, Diplomski rad, Građevinski fakultet, Univerzitet u Beogradu, 2009.

[16] Schmid G, Tosecky A (2003) *Soil-Structure Interaction – Foundation Vibrations*, Lecture for the Master Course "Earthquake Engineering" at IZIIS, University SS. Cyril and Methodius Skopje

INFLUENCE OF TRANSVERSE SHEAR AND ROTARY INERTIA ON VIBRATION AND STABILITY OF CROSS-PLY LAMINATED PLATES

Ratko Pavlović[1], Ivan Pavlović[1], Vladimir Stojanović[1]
University of Niš, Faculty of Mechanical Engineering, A. Medvedeva 14, 18000 Niš, Serbia
e-mail:ratko@masfak.ni.ac.rs, pivan@ masfak.ni.ac.rs, stojanovic.s.vladimir@gmail.com

Abstract. In the present paper, by including two shear correction factors, vibration and stability of symmetric and antisymmetric cross-ply laminated plates are investigated. Natural frequency parameters and buckling coefficients are obtained for simply supported rectangular laminated plates. Numerical results are given as function of span-to-depth ratio, aspect ratio, cross-ply ratio, number of layers and ratio of the principal lamina stiffnesses. Shear deformation shown a considerable effect on natural frequencies and critical buckling load for cross-ply plates, whereas the rotary inertia effect was found to be negligible.

Keywords: Vibration, Stability, Laminated plates, Shear factors, Rotary inertia

1. Introduction

The potential of fiber-reinforced composite materials for use as structural members has inspired considerable research activity in the study of the response anisotropic laminated plates. Composite materials are very suitable for structural applications where high strength -to - weight and stiffness - to - weight ratios are required. Laminated composite materials are used as structural components in various applications (aerospace, automotive, marine, etc.).

The determination of natural frequencies and stability regions is of fundamental importance in the design of many structural components. It is necessary that the natural frequencies of vibration and buckling loading be determined accurately in order to obtain a design that results in virtually resonant-free structural components. In the classical laminate theory [1], which is an extension of the classical plate theory to laminated plates, one ignores the transverse stress components and models a laminate as an equivalent single layer. That theory is adequate for many engineering problems, but laminated plates made of advanced filamentary composite materials, like graphite-epoxy, are susceptible to thickness effects because their effective transverse shear moduli are significantly smaller than the effective elastic modulus along the fiber direction.

This high ratio of elastic modulus to shear modulus renders the classical laminate theory inadequate for the analysis of composite plates. Also, deformation due to transverse shear strains plays a significant role in the behavior of beams, plates and shells when a linear dimension or response mode wave length is of the same order as the thickness. For typical fibrous composite materials the transverse shear elastic modulus is less than 1/50 of the major in-surface normal modulus.

As is known from theory of elasticity, exact linear solutions of some laminated plates can be obtained by solving three-dimensional elasticity equations, but the procedure

becomes very cumbersome when the number of layers increases, and the analysis is computationally expensive and infeasible for practical use.

The problem of correction of shear on static and dynamic behavior of the laminated plates goes back to the papers of Young *at al.* [2] and Whitney and Pagano [3]. Pai [4] investigated the characteristics of shear warping functions, shear coupling effect and presented a general derivation and interpretation of shear correction factors of anisotropic laminates. The influence of rotatory inertia and transverse shear on dynamic instability domains was studied by Pavlović *at al.* [5], [6]. The thermally inducted parametric vibrations of laminated plates with shear effects due to time-dependent temperature with Gaussian and harmonic distributions were analyzed by Tylikowski [7]. By introducing velocity feedback and particular polarization profiles of piezoelectic sensors and actuators, a stabilization problem of beam with shear deformations and rotatory inertia effects was studied also by Tylikowski [8].

The purpose of the present paper is, by including two shear correction factors, the investigation vibration and stability of symmetric and antisymmetric cross-ply laminated plates.

2. Problem formulation

Let us consider the elastic, symmetrically or antisymmetrically laminated cross-ply rectangular plates. The plates are made up of many unidirectional layers stacked up in 0^o or 90^o with respect to a reference axis, as is shown in Fig. 1.

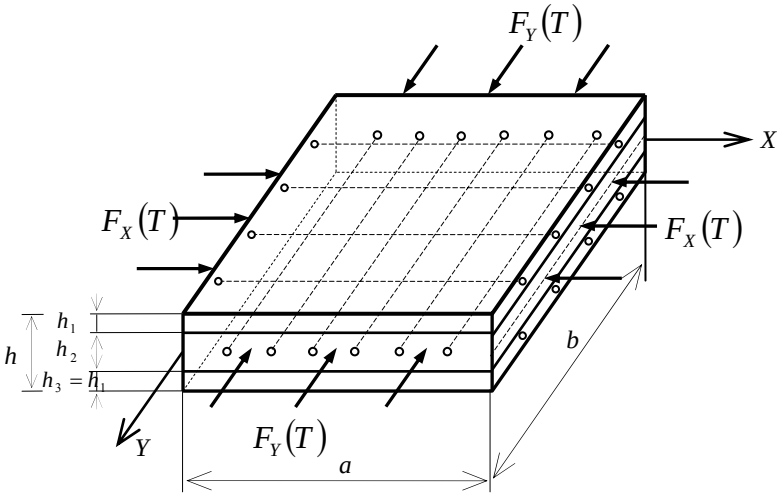

Fig. 1 Geometry and co-ordinate system of a three-layered cross-ply symmetric plate

The dynamic equilibrium equations, based on the first order shear deformation theory, after Whitney and Pagano [3], and Pai [4], are:

$$A_{11}\frac{\partial^2 U_o}{\partial X^2}+A_{66}\frac{\partial^2 U_o}{\partial Y^2}+\left(A_{12}+A_{66}\right)\frac{\partial^2 V_o}{\partial X\partial Y}+B_{11}\frac{\partial^2 \psi_x}{\partial X^2}=0, \tag{1}$$

$$\left(A_{12}+A_{66}\right)\frac{\partial^2 U_o}{\partial X\partial Y}+A_{66}\frac{\partial^2 V_o}{\partial X^2}+A_{22}\frac{\partial^2 V_o}{\partial Y^2}-B_{11}\frac{\partial^2 \psi_y}{\partial Y^2}=0, \tag{2}$$

$$\rho h\frac{\partial^2 W}{\partial T^2}-k_1A_{55}\left(\frac{\partial \psi_x}{\partial X}+\frac{\partial^2 W}{\partial X^2}\right)-k_2A_{44}\left(\frac{\partial \psi_y}{\partial Y}+\frac{\partial^2 W}{\partial Y^2}\right)+F_X(T)\frac{\partial^2 W}{\partial X^2}+F_Y(T)\frac{\partial^2 W}{\partial Y^2}=0, \tag{3}$$

$$I\frac{\partial^2 \psi_x}{\partial T^2}-B_{11}\frac{\partial^2 U_o}{\partial X^2}-D_{11}\frac{\partial^2 \psi_x}{\partial X^2}-D_{66}\frac{\partial^2 \psi_x}{\partial Y^2}-\left(D_{12}+D_{66}\right)\frac{\partial^2 \psi_y}{\partial X\partial Y}+k_1A_{55}\left(\psi_x+\frac{\partial W}{\partial X}\right)=0, \tag{4}$$

$$I\frac{\partial^2 \psi_x}{\partial T^2}-B_{11}\frac{\partial^2 V_o}{\partial Y^2}-\left(D_{12}+D_{66}\right)\frac{\partial^2 \psi_x}{\partial X\partial Y}-D_{66}\frac{\partial^2 \psi_y}{\partial X^2}-D_{22}\frac{\partial^2 \psi_y}{\partial Y^2}+k_2A_{44}\left(\psi_y+\frac{\partial W}{\partial Y}\right)=0, \tag{5}$$

where A_{11}, A_{12}, A_{22}, A_{44}, A_{55}, A_{66}, B_{11}, D_{11}, D_{12}, D_{22} and D_{66} are laminate stiffness coefficients, U_o, V_o are inplane displacements, W is the transverse displacement, ψ_x and ψ_y are bending slopes, k_1, k_2 are the shear correction factors associated with the shear stiffnesses A_{55} and A_{44}, respectively, ρ is the mass density, T is the time, $F_X(T)$ and $F_Y(T)$ are time-dependent compressing forces.

Boundary conditions corresponding to simply supported edges have the form:

$$\left.\begin{array}{ll} X=0, & a \\ Y=0, & b \end{array}\right\} \quad \begin{array}{l} W=0,\ \psi_y=0,\quad M_X=0,\quad V_o=N_X=0 \\ W=0,\ \psi_x=0,\quad M_Y=0,\quad U_o=N_Y=0 \end{array}, \tag{4}$$

where bending moments and stress resultsnts are

$$M_X=B_{11}\frac{\partial U_o}{\partial X}+D_{11}\frac{\partial \psi_x}{\partial X}+D_{12}\frac{\partial \psi_y}{\partial Y},$$
$$M_Y=-B_{11}\frac{\partial V_o}{\partial Y}+D_{12}\frac{\partial \psi_x}{\partial X}+D_{22}\frac{\partial \psi_y}{\partial Y}, \tag{5}$$

$$N_X = A_{11}\frac{\partial U_o}{\partial X} + A_{12}\frac{\partial V_o}{\partial Y} + B_{11}\frac{\partial \psi_x}{\partial X},$$
$$N_Y = A_{12}\frac{\partial U_o}{\partial X} + A_{22}\frac{\partial V_o}{\partial Y} - B_{11}\frac{\partial \psi_y}{\partial Y}.$$

The following parameters can be used to non-dimensionalize equations (1)-(3):

$$X = ax, \quad Y = by, \quad U_o = hu, \quad V_o = hv, \quad W = hw, \quad T = k_t t, \quad k_t = \sqrt{\frac{\rho h a^4}{D_{22}}}, \quad q = \frac{a}{b}, \quad s = \frac{h}{a},$$

(6)

$$a_{ij} = \frac{A_{ij}a^2}{D_{22}}, \quad b_{11} = \frac{B_{11}a}{D_{22}}, \quad d_{ij} = \frac{D_{ij}}{D_{22}}, \quad \left(f_x, f_y\right) = \frac{\left(F_X, F_Y\right)b^2}{D_{22}}, \quad e = \frac{I}{\rho h a^2}.$$

Now, they have the form:

$$a_{11}\frac{\partial^2 u}{\partial x^2} + a_{66}q^2\frac{\partial^2 u}{\partial y^2} + \left(a_{12} + a_{66}\right)q\frac{\partial^2 v}{\partial x \partial y} + \frac{b_{11}}{s}\frac{\partial^2 \psi_x}{\partial x^2} = 0,$$

(7)

$$\left(a_{12} + a_{66}\right)q\frac{\partial^2 u}{\partial x \partial y} + a_{66}\frac{\partial^2 v}{\partial x^2} + a_{22}q^2\frac{\partial^2 v}{\partial y^2} - \frac{b_{11}}{s}q^2\frac{\partial^2 \psi_y}{\partial y^2} = 0,$$

(8)

$$\frac{\partial^2 w}{\partial t^2} - \frac{k_1}{s}a_{55}\left(\frac{\partial \psi_x}{\partial x} + s\frac{\partial^2 w}{\partial x^2}\right) - \frac{k_2}{s}a_{44}q\left(\frac{\partial \psi_y}{\partial y} + sq\frac{\partial^2 w}{\partial y^2}\right) + f_x q^2\frac{\partial^2 w}{\partial x^2} + f_y q^4\frac{\partial^2 w}{\partial y^2} = 0$$

, (9)

$$e\frac{\partial^2 \psi_x}{\partial t^2} - d_{11}\frac{\partial^2 \psi_x}{\partial x^2} - d_{66}q^2\frac{\partial^2 \psi_x}{\partial y^2} - \left(d_{12} + d_{66}\right)q\frac{\partial^2 \psi_y}{\partial x \partial y} - b_{11}s\frac{\partial^2 u}{\partial x^2} + k_1 a_{55}\left(\psi_x + s\frac{\partial w}{\partial x}\right) = 0,$$

(10)

$$e\frac{\partial^2 \psi_y}{\partial t^2} - \left(d_{12} + d_{66}\right)q\frac{\partial^2 \psi_x}{\partial x \partial y} - d_{66}\frac{\partial^2 \psi_y}{\partial x^2} - q^2\frac{\partial^2 \psi_y}{\partial y^2} + b_{11}sq^2\frac{\partial^2 v}{\partial y^2} + k_2 a_{44}\left(\psi_y + sq\frac{\partial w}{\partial y}\right) = 0,$$

(11)

and boundary conditions:

$$\left.\begin{array}{l} x=0,\quad 1 \\ \\ y=0,\quad 1 \end{array}\right\} \begin{array}{l} w=0,\ \psi_y=0,\quad m_x=0,\quad v=n_x=0 \\ w=0,\ \psi_x=0,\quad m_y=0,\quad v=n_y=0 \end{array}, \tag{12}$$

where

$$m_x = b_{11}s\frac{\partial u}{\partial x} + d_{11}\frac{\partial \psi_x}{\partial x} + d_{12}q\frac{\partial \psi_y}{\partial y}, \qquad m_y = -b_{11}qs\frac{\partial v}{\partial y} + d_{12}\frac{\partial \psi_x}{\partial x} + q\frac{\partial \psi_y}{\partial y}, \tag{13}$$

$$n_x = a_{11}\frac{\partial u}{\partial x} + a_{12}q\frac{\partial v}{\partial y} + \frac{b_{11}}{s}\frac{\partial \psi_x}{\partial x},$$

$$n_y = a_{12}\frac{\partial u}{\partial x} + a_{22}q\frac{\partial v}{\partial y} - \frac{b_{11}}{s}q\frac{\partial \psi_y}{\partial y}.$$

By applying differential operators:

$$\begin{aligned} \ell_{11} &= a_{11}\frac{\partial^2}{\partial x^2} + a_{66}q^2\frac{\partial^2}{\partial y^2}, \quad \ell_{12} = (a_{12}+a_{66})q\frac{\partial^2}{\partial x \partial y}, \\ \ell_{22} &= a_{66}\frac{\partial^2}{\partial x^2} + a_{22}q^2\frac{\partial^2}{\partial y^2}, \quad \ell_{uv} = \ell_{11}\ell_{22} - \ell_{12}\ell_{12}, \end{aligned} \tag{14}$$

to the differential equations (7), (8), (11) and (12) we can eliminate in plane displacements u *and* v. Reduced sistem is:

$$\frac{\partial^2 w}{\partial t^2} - \frac{k_1}{s}a_{55}\left(\frac{\partial \psi_x}{\partial x} + s\frac{\partial^2 w}{\partial x^2}\right) - \frac{k_2}{s}a_{44}q\left(\frac{\partial \psi_y}{\partial y} + sq\frac{\partial^2 w}{\partial y^2}\right) + f_x q^2\frac{\partial^2 w}{\partial x^2} + f_y q^4\frac{\partial^2 w}{\partial y^2} = 0 \tag{15}$$

,

$$\begin{aligned} &e\frac{\partial^2 \ell_{uv}\psi_x}{\partial t^2} - d_{11}\frac{\partial^2 \ell_{uv}\psi_x}{\partial x^2} - d_{66}q^2\frac{\partial^2 \ell_{uv}\psi_x}{\partial y^2} - (d_{12}+d_{66})q\frac{\partial^2 \ell_{uv}\psi_y}{\partial x \partial y} + \\ &+ b_{11}^2\left(\frac{\partial^4 \ell_{22}\psi_x}{\partial x^4} + q^2\frac{\partial^4 \ell_{12}\psi_y}{\partial x^2 \partial y^2}\right) + k_1 a_{55}\left(\ell_{uv}\psi_x + s\frac{\partial \ell_{uv} w}{\partial x}\right) = 0, \end{aligned} \tag{16}$$

$$e\frac{\partial^2 \ell_{uv}\psi_y}{\partial t^2} - (d_{12}+d_{66})q\frac{\partial^2 \ell_{uv}\psi_x}{\partial x \partial y} - d_{66}\frac{\partial^2 \ell_{uv}\psi_y}{\partial x^2} - q^2\frac{\partial^2 \ell_{uv}\psi_y}{\partial y^2} +$$

(17)

$$+ b_{11}^2 q^2 \left(\frac{\partial^4 \ell_{12} \psi_x}{\partial x^2 \partial y^2} + q^2 \frac{\partial^4 \ell_{11} \psi_y}{\partial y^4} \right) + k_2 a_{44} \left(\ell_{uv} \psi_y + qs \frac{\partial \ell_{uv} w}{\partial y} \right) = 0,$$

and modified boundary conditiond have the form:

$$\left.\begin{array}{ll} x = 0, \quad 1 \\ \\ y = 0, \quad 1 \end{array}\right\} \quad \begin{array}{l} w = \dfrac{\partial^2 w}{\partial x^2} = \dfrac{\partial^4 w}{\partial x^4} = 0, \;\; \ell_{uv} \psi_y = 0, \quad \dfrac{\partial \ell_{uv} \psi_x}{\partial x} = 0 \\ \\ w = \dfrac{\partial^2 w}{\partial x^2} = \dfrac{\partial^4 w}{\partial x^4} = 0, \;\; \ell_{uv} \psi_x = 0, \quad \dfrac{\partial \ell_{uv} \psi_y}{\partial y} = 0 \end{array} .$$

(18)

3. Flexural Vibrations and Stability

The following set of displacements will satisfy differential equations (15)-(17) and the boundary conditions (18):

$$\psi_x(x,y,t) = \sum_{m,n=1}^{\infty} A_{mn} e^{i\omega_{mn} t} \cos \alpha_m x \sin \beta_n y, \tag{19}$$

$$\psi_y(x,y,t) = \sum_{m,n=1}^{\infty} B_{mn} e^{i\omega_{mn} t} \sin \alpha_m x \cos \beta_n y,$$

$$w(x,y,t) = \sum_{m,n=1}^{\infty} C_{mn} e^{i\omega_{mn} t} \sin \alpha_m x \sin \beta_n y.$$

By putting relations (19) into (15)-(17) we obtain homogenous set of algebraic equations which poseses nontrival solution if:

$$\Delta = \begin{vmatrix} H_{11} & H_{12} & H_{13} \\ H_{21} & H_{22} & H_{23} \\ H_{31} & H_{32} & H_{33} \end{vmatrix} = 0, \tag{20}$$

where

$$H_{11} = k_1 a_{55} \alpha_m^2 + k_2 a_{44} q^2 \beta_n^2 - \omega_{mn}^2 - f_x q^2 \alpha_m^2 - f_y q^4 \beta_n^2,$$

$$H_{12} = \frac{1}{s} k_1 a_{55} \alpha_m, \quad H_{13} = \frac{1}{s} k_2 a_{44} q \beta_n,$$

$$H_{21} = k_1 a_{55} s \alpha_m \ell_{uv}^{mn},$$

$$H_{22} = \left(k_1 a_{55} + d_{11} \alpha_m^2 + d_{66} q^2 \beta_n^2 - e \omega_{mn}^2 \right) \ell_{uv}^{mn} + b_{11}^2 \ell_{22}^{mn} \alpha_m^4, \tag{21}$$

$$H_{23} = H_{32} = \left(d_{12} + d_{66}\right) q \alpha_m \beta_n \ell_{uv}^{mn} - b_{11}^2 q^2 \alpha_m^2 \beta_n^2 \ell_{12}^{mn}, \quad H_{31} = k_2 a_{44} q s \beta_n \ell_{uv}^{mn},$$

$$H_{33} = \left(k_2 a_{44} + d_{66} \alpha_m^2 + q^2 \beta_n^2 - e \omega_{mn}^2\right) \ell_{uv}^{mn} + b_{11}^2 q^4 \ell_{11}^{mn} \beta_n^4,$$

and

$$\ell_{11}^{mm} = -\left(a_{11} \alpha_m^2 + a_{66} q^2 \beta_n^2\right), \qquad \ell_{22}^{mm} = -\left(a_{66} \alpha_m^2 + a_{22} q^2 \beta_n^2\right),$$
$$\ell_{uv}^{mm} = \ell_{11}^{mm} \ell_{22}^{mm} - \left(a_{12} + a_{66}\right)^2 q^2 \alpha_m^2 \beta_n^2.$$

4. Numerical results and discussion

The expression (20) gives the possibility to obtain natural freqencies and regions stability as the function of the geometric and mechanical characteristics of the plate.

Antisymmetric cross-ply laminated plates have N unidirectionally reinforced layers with principal material directions alternatively oriented at 0^0 and 90^0 to the laminate coordinate axes. The fiber direction of odd-numbered layers is the x-direction, and even-numbered y-direction of the laminate. We will consider the case of odd-numbered layers with equal thickness and even-numbered ones with equal thickness, but not necessarily the same as that of the odd-numbered layers. Dimensionless laminate stiffnesses are:

$$a_{11} = \frac{12\left(M + F\right)}{\left(1 + M\right)\left[\left(1 - F\right)P + F\right]} \frac{1}{s^2}, \quad a_{12} = \frac{12 \nu_{12} F}{\left(1 - F\right)P + F} \frac{1}{s^2}, \quad a_{22} = \frac{12\left(1 + MF\right)}{\left(1 + M\right)\left[\left(1 - F\right)P + F\right]} \frac{1}{s^2},$$

$$a_{66} = \frac{12\left(1 - \nu_{12}^2 F\right)F}{\left(1 - F\right)P + F} \frac{G_{12}}{E_2} \frac{1}{s^2}, \quad b_{11} = \frac{12M\left(F - 1\right)}{N\left(1 + M\right)^2\left[\left(1 - F\right)P + F\right]} \frac{1}{s},$$

$$d_{11} = \frac{\left(F - 1\right)P + 1}{\left(1 - F\right)P + F}, \quad d_{12} = \frac{\nu_{12} F}{\left(1 - F\right)P + F}, \quad d_{66} = \frac{\left(1 - \nu_{12}^2 F\right)F}{\left(1 - F\right)P + F} \frac{G_{12}}{E_2},$$

$$a_{44} = \frac{12\left(1 - \nu_{12}^2 F\right)F}{\left(1 - F\right)P + F} \frac{G_{23}}{E_2} \frac{1}{s^2}, \quad a_{55} = \frac{12\left(1 - \nu_{12}^2 F\right)F}{\left(1 - F\right)P + F} \frac{G_{13}}{E_2} \frac{1}{s^2}, \tag{22}$$

$$R = \frac{1}{1 + M} + \frac{8M\left(M - 1\right)}{N^2\left(1 + M\right)^3}, \tag{23}$$

where N is the total number of layers, $F = E_2 / E_1$ is the ratio of principal lamina stiffnesses, E_1 and E_2 are major and minor Young's modulus, G_{12}, G_{23} and G_{13} are shear moduli, ν_{12}, $\nu_{21} = \nu_{12} F$ are Poisson's coefficients, and M is the cross-ply ratio, defined as the ratio of the total thickness of odd-numbered layers to total thickness of even-numbered layers:

$$M = \frac{\sum_{i=odd} h_i}{\sum_{i=even} h_i}. \tag{24}$$

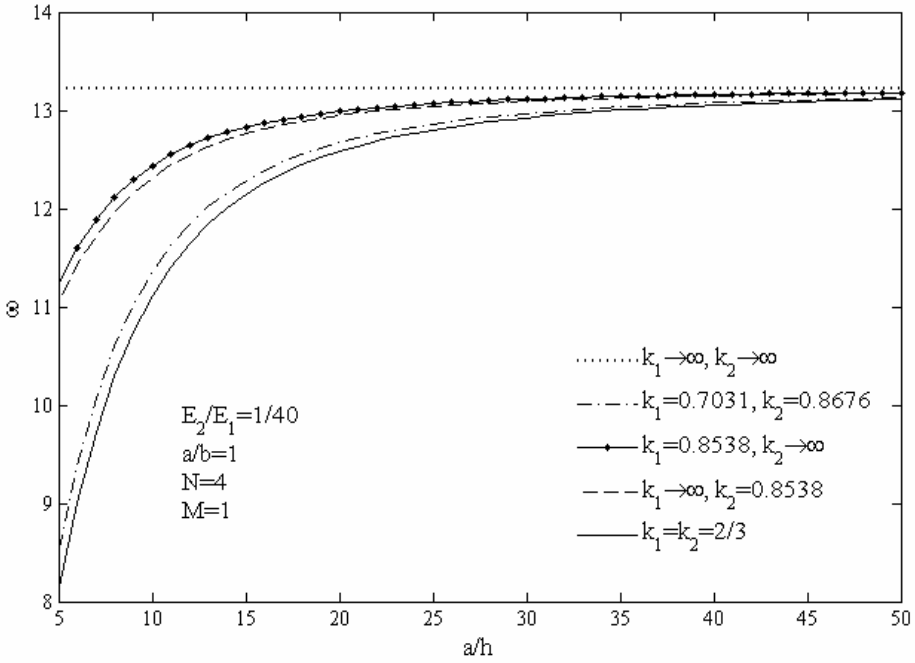

Fig. 2 Fundamental vibration frequency for a 4 layer square cross-ply plate

In Fig. 2 are shown fundamental vibration frequency for a graphite/epoxy regular cross-ply square laminated plate with material properties:

$$F = E_2 / E_1 = 1/40, \quad G_{12} / E_2 = G_{23} / E_2 = 0.6, \quad G_{13} / E_2 = 0.5, \quad \nu_{12} = 0.25,$$

with various shear correction factors. Neglecting of transverse shear $(k_1 \to \infty, k_2 \to \infty)$ can be justified for length-to-thickness ratio $a/h \geq 50$, and such neglecting for $a/h \leq 30$ can be serious error.

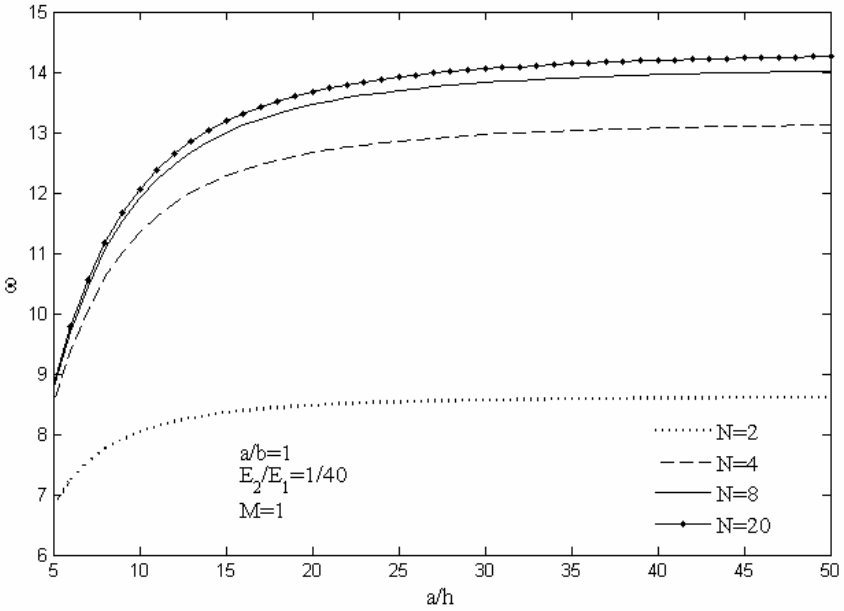

Fig. 3 Fundamental vibration frequency for a square cross-ply plate with various number of layers, $(k_1 = 0.7031, k_2 = 8676)$

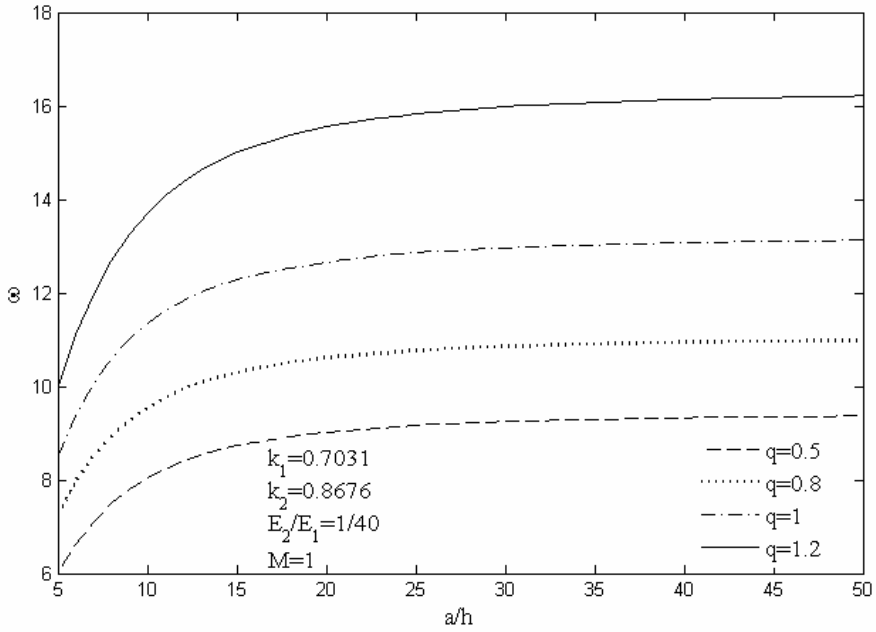

Fig. 4 Fundamental vibration frequency for a 4 layer cross-ply plate

with various plate aspect ratio

In Fig. 3 are shown fundamental vibration frequency for the same graphite/epoxy regular cross-ply laminated plate with various number of layers. Fundamental frequencies are the smallest for two-layered plate, and when number of layers increases, frequencies are closer and diference between line is smaller. Reason for this is because coupling stiffness b_{11} decreases when number of layers increases.

In Fig. 4 are shown fundamental vibration frequency for the same graphite/epoxy regular cross-ply laminated plate with various plate aspect ratio. Fundamental frequencies increase when plate aspect ratio increase.

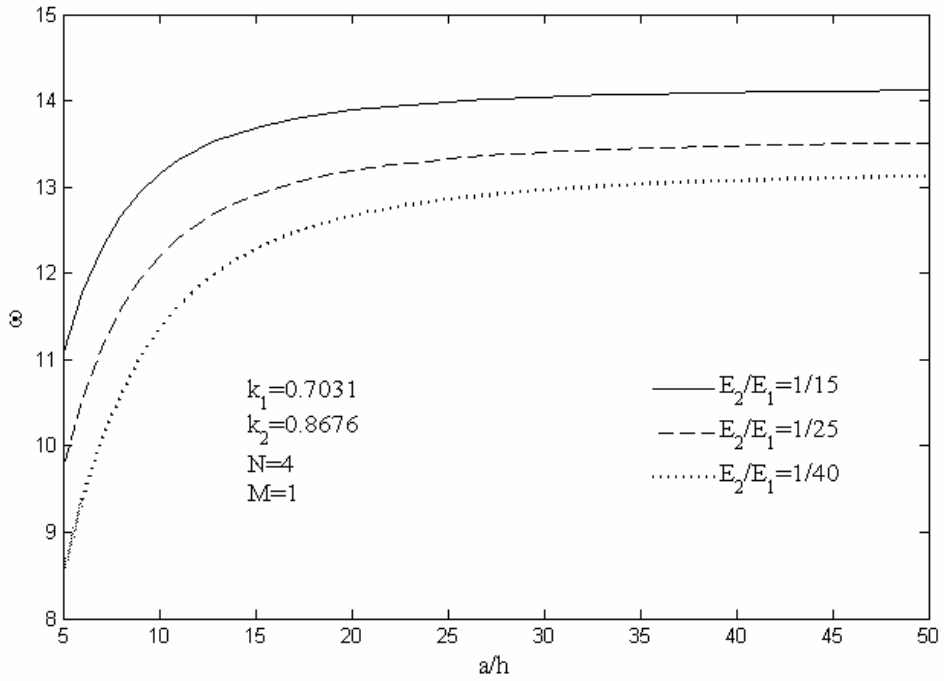

Fig. 5 Fundamental vibration frequency for a 4 layer cross-ply plate with various ratio of the principal lamina stiffnesses

In Fig. 5 are shown fundamental vibration frequency for the different graphite/epoxy regular cross-ply laminated plate with previous and new material properties:

$$F = E_2 / E_1 = 1/25, \quad G_{12} / E_2 = G_{13} / E_2 = 0.5, \quad G_{23} / E_2 = 0.2, \quad \nu_{12} = 0.25,$$
$$F = E_2 / E_1 = 1/15, \quad G_{12} / E_2 = G_{13} / E_2 = 0.5, \quad G_{23} / E_2 = 0.35, \quad \nu_{12} = 0.3.$$

It is evident that fundamental frequencies are smaller for materials with smaller ratio of the principal lamina stiffnesses.

5. Conclusion

This paper discusses vibrations of the cross-ply antisymmetrically laminated plates when transverse shear is taken into account.

The influence of transverse shear is very expressive when the ratio of principal lamina stiffnesses is high, e.g. for graphite/epoxy composite plates, but even for a laminated composite material as glass/epoxy, whose ratio of principal lamina stiffnesses is much smaller, neglecting the transverse shear causes an error.

The increase of the number of layers and plate aspect ratio leads to the increase of fundamental frequencies.

Acknowledgment

This work is supported by Ministry of Science of Republic Serbia, through the project No. 174011.

References

[1] Jones, R. M. (1975), *Mechanics of Composite Materials*, Scripta Book Company, Washington, D. C.

[2] Yang, P. C., Norris, C. H., Stavsky, Y. (1966), *Elastic Wave Propagation in Heterogeneous Plates*, Int. J. Sol. Struct., 2, pp. 665-684.

[3] Whitney, J. M., Pagano, N. J. (1970), *Shear Deformation in Heterogeneous Anisotropic Plates*, ASME J. Appl. Mech., 37, pp. 1031-1036.

[4] Pai, P. (1995), *A New Look at Shear Correction Factors and Warping Functions of Anisotropic Laminates,* Int. J. of Sol. Struct., 32(16), pp. 2295-2313.

[5] Pavlović, R., Kozić, P., Rajković, P. (2001), *Influence of Transverse Shear on Stochastic Instability of Viscoelastic Beam*, Int. J. of Sol. Struct., 38, pp. 6829-6837.

[6] Pavlović, R., Pavlović, I. (2005), *Influence of Rotatory Inertia and Transverse Shear on Stochastic Instability of the Cross-Ply Laminated Beam,* Int. J. of Sol. Struct., 42, pp. 4913-4926.

[7] Tylikowski, A. (2003), *Shear Deformation Effects on Thermally Induced Instability of Laminated Plates*, Journal of Thermal Stresses, 26, pp. 1251 - 1261.

LASER SHOCK PEENING OF DEFORMED N-155 SUPERALLOY

S. Petronic[1], A. Milosavljevic[2], A. Kovacevic[3], B. Grujic[4], K. Colic[5]

[1] Innovation centre, Faculty of Mechanical Engineering,
The University of Belgrade, Kraljice Marije 16, 11120 Belgrade 35
e-mail: sanjapetronic@yahoo.com
[2] Faculty of Mechanical Engineering,
The University of Belgrade, Kraljice Marije 16, 11120 Belgrade 35
e-mail: amilosavljevic@mas.bg.ac.rs
[3] Institute of Physics
Pregrevica 118, 11080 Belgrade
e-mail: Aleksander.Kovacevic@ipb.ac.rs
[4] Innovation centre, Faculty of Mechanical Engineering,
The University of Belgrade, Kraljice Marije 16, 11120 Belgrade 35
e-mail: bgrujic@mas.bg.ac.rs
[5] Innovation centre, Faculty of Mechanical Engineering,
The University of Belgrade, Kraljice Marije 16, 11120 Belgrade 35
e-mail: kcolic@mas.bg.ac.rs

Abstract. Iron base superalloy N – 155 samples were cut from the turbine blade after longtime service at elevated temperature and pressure. After work hardening of material, the laser surface treatment was applied with the aim to achieve better mechanical properties of material and recover material after longtime service. The samples were observed by scanning electron microscopy (SEM) and analyzed by energo-dispersive spectrometry (EDS). Vickers microhardness tests were performed. In this paper, microstructures arising after various pulse frequencies were analyzed and compared and causes of the treatment type were explained.

1. Introduction

A large number of superalloys have been developed for application in gas turbine aero engines; among these, N-155 is an important precipitation hardening iron base superalloy, with good ductility, strength, excellent oxidation and corrosion resistance, and can be readily fabricated and machined. These components are fabricated from plate/sheet of this alloy. The formability and weldability of the alloy hence become important factors for the fabrication of these components. Formability of metals and alloys is known to be strongly related to their work hardening behaviour [1].

Laser shock peening (LSP) is a relatively new technology to classical treatments for improving fatigue, corrosion and wearing resistance of metals. The effect on target material is mainly achieved through mechanical effect produced by shock waves [2]. It is well suited for precisely controlled treatment of localized fatigue critical areas, such as holes, notches, fillets and welds [3].

The principle of LSP is to use a high intensity laser and suitable overlays to generate high pressure shock waves on the surface of the workpiece [4].

For LSP the surface of the specimen is pre-coated with a thin layer of material highly absorptive at operating wavelength of the laser beam, such as black paint [5] and transparent material, such as water or glass.

2. Experiment

The experiment was carried out on iron base superalloy samples cut from turbine blades after 10000h of exploitation. Dimensions of samples were 20x10x1.2 mm. Chemical composition of samples is listed in Table 1.

Table 1. Chemical composition of superalloy N – 155.

Ni	Cr	Mo	Mn	Si	Fe	C	Al	Co	W	Nb
20.0	21.0	3.0	1.5	0.5	30.0	0.15	0.15	20.0	1.2	2.0

The samples were cold deformed by rolling and laser surface treated.
The samples were exposed to various numbers of laser pulses with different repetition frequencies (Tab. 2).

Table 2. The number of pulses and different pulse frequencies used in the experiment.

Repetition frequency (Hz)	1	2	4
Number of pulses	12	12	16

The experiment setup is presented in Fig. 1. The sample was coated with an absorptive and protective layer (black paint), placed in the container filled with distilled water (a transparent layer) and exposed to pulsed laser beam (Nd^{3+}:YAG, wavelength 532 nm , pulse energy 37 mJ, and duration 10 ns). Protective overlay is used for two reasons: (1) to absorb the incident thermal energy, expand and transfer the shock wave to the metal target and (2) to protect the metal target from the heat influence of the incident [5]. The implementation of the transparent layer increases the plasma pressure by a trapping-like effect on the plasma expansion.

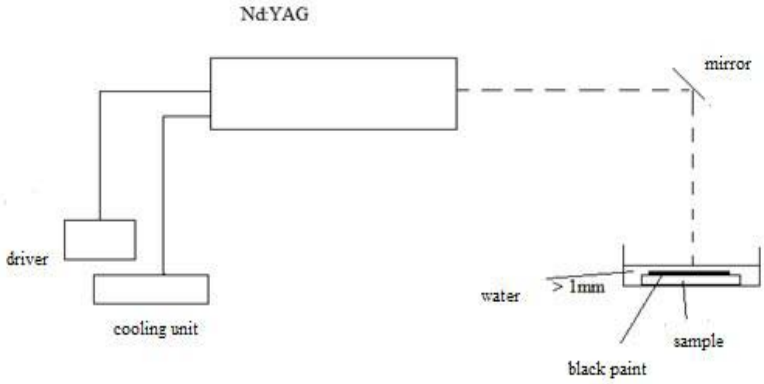

Fig. 1. The experimental setup.

The material was treated with nearly square laser spot, as there is no focus point of release waves. The residual stress drop will not be as remarkable as that treated by a round laser

spot. Using square laser spots should attenuate the simultaneous focalization of release waves and decrease the residual stress drop at the center of the laser shocked zone [6].
The microstructure was observed by scanning electron microscope – model JEOL JSM-5800, and analyzed by EDS. Microhardness measurement was performed by Vickers using the apparatus – model ZWIK – Edman Weltzar and under load of 0.5 N.

3. Result and discussion

Figures 1 and 2 show the initial microstructure of N-155 superalloy cut from turbine blades after longtime service. The structure is not smooth and homogeneous, and chromium carbides are concentrated at the surface due to long exposure to adverse working conditions.
The gaps between the grains are obvious that are suitable for the creation of microcracks which during the time and working conditions give rise to cracks. Several areas of the inhomogeneity are visible in the microstructure, the areas with micro-pores of up to 9μm in size.
Figure 2 shows the microstructure presented in Fig. 1 magnified 3 times. The inhomogeneity of the structure and different orientation of grains is clearly obvious. At some parts, there are the flower colonies that merge and grow into one grain.

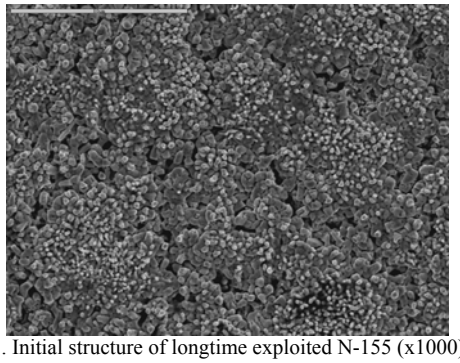

Figure 1. Initial structure of longtime exploited N-155 (x1000). SEM.

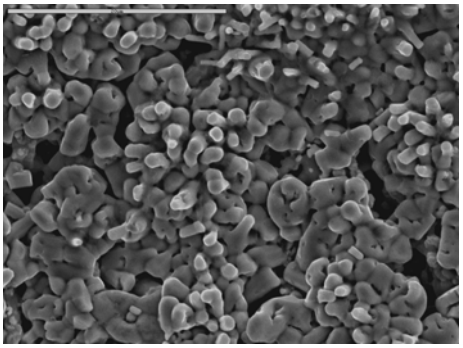

Figure 2. Initial structure of longtime exploited N-155 (x1000). SEM.

Figures 3 and 4 show the microstructure of superalloy N-155 after longtime service and plastic deformation by rolling. Strain ratio was low and therefore the grains do not have the same orientation.

During plastic deformation of metals, dislocations, which move along a particular slip plane can not move directly from one grain to another in a straight line. The slide line change the direction at the grain boundaries. Therefore, every grain has its own group of dislocations on their own priority slip planes. With greater deformation applied the grains change their shape and size due process of sliding. Initially, the grains had a spherical shape, and after deformation the grains are elongated in the direction of force, forming the directed structure, caused by moving of sliding planes [7].

When deformation occurs, the certain microconstinutents elongate. Ductile and tough crystals follow the effect of acting forces, and the brittle microconstituents crush, and their parts are arranged in the direction of material flow. During plastic deformation, tough grains change the shape only, but not the volume [8].

Tensile strength, yield strenght and hardness of material increase with the degree of deformation while the elongation and transverse contraction decrease. With increasing grade of deformation the impact strength, Young modulus and density decreace, while electrical resistance, coercive force and hysteresis loss incease [9].

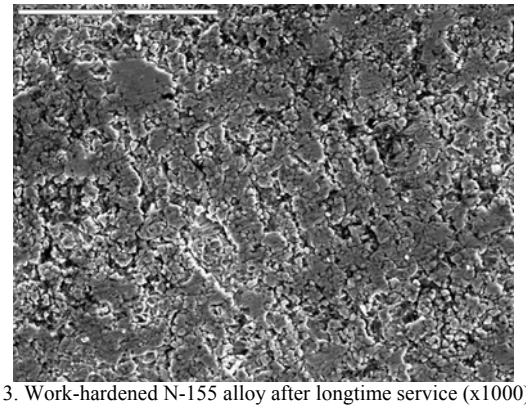

Figure 3. Work-hardened N-155 alloy after longtime service (x1000).SEM.

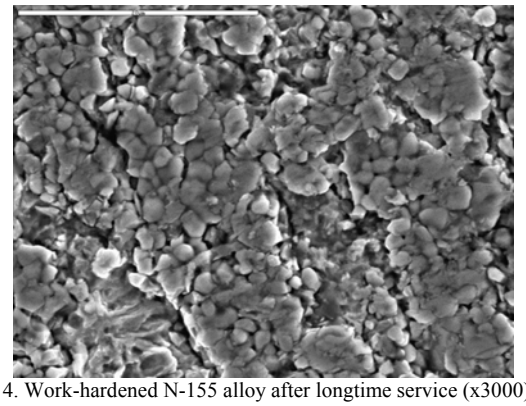

Figure 4. Work-hardened N-155 alloy after longtime service (x3000).SEM.

Table 3 lists the results of EDS analysis of the whole area in Figure 4. The Table 3 indicates increased content of Cr and Fe, as well as presence of S.
It is assumed that these types of carbides are $(Cr, Fe)_xC_y$ probably cementite-type. The appearance of sulfur is not related to Mn which is in smaller quantities, but it is assumed that the complex particles M_xC_y + MS are formed.

Table 3. The EDS results of the whole area in Figure 4

element	Si	S	Cr	Mn	Fe	Co	Ni
the area in Fig.4	0.84	0.64	32.58	0.94	41.22	12.66	11.12

Figure 5 shows the microstructure further strengthened by the laser mechanical treatment in order to improve the fatigue strength and resistance to intergranular corrosion, which can not be achieved by rolling. The principle of LSP is to use a high intensity laser and suitable overlays to generate high pressure shock waves on the surface of the workpiece.
The maximum compressive residual stress is often formed at the surface of the workpiece and decreases in magnitude with the increase of the depth below the surface. The transient shock waves can also induce microstructure changes near the surface and cause high density of dislocations to be formed. The combined effect of the microstructure changes and dislocation entanglement contribute to an increase in the mechanical properties near the surface. The compressive residual stresses improve the resistance to corrosion fatigue. An advantage of LSP is that the magnitude of affected depth is very deep as compared with conventional shot peening [2].
However, laser treatment has helped change the shape of grains, almost returning them in the form they had prior plastic deformation by rolling. Still, the grains has elongated shape and the material keep the advantages gained by work hardening.
It is supposed that combining of work hardening and laser shock peening mechanical properties would be improved, better that is posssible by applying only one of them at the time.
Figure 6 shows the microstructure of the Figure 5 mignified three times. Table 4 lists the results of EDS analysis in the areas 12 and 13. Point 12 is (Cr, Fe)xCy carbide, while the point 13 is Cr_xC_y carbide. It can be concluded that the laser mechanical processing decompose carbides (Cr, Fe), and prevail Cr_xC_y carbides.

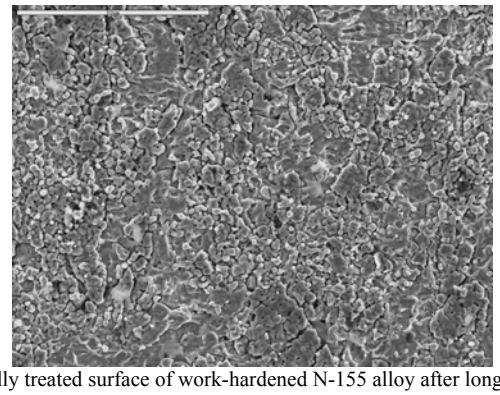

Figure 5. Laser mechanically treated surface of work-hardened N-155 alloy after longtime service (x1000).SEM.

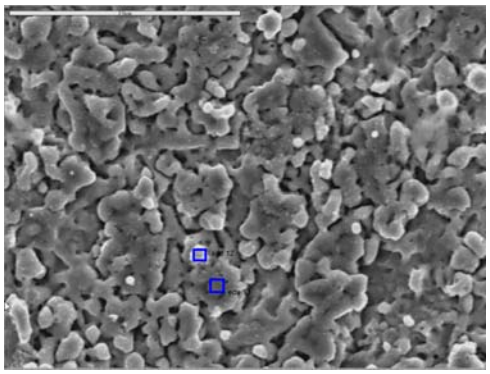

Figure 6. Laser mechanically treated surface of work-hardened N-155 alloy after longtime service (x3000).SEM.

Table 4. The EDS results of the whole area in Figure 6

	Si	S	Cr	Mn	Fe	Co	Ni
Eds 1	0.70	0.67	39.88	0.95	35.19	12.33	10.28
Eds 2	0.50	0.64	47.02	1.13	32.30	11.31	7.09

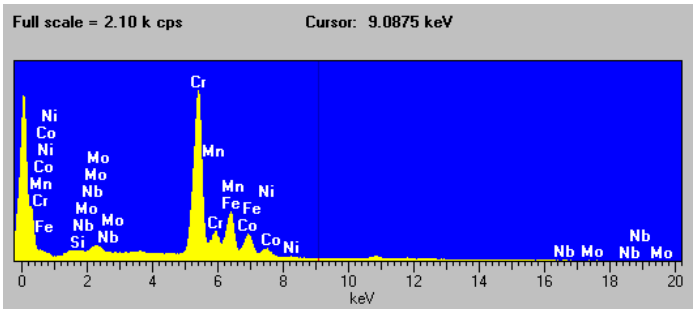

Fig 7. The EDS pattern of point 1 in Fig. 6

Figure 7 shows the EDS pattern of point 1 in Figure 6 nad listed in Table 4.
Figure 8 shows the laser thermomechanical treatment. After the laser beam melted protective layer, the action of the laser continued and there was a thermal effect. The laser pulse frequency was 4Hz. The part of material where the highest laser beam density was applied is melted. In this area there has been a segragation of Co and Ni as shown in Table 5, while the content of Co is quite small.
In the part that is not melted the grain boundaries are still visible, although the grains are much larger and irregularly shaped. Lighter grains (point 15) are the types of carbides $(Cr, Fe)_xC_y$. Form of elongated grains is due to rolling deformation. Laser beam has different affect to the grain look with pulse frequency of 4Hz and thermomechanical treatment then with pulse frequency of 1Hz and mechanical treatment.

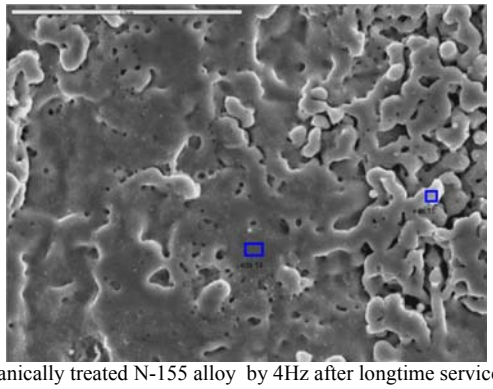

Figure 8. Laser mechanically treated N-155 alloy by 4Hz after longtime service and work hardening (x3000).SEM.

Table 5. The EDS results of the whole area in Figure 8

	Si	S	Cr	Mn	Fe	Co	Ni
Eds 1	1.97	0.86	9.40	0.51	34.51	23.38	29.36
Eds 2	0.36	0.56	51.02	1.13	29.56	11.67	5.68

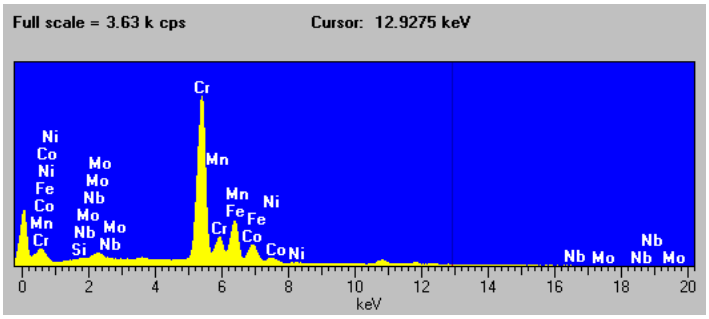

Figure 9. The EDS pattern of point 1 in Fig. 8

Figure 9 shows the EDS pattern of point 1 in Figure 8 nad listed in Table 5.
In this paper vickers microhardness testing of initial material N-155 (after longtime service), after work hardenning and after laser surface treatment wea performed. The microhardness of initial material was 240 $HV_{0.5.}$ the process of work hardening by rolling increased the value to 285 $HV_{0.5}$, while the laser shock peening had slightly effect on microhardness increasment – 290 $HV_{0.5}$, after it was increased by plastic deformation.

4. Conclusion

The samples of N-155 superalloy were cut from turbine blades after longtime service. The structure is not homogeneous,there are the gaps and micropores between the grains.
The work hardening by rolling was applied causing directed structure and elongated grains. It is assumed that these types of carbides are $(Cr, Fe)_xC_y$ probably cementite-type that the complex particles M_xC_y + MS are formed.

Laser surface treatment has helped change the shape of grains, almost returning them in the form they had prior plastic deformation by rolling. Still, the grains has elongated shape and the material keep the advantages gained by work hardening. It is supposed that combining of work hardening and laser shock peening mechanical properties would be improved, better that is posssible by applying only one of them at the time. Also, the laser mechanical processing decompose carbides (Cr, Fe), and prevail Cr_xC_y carbides.
The process of work hardening by rolling increased the value of microhardness. The laser shock peening had slightly effect on microhardness increasment after it was increased by plastic deformation.

Acknowledgement. This work was supported by the Ministry of Science of the Republic of Serbia under contract number TR-35040.

References

[1] Bhadeshia H.K.D.H. (1997) Recrystallisation of practical mechanically alloyed iron-base and nickel-base superalloys, Materials Science and Engineering A, 223, 64-77.
[2] K. Ding, L. Ye (2006) Laser shock peening, Performance and process simulation, Woodhead publishing limited, Cambridge England.
[3] Hu Y, Gong C, Yao Z, Hu J. (2009) Investigation on the non-homogeneity of residual stress field induced by laser shock peening. *Surface & Coatings Technology* 203, 3503-3509.
[4] Warren AW, Guo YB, Chen SC (2008) Massive parallel laser shock peening: Simulation, analysis, and validation. *International Journal of Fatigue,* 30, 188-197.
[5] Kovacevic A, Petronic S, Sedmak A, Milosavljevic A, Popovic M (2010) Modifikacija mehaničkih osobina austenitnih materijala – superlegure nikla, železa i nerđajući čelik – nanosekundnim laserskim impulsima, *Fotonika 2010, Beograd, book of abstract*, 11.
[6] Petronic S (2010) *Uticaj termičke i laserske obrade na promene u mikrostrukturi superlegura nikla* -PhD thesis, Faculty of Mechanical Engineering, University of Belgrade.
[7] Drobnjak Dj (1980) *Fizička metalurgija*, Faculty of Technology and Metalurgy, University of Belgrade.
[8] Cahn R and Haasan P (1996) *Physical Metallurgy*, Elsevier Science B.V.
[9] Rösler J, Harders H, Bäker M (2007) *Mechanical Behaviour of Engineering Materials*, Springer-Verlag Berlin Heidelberg.

APPLICATION OF INTEGRAL TRANSFORM METHOD TO CALCULATE IMPEDANCE FUNCTIONS

Marko Radišić[1], Marija Nefovska-Danilović[2], Mira Petronijević[3]

[1]Faculty of Civil Engineering
University of Belgrade, Bulevar kralja Aleksandra 73, 11000 Belgrade
e-mail: mradisic@grf.rs
[2]Faculty of Civil Engineering
University of Belgrade, Bulevar kralja Aleksandra 73, 11000 Belgrade
e-mail: marija@grf.rs
[3]Faculty of Civil Engineering
University of Belgrade, Bulevar kralja Aleksandra 73, 11000 Belgrade
e-mail: pmira@grf.rs

Abstract. To solve vibration problems of structure founded on the soil, the dynamic behavior of the soil needs to be understood and an accurate dynamic stiffness model of the soil has to be developed. Frequency dependent dynamic stiffness matrix of the massless, f exible soil-structure interface can be calculated analytically or numerically, depending on the complexity of the problem, using Boundary Element Method [1] or Thin Layer Method [3]. In this paper the impedance functions of a stiff rectangular foundation laying on a half-space are determined with the help of the Integral Transform Method (ITM) [4]. The Integral Transform Method is an eff cient method to calculate wave propagation in an elastic homogeneous, or layered half-space. By the use of the decomposition of Helmholtz, the Lamé's equations of elastodynamics are converted to a system of decoupled partial differential wave equations in space-time domain. With the help of a threefold Fourier Transform in the wave number-frequency domain wave equations can be transformed into a system of three decoupled ordinary differential equations which can be solved in the transformed domain. The results in the original domain can be f nally obtained by an Inverse Fourier Transform. Using ITM method the dynamic stiffness of f exible foundation are determinate f rst. After that the impedance functions of the stiff foundation are obtained using kinematic transformation matrix. The obtained results are compared with impedance functions from literature.

1. Introduction

1.1. Impedance

Impedance can be any kind of resistance to wave oscillation. For example, electrical impedance can be calculated as a ratio between voltage and current, acoustic impedance as a ratio between sound pressure and particle velocity, etc. For the purpose of this paper, mechanical impedance is calculated as a ratio between force and response quantity, where the response quantity is displacement

$$Z_M = \frac{force}{response\ quantity} \tag{1}$$

1.2. History of Impedance Functions

Impedance functions are frequency dependent foundation dynamic stiffnesses functions used in the dynamic soil-structure interaction problems. Those functions were f rst introduced by *Lamb*, 1904. He studied the vibrations of a linear elastic half-space due to a harmonic load acting on a point. In 1936, *Reissner* analyzed the response to a vertical harmonic excitation of a plate placed at the surface of a homogeneous elastic half-space. He was the f rst to notice the existence of energy dissipated by radiation. Between 1953 and 1956, *Sung*, *Quilan*, *Arnold* and *Bycroft* were working on generalization of the work of *Reissner* by introducing the six degrees of freedom of the footing. Ten years later, *Hsieh* and *Lysmer* introduced for the f rst time the idea that soil - footing vibrations in vertical direction can be represented with a single-degree-of-freedom system which stiffness and damping are independent of frequency - *Lysmer's analogy*. This approach was extended to all degrees of freedom by *Richart* and *Whitman*. In order to solve soil-structure interaction problems, many numerical approaches are being developed form the beginning of 60's [6]. The most successful ones are *Finite Element Method - FEM* and *Boundary Element Method - BEM*. The impedance functions for different type of foundations could be obtained using one of the before mention methods [5], [7].

1.3. Integral Transform Method

It is clear that FEM is widely applicable and eff cient, but there are some f elds where is not very suitable to use FEM. For example, while analyzing the behavior of a layered half-space due to a dynamic loading, as the soil is semi-inf nite and some kind of boundary conditions are needed to account Sommerfeld's radiation conditions, it is more convenient to use *Integral Transform Method* (ITM). ITM is based on solving the Lamé's elastodynamics equations of half-space using the Helmholtz potentials and Fourier transformations. It is very eff cient solution technique which leads to a better understanding of the physical nature of the problem, which can be integrated into FEM or BEM approaches [2]. On the other hands ITM has a very restricted domain for application.

2. Propagation of Waves in Continuum

In general, the system of equations of motion of an elastic continuum is nonlinear, but, many wave propagation effects in elastic solids can be adequately described by a linearized theory. The system of equations governing the motion of linearly elastic a homogeneous isotropic solid are obtained from the stress-equation of motion, Hooke's law and strain-displacement relations, in the form

$$\mu u_{i,jj} + (\lambda + \mu) u_{j,ji} = \rho \ddot{u}_i \tag{2}$$

where λ and μ are two material parameters known as *Lamé*'s constants

$$\mu = \frac{E}{2(1+\nu)}; \qquad \lambda = \nu \frac{E}{(1+\nu)(1-2\nu)} \tag{3}$$

while E is *Young*'s modulus and ν is *Poisson*'s ratio.
In vector notation the equation (2) can be written as:

$$(\lambda + \mu) \nabla \nabla \cdot \boldsymbol{u} + \mu \nabla^2 \boldsymbol{u} = \rho \ddot{\boldsymbol{u}} \tag{4}$$

The equilibrium equations, the kinematic and constitutive relations and hence, the *Navier*'s equation, must be satisf ed at every interior point of the undeformed body, i.e. in the domain Ω. On the surface S of the undeformed body, boundary conditions must be satisf ed, also.
The system of equations (4) couples the three displacement components. It can be uncoupled using *Helmholtz* decomposition, which states that any vector $\boldsymbol{u}$ can be written as a sum of gradient of a scalar potential $\phi(x,t)$ and the curl of a vector potential $\boldsymbol{\Psi}(x,t)$ as:

$$\boldsymbol{u} = \nabla\phi + \nabla\times\boldsymbol{\Psi} \tag{5}$$

The scalar potential $\phi(x,t)$ and the components of vector potential $\Psi_i(x,t),\ i = x,y,z$ are coupled through the boundary conditions.
Substitution of (5) into the f eld equation (4) yields

$$\mu\nabla^2[\nabla\phi + \nabla\times\boldsymbol{\Psi}] + (\lambda+\mu)\nabla\nabla\cdot[\nabla\phi + \nabla\times\boldsymbol{\Psi}] = \rho[\nabla\ddot{\phi} + \nabla\times\ddot{\boldsymbol{\Psi}}] \tag{6}$$

Since that $\nabla\cdot\nabla\times\boldsymbol{\Psi} = 0$, one obtains upon rearranging terms

$$\nabla[(\lambda+2\mu)\nabla^2\phi] + \nabla\times\mu\nabla^2\boldsymbol{\Psi} = \rho\nabla\ddot{\phi} + \rho\nabla\times\ddot{\boldsymbol{\Psi}} \tag{7}$$

The displacement representation (5) satisf es the equation of motion if

$$\nabla^2\phi - \frac{1}{c_p^2}\ddot{\phi} = 0 \tag{8}$$

and

$$\nabla^2\boldsymbol{\Psi} - \frac{1}{c_s^2}\ddot{\boldsymbol{\Psi}} = 0 \tag{9}$$

In these equations of motion c_p is the velocity of *dilatational (longitudinal) wave* or *P-wave*:

$$c_p = \sqrt{\frac{\lambda+2\mu}{\rho}} \tag{10}$$

c_s is the velocity of *distorsional (shear) wave* or *S-wave*:

$$c_s = \sqrt{\frac{\mu}{\rho}} \tag{11}$$

and ∇^2 is the Laplacian:

$$\nabla^2 = \frac{\partial^2}{\partial x^2} + \frac{\partial^2}{\partial y^2} + \frac{\partial^2}{\partial z^2} \tag{12}$$

The equation (5) can be written in the matrix form

$$\begin{bmatrix} u_x \\ u_y \\ u_z \end{bmatrix} = \begin{bmatrix} \frac{\partial}{\partial x} \\ \frac{\partial}{\partial y} \\ \frac{\partial}{\partial z} \end{bmatrix}\phi + \begin{bmatrix} 0 & -\frac{\partial}{\partial z} & \frac{\partial}{\partial y} \\ \frac{\partial}{\partial z} & 0 & -\frac{\partial}{\partial x} \\ -\frac{\partial}{\partial y} & \frac{\partial}{\partial x} & 0 \end{bmatrix}\begin{bmatrix} \Psi_x \\ \Psi_y \\ \Psi_z \end{bmatrix} \tag{13}$$

The four potential f elds ϕ, Ψ_x, Ψ_y and Ψ_z are not uniquely determined by the three displacements u_x, u_y and u_z. Usually, but not always, the relation $\nabla\cdot\boldsymbol{\Psi} = 0$, is taken as the additional constraint condition. Here, as a special case, Ψ_z is set to zero. Then, the equation (13) can be written as

$$\begin{aligned} u_x &= \phi_{,x} - \Psi_{y,z} \\ u_y &= \phi_{,y} + \Psi_{x,y} \\ u_z &= \phi_{,z} - \Psi_{x,y} + \Psi_{y,x} \end{aligned} \tag{14}$$

3. Solution of Wave Equations using Integral Transform Method

To solve the equations of motions (8) and (9) the *Integral Transform Method* (ITM) together with the *Fourier Transform* will be used. The procedure is schematically described in f gure 1.

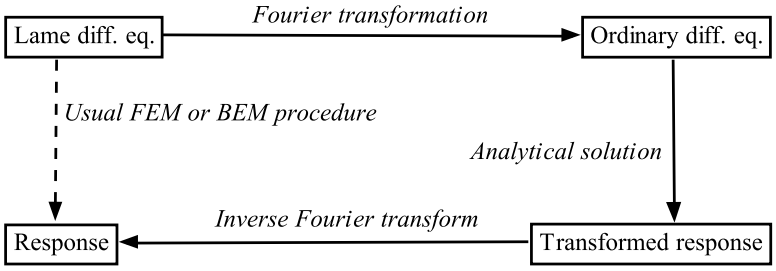

Figure 1. ITM procedure scheme

The *Fourier Transform* $\hat{f}(\omega)$ of a function $f(t)$ and *Inverse Fourier Transform* are def ned by the integrals:

$$\hat{f}(\omega) = \int_{-\infty}^{+\infty} f(t) e^{-i\omega t} dt \quad \circ\!-\!\bullet \quad f(t) = \frac{1}{2\pi} \int_{-\infty}^{+\infty} \hat{f}(\omega) e^{i\omega t} d\omega \tag{15}$$

where $\circ\!-\!\bullet$ sign represents the *Fourier Transformation*.
In case of a function with several independent variables, multiple integrals are used, concerning the transformation of each variable

$$\begin{gathered} \hat{f}(k_x,k_y) = \int_{-\infty}^{+\infty}\int_{-\infty}^{+\infty} f(x) e^{-i(k_x x + k_y y)} dx dy \\ \circ \\ | \\ \bullet \\ f(x,y) = \frac{1}{2\pi}\int_{-\infty}^{+\infty}\int_{-\infty}^{+\infty} \hat{f}(k_x,k_y) e^{i(k_x x + k_y y)} dk_x dk_y \end{gathered} \tag{16}$$

By a threefold *Fourier Transform* with regard to $x \circ\!-\!\bullet k_x$, $y \circ\!-\!\bullet k_y$ and $t \circ\!-\!\bullet \omega$, equations (8) and (9) can be transformed into the ordinary differential equations regarding the z-direction in wave number domain

$$\left(\frac{\omega^2}{c_p^2} - k_x^2 - k_y^2\right)\hat{\phi} + \frac{\partial^2 \hat{\phi}}{\partial z^2} = 0 \tag{17}$$

$$\left(\frac{\omega^2}{c_s^2} - k_x^2 - k_y^2\right)\hat{\Psi}_i + \frac{\partial^2 \hat{\Psi}_i}{\partial z^2} = 0 \quad , \quad i = x,y \tag{18}$$

The solution of the equations (17) and (18) is

$$\hat{\phi} = A_1 e^{\lambda_1 z} + A_2 e^{-\lambda_1 z} \tag{19}$$

$$\hat{\Psi}_i = B_{1i} e^{\lambda_2 z} + B_{2i} e^{-\lambda_2 z} \quad , \quad i = x,y \tag{20}$$

where A_1, A_2, B_{1i} and B_{2i} are the constants of integration, which can be obtained from boundary conditions, while λ_1 and λ_2 are equal to

$$\lambda_1^2 = k_x^2 + k_y^2 - k_p^2, \qquad \lambda_2^2 = k_x^2 + k_y^2 - k_s^2 \tag{21}$$

In equations (21) k_p and k_s are wave numbers for *P*- and *S-waves*

$$k_p = \frac{\omega}{c_p}, \qquad k_s = \frac{\omega}{c_s} \tag{22}$$

This solution allows to derivative macro-element relations for each layer between the stress and displacement at the top and bottom boundary of the layer in transformed domain. In transformed domain the equation (14) can be written as

$$\begin{aligned} \hat{u_x} &= ik_x\hat{\phi} - \hat{\Psi}_{y,z} \\ \hat{u_y} &= ik_y\hat{\phi} - \hat{\Psi}_{x,z} \\ \hat{u_y} &= \hat{\phi}_{,z} - ik_y\hat{\Psi}_x + ik_x\hat{\Psi}_y \end{aligned} \tag{23}$$

Substituting equations (20) and (19) into equation (23) the displacement vector in transformed domain is obtained in the form

$$\begin{bmatrix} \hat{u_x} \\ \hat{u_y} \\ \hat{u_z} \end{bmatrix} = \begin{bmatrix} ik_x & ik_y & 0 & 0 & -\lambda_2 & \lambda_2 \\ ik_y & ik_x & \lambda_2 & -\lambda_2 & 0 & 0 \\ \lambda_1 & -\lambda_1 & -ik_y & -ik_y & ik_x & ik_x \end{bmatrix} \cdot \{C\} \tag{24}$$

where

$$\{C\}^T = \begin{bmatrix} A_1e^{z\lambda_1} & A_2e^{-z\lambda_1} & B_{1x}e^{z\lambda_2} & B_{2x}e^{-z\lambda_2} & B_{1y}e^{z\lambda_2} & B_{2y}e^{-z\lambda_2} \end{bmatrix} \tag{25}$$

The stress vector in transformed domain can be obtained from the strain-displacement relations and *Hooke*'s law [9] as

$$\begin{bmatrix} \hat{\sigma}_x \\ \hat{\sigma}_y \\ \hat{\sigma}_z \\ \hat{\tau}_{xy} \\ \hat{\tau}_{yz} \\ \hat{\tau}_{zx} \end{bmatrix} = \mu \begin{bmatrix} -2kx^2 - \frac{\lambda_1}{\mu}k_p^2 & -2kx^2 - \frac{\lambda_1}{\mu}k_p^2 & 0 & 0 & -2ik_x\lambda_2 & 2ik_x\lambda_2 \\ -2ky^2 - \frac{\lambda_1}{\mu}k_p^2 & -2ky^2 - \frac{\lambda_1}{\mu}k_p^2 & 2ik_y\lambda_2 & -2ik_x\lambda_2 & 0 & 0 \\ 2k_r - k_s^2 & 2k_r - k_s^2 & -2ik_y\lambda_2 & 2ik_y\lambda_2 & 2ik_x\lambda_2 & -2ik_x\lambda_2 \\ -2k_xk_y & -2k_xk_y & ik_x\lambda_2 & -ik_x\lambda_2 & -ik_y\lambda_2 & ik_y\lambda_2 \\ 2ik_y\lambda_1 & -2ik_y\lambda_1 & \lambda_2^2 + k_y^2 & \lambda_2^2 + k_y^2 & -k_xk_y & -k_xk_y \\ 2ik_x\lambda_1 & -2ik_x\lambda_1 & k_xk_y & k_xk_y & -(\lambda_2^2 + k_x^2) & -(\lambda_2^2 + k_x^2) \end{bmatrix} \tag{26}$$

In the case of a layered half-space, it is better to use a new constants $\bar{A_1}$, $\bar{B_{1i}}$ instead of A_1, B_{1i} according to

$$\begin{aligned} A_1e^{\lambda_1 z} &= A_1e^{\lambda_1 h}e^{-\lambda_1 h}e^{\lambda_1 z} = \bar{A_1}e^{\lambda_1(z-h)} \\ B_{1i}e^{\lambda_2 z} &= B_{1i}e^{\lambda_2 h}e^{-\lambda_2 h}e^{\lambda_2 z} = \bar{B_{1i}}e^{\lambda_2(z-h)} \end{aligned} \tag{27}$$

where h is depth of the layer and $h > z$. The displacement vector, for each layer, in the transformed domain can be now written as

$$\begin{bmatrix} \hat{u_x} \\ \hat{u_y} \\ \hat{u_z} \end{bmatrix} = \begin{bmatrix} ik_x & ik_y & 0 & 0 & -\lambda_2 & \lambda_2 \\ ik_y & ik_x & \lambda_2 & -\lambda_2 & 0 & 0 \\ \lambda_1 & -\lambda_1 & -ik_y & -ik_y & ik_x & ik_x \end{bmatrix} \cdot \{\bar{C}\} \tag{28}$$

were $\{\bar{C}\}^T$ is

$$\{\bar{C}\}^T = \begin{bmatrix} A_1e^{(z-h)\lambda_1} & A_2e^{-z\lambda_1} & B_{1x}e^{(z-h)\lambda_2} & B_{2x}e^{-z\lambda_2} & B_{1y}e^{(z-h)\lambda_2} & B_{2y}e^{-z\lambda_2} \end{bmatrix} \tag{29}$$

The unknown integration constants can be obtained from the boundary conditions at the interface between the layers. At the upper surface of the top element the boundary conditions of the half space must be fulfilled, as well as the Sommerfeld's radiation condition if the bottom element goes to infinity.

4. Half-Space Displacements Due to Harmonic Unit Force

In order to get the impedance functions of the rectangular foundations lying on the half-space, the displacements of the half-space due to unit harmonic forces acting in vertical direction z, and both horizontal directions, x and y (Figure 2) have to be calculated.

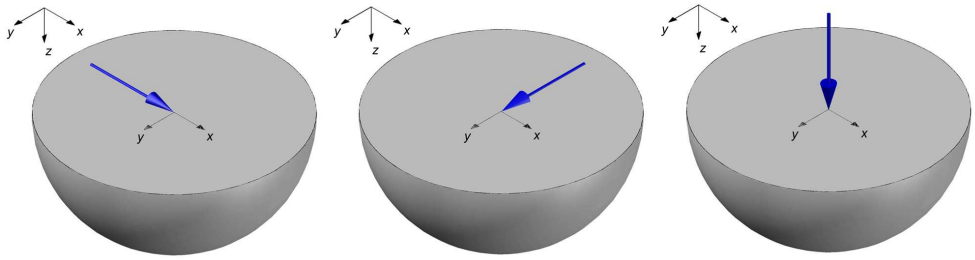

Figure 2. Harmonic force acting on the surface of the half-space

On the f gures below, the displacements at the surface of the half-space due to the vertical and horizontal force of unit amplitude, at frequency $\omega = 50\ Hz$ are displayed.

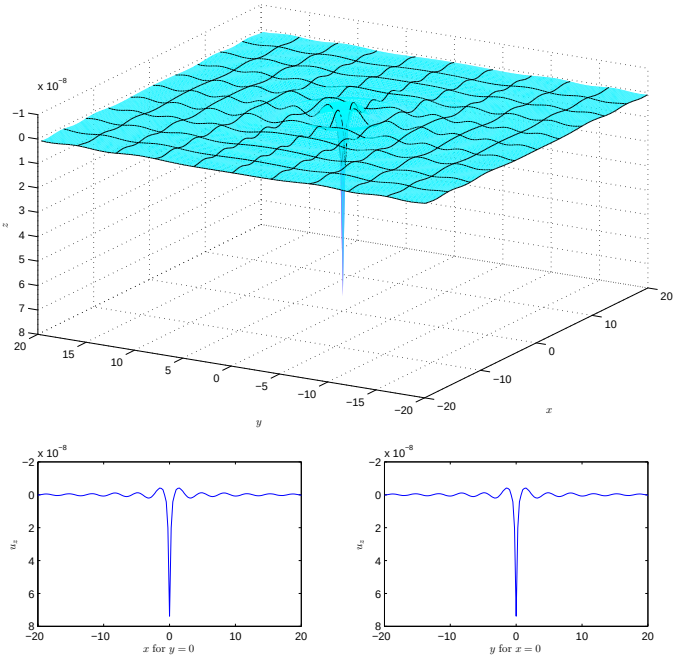

Figure 3. Vertical displacements $u_z\ (m)$, $P_z = 1\ (kN)$, $\omega = 160\ rad/s$, $\nu = 0.4$

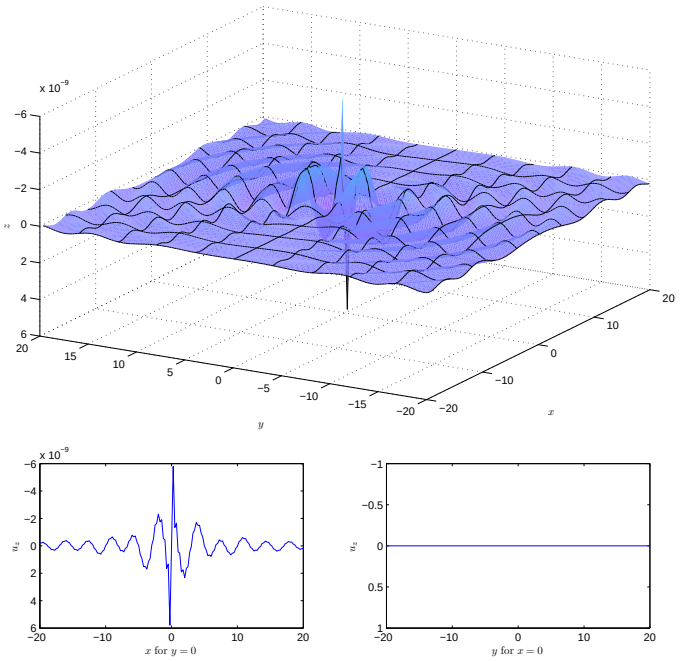

Figure 4. Horizontal displacements u_x (m), $P_z = 1$ (kN), $\omega = 160$ rad/s, $\nu = 0.4$

5. Impedance Functions

5.1. Dynamic stiffness matrix of flexible rectangular foundation

The dynamic stiffness matrix of the f exible rectangular foundation, $\mathbf{K}_f$, is obtained by inverting the dynamic f exibility matrix, $\mathbf{K}_f = \mathbf{F}_f^{-1}$. Elements of dynamic f exibility matrix $\mathbf{F}_f$ represent the nodal displacements at the surface of the half-space due to corresponding harmonic forces of a unit amplitude. They are obtained using ITM. If $n \times n$ is a number of nodes of a rectangular surface on half-space, the dimension of the f exibility matrix is $3n \times 3n$. Nodal displacements vector $u_f(3n,1)$ and corresponding force vector $P_f(3n,1)$ are related by dynamic stiffness matrix of f exible foundation $\mathbf{K}_f(3n,3n)$

$$\mathbf{P}_f = \mathbf{K}_f \mathbf{u}_f \tag{30}$$

5.2. Dynamic stiffness matrix of rigid rectangular foundation

Dynamic stiffness matrix of the corresponding rigid, massless, rectangular foundation is obtained from dynamic stiffness matrix of f exible foundation using kinematic transformation. Rigid foundation has 6 degrees of freedom: three translator vibrations, in x, y and z directions, and three rotational vibrations, around x, y and z axes. The vector of

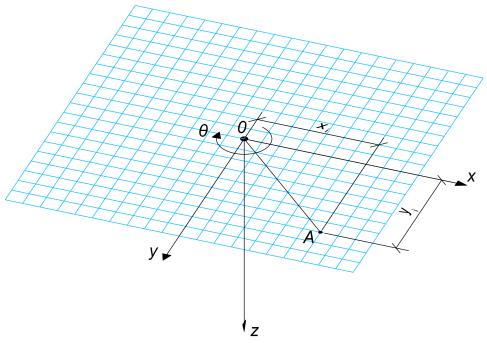

Figure 5. Interaction surface between rigid foundation and soil

displacements $\mathbf{u}_r$ in the centroid O of the interaction surface and corresponding force vector $\mathbf{P}_r$ are, respectively

$$\mathbf{u}_r = \begin{bmatrix} u_x \\ u_y \\ u_z \\ \varphi_x \\ \varphi_y \\ \varphi_z \end{bmatrix} \qquad \mathbf{P}_r = \begin{bmatrix} P_x \\ P_y \\ P_z \\ M_x \\ M_y \\ M_z \end{bmatrix} \tag{31}$$

Vectors $\mathbf{u}_r$ and $\mathbf{P}_r$ are related by

$$\mathbf{P}_r = \mathbf{K}_r \mathbf{u}_r \tag{32}$$

where $\mathbf{K}_r(6,6)$ is dynamic stiffness matrix of rigid foundation.
Vector of nodal displacements $\mathbf{u}_f$ and vector $\mathbf{u}_r$ are relate with kinematic constraint equation

$$\mathbf{u}_f = \mathbf{a}\mathbf{u}_r \tag{33}$$

where $\mathbf{a}(3(n \times n), 6)$ is kinematic matrix

$$\mathbf{a} = \begin{bmatrix} \mathbf{a}_1 \\ \mathbf{a}_2 \\ \vdots \\ \mathbf{a}_i \\ \vdots \\ \mathbf{a}_{n \times n} \end{bmatrix} \tag{34}$$

This matrix consists of $n \times n$ sub-matrices $\mathbf{a}_i$, $i = 1, 2, \cdots n \times n$. Each sub-matrix $\mathbf{a}_i$ is obtained from kinematic consideration, regarding node $A = i$ and centroid of foundation O (Figure 5), as

$$\mathbf{a}_i = \begin{bmatrix} 1 & 0 & 0 & 0 & 0 & -y_i \\ 0 & 1 & 0 & 0 & 0 & x_i \\ 0 & 0 & 1 & y_i & -x_i & 0 \end{bmatrix} \tag{35}$$

Quantities x_i and y_i are horizontal distances in x and y direction, respectively, between the centroid of the surface foundation O and node $A = i$, Figure 5.
Equaling the energy of the deformation, expressed in term of both pairs of variables,

$$E = \mathbf{P}_f^T \mathbf{u}_f = \mathbf{P}_r^T \mathbf{u}_r \tag{36}$$

and taking into account Eqs. (30), (32) and (33), obtained is the relation between the dynamic stiffness matrix of rigid and f exible foundation in the form

$$\mathbf{K}_r = \mathbf{a}^T \mathbf{K}_f \mathbf{a} \tag{37}$$

At least, the dynamic stiffness matrix of rigid rectangular foundation is obtained as

$$\mathbf{K}_r = \begin{bmatrix} K_{xx} & 0 & 0 & 0 & K_{x,my} & 0 \\ 0 & K_{yy} & 0 & K_{y,mx} & 0 & 0 \\ 0 & 0 & K_{zz} & 0 & 0 & 0 \\ 0 & K_{mx,y} & 0 & K_{mx} & 0 & 0 \\ K_{my,x} & 0 & 0 & 0 & K_{my} & 0 \\ 0 & 0 & 0 & 0 & 0 & K_{mz} \end{bmatrix} \tag{38}$$

The dynamic stiffness matrix $\mathbf{K}_r$ is frequency dependent, complex matrix, which can be written as a sum of real and imaginary part

$$\mathbf{K}_r(a_0) = R_e(\mathbf{K}_r(a_0)) + i \cdot I_m(\mathbf{K}_r(a_0)) \tag{39}$$

The impedance functions are functions representing the dimensionless real and imaginary part of dynamic stiffness matrix $\mathbf{K}_r$. Real part represents the dynamic stiffness, while imaginary part represents damping of foundation in one direction. These functions are usually written as functions of dimensionless frequency $a_0 = \omega B/c_s$, where B is the foundation half-width. To obtain impedances the dynamic stiffnesses are reduced by the appropriate coeff cients of reduction. For vertical and horizontal stiffness the reduction coeff cient is equal to GB, while for rocking and torsional stiffness it is equal to GB^3, where G is shear modulus of the soil.

6. Numerical Example

In the following example the impedance functions of the rigid massless square foundation lying on the half-space is calculated using ITM. The dimensions of square foundation are $5m \times 5m$. The foundation is divided into the mesh, with unit 0.25 meters in both directions. The half-space characteristics are

- Elastic modulus: $E = 5 \cdot 10^7(1 + 2iD) \quad kN/m^2$
- Damping ratio: $D = 0.02$
- Poisson coeff cient: $\nu = 0.4$
- Density: $\rho = 2000 \quad kg/m^3$

The process of obtaining impedance functions is divided into several parts.
First, the displacements at the surface of the half-space (in x, y and z directions) for single unit force in x, y and z direction were calculated for every chosen angular frequency ω, using ITM. The discretization mesh should be wide and dense enough to avoid troubles with singularities and aliasing [8]. The obtained displacement f elds are shown at Figures 3 and 4.

The next step is calculation of flexibility matrix of the flexible foundation, F_f. The displacement fields is calculated for one node of the mesh and than shifted accordingly to the global coordinate system, in order to fill the flexibility matrix F_f. Figure 6 shows the example of shifting data for filling the columns and rows of the flexibility matrix F_f that correspond to the vertical displacements due to vertical harmonic unit force. Assume that displacement field is calculated for the acting force node which has index (i, j), Figure 6.a. The displacement field due to the force acting in node (m, n), Figure 6.b, can be obtained for every pair of index increments k and l from the relation

$$u_z(i+k, j+l) = u_z(m+k, n+l) \tag{40}$$

The stiffness matrix of the flexible foundation K_f is obtained by inverting the flexibility matrix, $K_f = F_f^{-1}$.

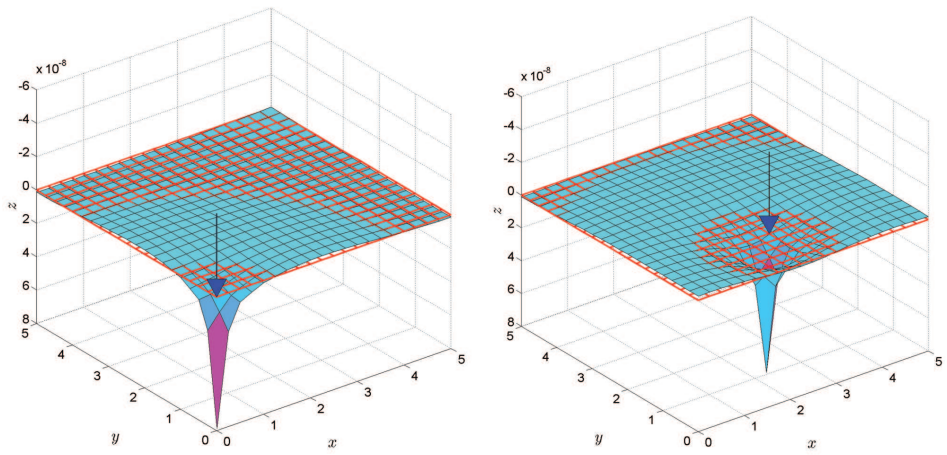

(a) (b)

Figure 6. Calculation of the flexibility matrix. Shifting the displacements field data.

Finally, the stiffness matrix of the rigid foundation K_r is obtained from the stiffness matrix of the flexible foundation K_f using kinematic transformation defined in Eq. (37). Once K_r is calculated for every chosen ω the impedance functions can be obtained, as described at the end of the section 5.

Figures 7, 8, 9, 10 represent impedance functions. Since the foundation is square, $K_{yy} = K_{xx}$ and $K_{my} = K_{mx}$. Dashed line refers to the results obtained in the numerical example described in this section; solid line refers to the results obtained by *Schmid* [5] using *BEM*. Impedance functions obtained using ITM have the same shape but higher values than functions obtained using *BEM*.

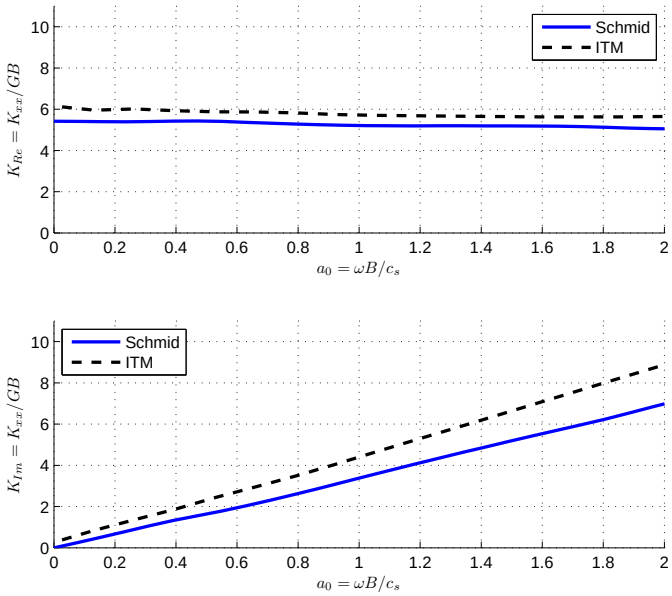

Figure 7. Horizontal dynamic stiffness K_{xx}, $\nu = 0.4$

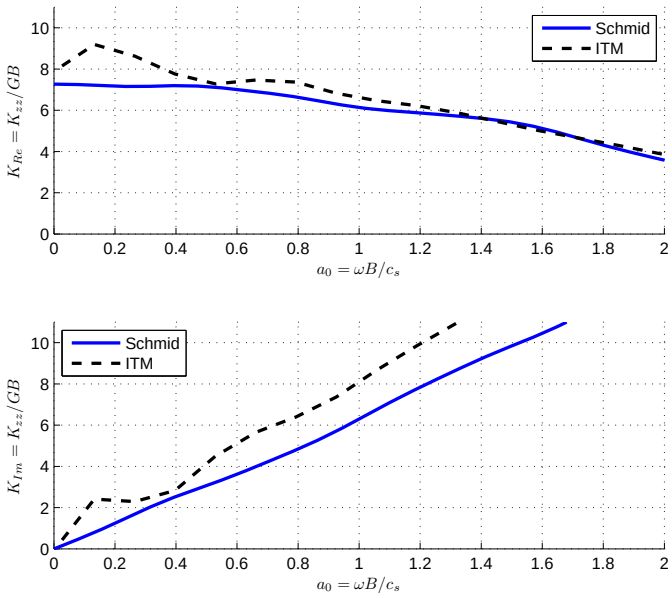

Figure 8. Vertical dynamic stiffness K_{zz}, $\nu = 0.4$

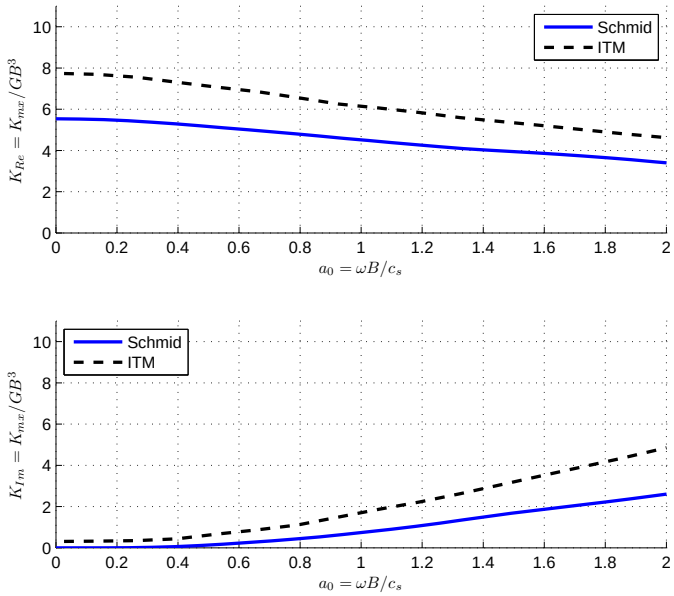

Figure 9. Rotational dynamic stiffness K_{mx}, $\nu = 0.4$

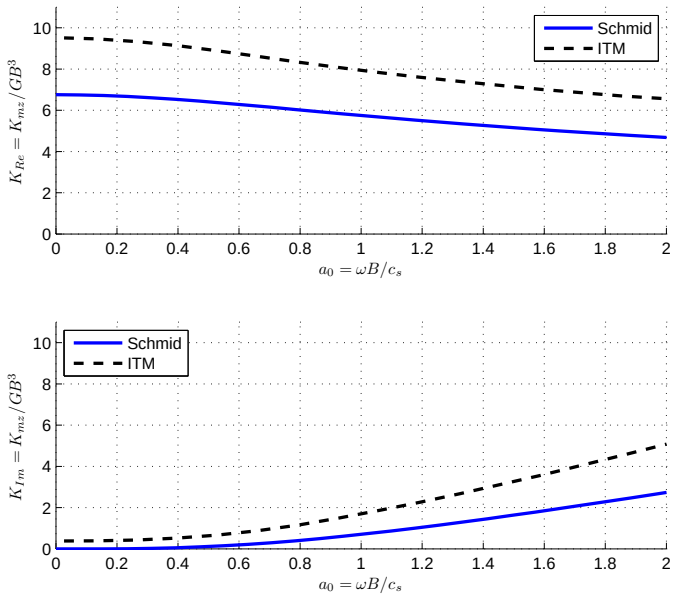

Figure 10. Torzional dynamic stiffness K_{mz}, $\nu = 0.4$

7. Conclusion

The *ITM* is used to calculate impedance functions for rectangular rigid foundation on a half-space. The obtained results show good agreement with results from literature. *Integral Transform Method* is based on the analytic solution of the wave propagation theory and transformed technique. The original problem is transfered to a new domain using *Fast Fourier Transform (FFT)*, where it can be solved much easily. The obtained results are returned into the original domain by *Inverse Fast Fourier Transform (IFFT)*. These transformations may demand a considerable computational effort.

ITM is restricted to the half-space and to a horizontally layered half-space, with a homogeneous and isotropic layers. In order to overcome this limitation for the case of local irregularities *ITM*-approach can be combined with *FEM*. Instead of *FFT*, Laplace transformation or *Wavelet transform* can be used.

The advantage of *ITM* is that damping is taken into account automatically, as material, or hysteretic damping as well radiation damping. The material damping is involved through complex modulus, while radiation damping is def ned by *Sommerfeld*'s radiation condition. This approach can be used for solving different problems of wave propagation in the soil, specially problems of rail or road traff c induced vibrations.

References

[1] Dominguez J (1993) *Boundary Elements in Dynamics*, Computational Mechanics Publications, Boston.

[2] Grundmann H, Trommer E (2001) *Transform methods–what can they contribute to (computational) dynamics?*, Computers and Structures, 79, 2001, p.2091-2102

[3] Kausel E (1994) *Thin-Layer Method* International Journal for Numerical Methods in Engineering, 37, 1994, p. 927-941.

[4] Müller G, *Integral Transform Method*, lecture materials, *Summer school: Traffic induced vibration*, 3-11 October 2009 and 4-11 October 2010, Faculty of Civil Engineering University of Belgrade, Belgrade.

[5] Schmid G, Tosecky A (2003) *Soil-Structure Interaction Foundations Vibrations*, Lecture for the Master Course *Earthquake Engineering* at IZIIS University *SS. Cyril and Methodius* Skopje, Ruhr University Bochum, Department of Civil Engineering

[6] Petronijević M, Schmid G (2008), *Metode linearne dinamicke analize sistema tlo-objekat*, Izgradnja, 62, 2008, p. 541-554 (UDK: 699.841.001.575=861)

[7] Radišić M, Nefovska-Danilović M, Petronijević M (2010): Dinamička krutost pravougaonog temelja, *Zbornik radova 13. kongresa DGKS*, Zlatibor-Čigota, 22-24.09.2010. s. 473-478, (ISBN 978-86-85073-09-0)

[8] Radišić M (2010), *Primjena Metoda integralne transformacije (ITM) za odredjivanje pomjeranja i napona u tlu usled harmonijskog opterećenja*, diplomski–master rad, Gradjevinski fakultet Univerziteta u Beogradu, 2010.

[9] Rastandi J I (2003) *Modelization of Dynamic Soil-Structure Interaction Using Integral Transform-Finite Element Coupling*, Lehrstuhl für Baumechanik der Technischen Universität München

Acknowledgment

We are grateful that this research is f nancially supported through the project TR 36046 by the Ministry of Science and Technology, Republic of Serbia.

CONSTITUTIVE RELATIONS FOR HARDENING AND SOFTENING OF BRITTLE 2D LATTICES

A. Rinaldi[1*], S. Mastilovic[2,]**

[1] Department of Chemical Science and Technology, University of Rome "Tor Vergata"
Via della Ricerca Scientifica, 00133 Roma, Italy
e-mail: Antonio.Rinaldi@uniroma2.it
[2] Faculty of Construction Management, Union University
Cara Dusana 62-64, 11000 Belgrade, Serbia
* Corresponding author. e-mail: antonio.rinaldi@enea.it
** Corresponding author. e-mail: smastilovic@fgm.edu.rs

Abstract. The objective of this study is to highlight the universal behavior of the damage parameters and infer constitutive relations of the disordered brittle systems. The statistical damage model used, although admittedly simple, captures what we believe to be the key features of the problem at hand and facilitates formulation of an analytical constitutive relation for the hardening and softening phases of two-dimensional (2D) lattices. A definition of damage parameter for the softening is proposed. The results confirm that the analytical model can be used to investigate the softening phase and failure. As an alternative approach, a semi-empirical model based on Extreme Value Theory is offered. A base for Damage Tolerance Principles technology standards of commercial airplane industry is discussed.

1. Introduction

The objective of the present study is a brittle material with mesotexture characterized by initially random statistically homogeneous distribution of microcracks, which, in the course of loading, becomes heterogeneous due to propagation and clustering of microcracks prior to failure. This homogeneous-to-heterogeneous phase transition was analyzed by Krajcinovic and Rinaldi [1] using the statistical mechanics and fractal geometry, while the gist of the constitutive modeling presented herein is based on Rinaldi et al. [3]. The structure size and the material's mesoscale structural transformations influence the failure threshold. The limit states design is driven primarily by crack growth but also by the microstructural re-arrangements in the heterogeneous phase. The foundation of the structural design and maintenance principles in Boeing Commercial Airplane Group, U.S.A., is the "*Damage Tolerance Principles*" [2], which is focused on two structural design objectives:

(1) *Damage Tolerance*: Ability of structure to sustain anticipated loads in the presence of fatigue, corrosion or accidental damage until such damage is detected through inspections or malfunctions and repaired;
(2) *Durability*: Ability of the structure to sustain degradation from such sources as fatigue, accidental damage and environmental deterioration to the extent that they can be controlled by economically acceptable maintenance and inspection

programs.

Damage tolerance is comprised of three elements of importance for achieving the desired level of safety:

- The determination of the residual strength or the maximum allowable damage that the structure can sustain under regulatory fail-safe load conditions.
- The crack growth defined as the interval of damage progression from lengths with negligible probability of failure to an allowable size determined by the residual strength.
- The inspection program based on damage detection strategy such that the methods, sequence, and intervals of inspections ensure timely damage detection.

The typical experimental data from both full-scale crack growth testing (600 tests on two different wing panels of width 200 mm and 2300 mm) is presented in Fig. 1 (adopted from [2]). The crack length is normalized to the LEFM (Linear Elastic Fracture Mechanics) limit L_Y representing boundary between LEFM and transition behavior, and the corresponding strength is normalized to the maximum strength of the pristine undamaged panel.

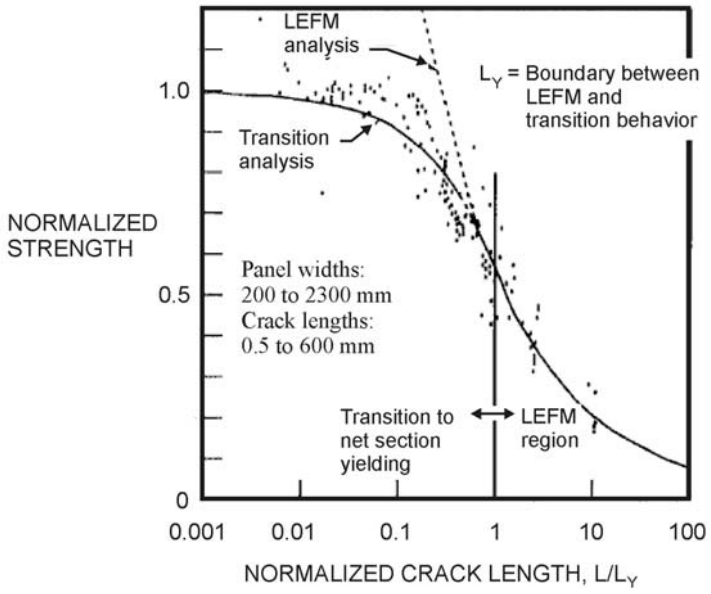

Figure 1. Experimental data of wing panels crack growth adopted from Goranson [2].

The minimum normalized strength, which corresponds to the maximum allowable damage, and the corresponding maximum crack length are assigned on Fig. 1 in compliance with the "fail-safe' strategy. Nevertheless, the determination of the tolerable damage level is based largely upon experience and POD (Probability of Detection) from visual inspection [3]. It is obvious that it is practically impossible to conduct expensive full-scale fatigue tests for every structural component to obtain the data such presented in Fig. 1. Unfortunately, LEFM is not always applied to the multiple-site cracking and diffuse damage [3], which is currently still managed in a purely empirical fashion. Consequently, there is an urging need

for a "reliable multiple scale analytical models that account for the structural size effect and which can be used for data extrapolation" [3].

2. Simulation model

The present study was focused on the universal trends rather than particularities of the physical problem at hand. Consequently, the simulation model and the analytical approach used, although admittedly simple, captured what we believe to be the underlying features of the phenomena. The computational approach taken was following footsteps of the classic papers on the central-force lattices modeling the brittle fracture of disordered materials [e.g., 13, 15, 17] and was built upon the more recent extensive work of the present authors and coworkers [e.g., 1, 3, 4, 6, 16, 18, 20]. The comprehensive summary of lattice models in micromechanics is available in [19].

We were studying a simple disordered discrete system that, from our experience, captured reasonably well the universal behavior of the damage parameters and constitutive relations of the quasi-brittle materials. Although the procedures for constructing a mechanically equivalent lattice capable of matching the physical properties of polycrystalline ceramics were available [18], no attempt was made to calibrate the major statistics of the given microstructure in the presently used model since it did not aim at describing a specific material but rather a class of brittle materials whose primary microstructural response was failure of an inferior-strength interface. Examples of the materials of this kind are many and well documented [e.g., 3, 4, 6, 16, 21]. Their microscale texture in two-dimensional space is similar to a random Voronoi froth with the dual Delaunay lattice [1, 3, 11]. A Voronoi polygon represented a defining constituent at the dominant spatial scale (a grain of ceramic, a concrete aggregate or a granule of clastic rock) whereas a bond in the Delaunay lattices was representative of interface cohesion. Damage evolution, reflecting accumulation of degradation micro-events and cooperative phenomena, is a stochastic process dependent on the various aspects of microstructural disorder. Consequently, the lattice was geometrically disordered since the initial link lengths (in the pristine condition) were normally distributed within the range $\alpha_L\ \bar{\lambda} \le \lambda \le (2-\alpha_L)\bar{\lambda}$ ($\alpha_L = 1$ would imply that all grains were perfect hexagons). The lattice topological disorder was defined in terms of the number of the nearest neighbors. The load-induced damage is introduced in the network by rupturing of the links, which represents intergranular microcrack nucleation. The links are nonlinear in compression and linear in tension (resulting from a combination of Born-Meyer's and Hooke's potentials, [6]), with random tensile strength and identical link stiffness k [3]. If the critical tensile strain ε_{cr} was reached, permanent rupture occurred and the link was reduced into a common contact element.[1] The values ε_{cr} were randomly sampled from a uniform distribution starting at zero (the limit case that captured preexisting microcracks, for example, from fabrication). It is obvious that such lattice model is inherently limited to intergranular microcracks, which is reasonable approximation for many ceramics [5, 7]. Since the resolution length of the model is equal to the grain facet, the rupture, i.e. the growth of a microcrack from the initial length to the length of the grain boundary facet, is necessarily instantaneous.

[1] The tensile stiffness becomes zero and the link cannot longer carry tensile forces. The broken link remains active in compression if load reversal occurs in the course of deformation to account for the crack closure.

The quasi-static uniaxial tensile tests were simulated under the displacement-controlled conditions on different lattice sizes. The molecular dynamics solver based upon the Verlet's algorithm [6, 21] was adopted. Each simulation was carried on incrementally, up to the threshold of failure, by applying small displacement steps and by computing the equilibrium configuration at each step [3, 21]. The damage evolution was tracked during the "virtual tensile experiment" [21] by recording the number of broken bonds, n. The macroscopic data scatter of the $\overline{F}$ *vs.* $\overline{u}$ and n *vs.* $\overline{u}$ curves (within-size variability) indicates that $\overline{D}(\overline{\varepsilon}, L)$ is a random variable at any given $\overline{\varepsilon}$ in the softening phase (Fig. 2).[2]

The average $\overline{F}$ *vs.* $\overline{u}$ and n *vs.* $\overline{u}$ curves from the 10 replicates per size $N = \{24, 48, 96, 192\}$ were considered for the scaling in [1], with N being the number of grains per lattice side. The original dataset is expanded in [3] to enhance the accuracy, robustness and precision of the regression analysis. Intermediate lattice sizes $N = \{72, 120\}$ were added and more than 10 runs were collected for smaller lattices. The maximum lattice size was also enlarged. Five extra simulations for $N = 288$ were analyzed but, for the sake of computational economy, limited to the hardening phase.

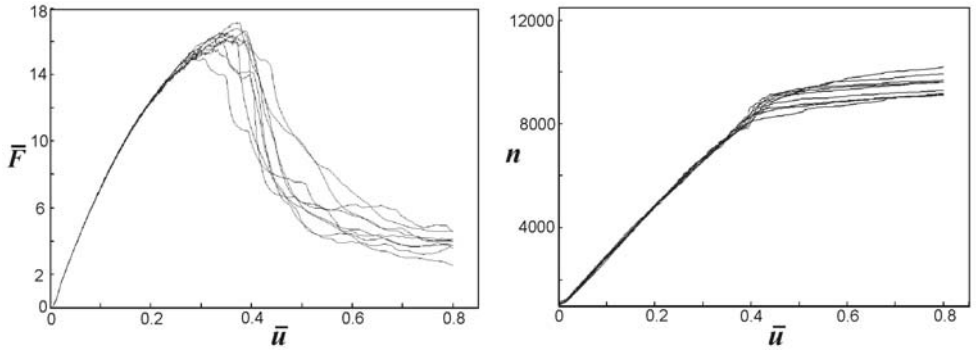

Figure 2. Evolution of state parameters in the course of the quasi-static uniaxial loading for ten N=192 replicas.

An example of the macrocrack emanating from damage localization is displayed in Fig.3. (The strain localization as a dynamic transition in the correlation length range was analyzed by a similar lattice model by Krajcinovic and Vujosevic [20].) Only the evolution of such macrocrack can provide the "Crack Growth" defined as "the interval of damage progression from length below which there is negligible POD to an allowable size determined by residual strength requirements" [2].

[2] The bar above the symbol indicates a macroscopic quantity.

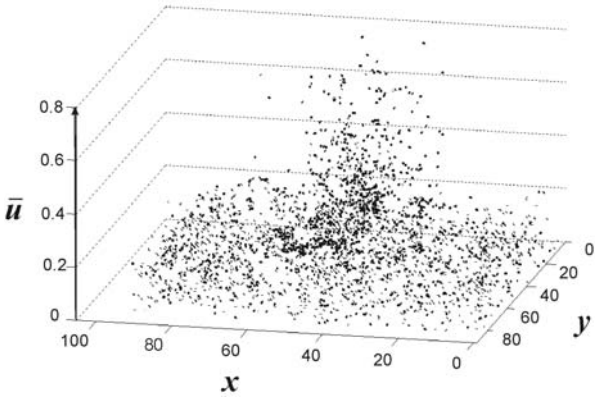

Figure 3. Damage localization. Short lines represent the broken links.

3. Damage mechanics modeling

The limits of traditional continuum models of damage are discussed in literature [*e.g.,* 4, 12]. Models based upon Eshelby's solution [8], representative volume element [9, 10] and fabric tensor [12], are suitable only as long as the microstructure is statistically homogenous. Materials are homogeneous when microcracks nucleate in absence of cooperative phenomena (and the expectation value of damage parameter $\bar{D}$ is equal to the volume average $\langle D \rangle$ of individual micro-cracks), and heterogeneous when clusters of microcracks form. The threshold of fracture is reached when the dominant cluster reaches a correlation length equal to the lattice (specimen) size.

The lattice simulation data indicated that the scaling techniques apply to damage mechanics [1]. This statistical model of the disordered microstructure provided analytical expressions of damage parameter.

The stress-strain relation for the damage-degraded material had the familiar form

$$\bar{\sigma}\left(\bar{\varepsilon}, L\right) = \bar{E}^{o}\left[1 - \bar{D}\left(\bar{\varepsilon}, L\right)\right]\bar{\varepsilon} \tag{1}$$

During the hardening phase ($\partial\bar{\sigma}/\partial\bar{\varepsilon} > 0$), a simple analytical formula for the damage parameter

$$\bar{D}\left(\bar{\varepsilon}, L\right) = a\bar{\varepsilon} + b\frac{\bar{\varepsilon}^{2}}{L^{\alpha}} \tag{2}$$

was obtained from the scaled data by Krajcinovic and Rinaldi [1]. (The values $\{\alpha, a, b\} = \{-0.035, 275, -14862\}$ were deduced by the data fitting.) On the other hand, the analytical model for the damage parameter during the softening phase ($\partial\bar{\sigma}/\partial\bar{\varepsilon} < 0$) had a more complex form

$$\bar{D} = L^{\alpha}\bar{D}_p + a_1 L^{\alpha}\bar{\varepsilon}_s + b_1 L^{\alpha} L^{z} \left(1 - \exp\left(-\frac{c_1 \bar{\varepsilon}_s}{L^{z}}\right)\right) \tag{3}$$

where $\bar{\varepsilon}_s = \left(\bar{\varepsilon} - \bar{\varepsilon}_{peak}\right) / L^{\alpha}$, $\bar{D}_p = 0.5$ and $\{a_1, b_1, c_1, z\} = \{15.80, 2.2, 100, -0.52\}$ [1].

3.1 Constitutive relations and damage parameter

The purpose of the present inquiry, published originally in [3], was the deduction of the analytical constitutive relation [1] from the correct application of the scaling relations (2) and (3). The damage parameter in the hardening phase was defined in [1] as

$$\bar{D} = n\left(\bar{\varepsilon}\right) / \mu L^2 \tag{4}$$

where $n\left(\bar{\varepsilon}\right)$ was the number of broken bonds and μ was a fitting parameter deduced from simulations.

3.2 Hardening

The proposed damage parameter (4) was inspired by three observations. First, the strict similarity between the "parallel bar system" (PBS) and the lattice during damage nucleation [4,12] suggested

$$\bar{D} = \frac{n}{2N_p} \tag{5}$$

where N_p was the number of broken links corresponding to the peak of the stress-strain curve (1).

Second, the *log-log* plot of the average N_p *vs.* L in Fig.3b from simulations demonstrated that N_p for the lattice was a fractal following the power law

$$N_p\left(L\right) \cong n(\bar{\varepsilon}_p, L) = \left(e^{-1.3}\right) L^{1.94} \tag{6}$$

The fractal exponent was 1.94 with 95% confidence interval $\left[1.92,\ 1.96\right]$. From Eqs.(4-6) the value $\mu = 2\ e^{-1.3}$ was assumed, where -1.3 was obtained from Fig.4b as the intercept of the regression line. This value of the fitting parameter differs from $\mu = 2\ e^{-1.6}$ reported in [1], which could be associated with different datasets used for the statistical analysis. Similarly, the first estimate of the fractal exponent was 1.96 [1]. Since the "expanded" dataset was used later [3] for the regression, the corresponding estimates should be more reliable and, consequently, the mean square error and the confidence intervals on the regression coefficients (slope and intercept) were tighter. Nevertheless, most of our treatment referred to the first dataset only and, hence, we retained the old value $\mu = 2\ e^{-1.6}$ in order to legitimately use Eqs.(2) and (3).

Finally, $L^{1.94}$ was replaced by L^2 in Eq. (4) because n was a fat fractal with exponent 2 throughout the hardening phase, before the critical point $(\partial\bar{\sigma}/\partial\bar{\varepsilon}=0)$ was reached, as demonstrated by the n *vs.* L plot in Fig.4a. Furthermore, the n *vs.* $\bar{\varepsilon}$ curves of different lattice sizes collapsed into a single curve $\bar{D}$ *vs.* $\bar{\varepsilon}$ during damage nucleation only for the exponent 2 (Fig.4b in [1]), as previously noted by Hansen et al. [13]. The 95% confidence intervals (the dashed lines in Fig. 4) were very tight.

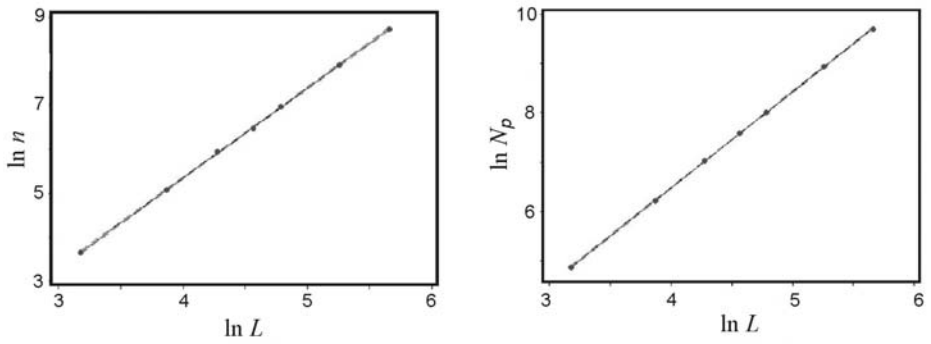

Figure 4. Fractal behavior of $n(\bar{\varepsilon},L)$ in the middle of hardening phase (exp. = 2) and at the peak (exp. = 1.94). (a) $\ln n=-2.85+2.05\cdot\ln L$; $R^2_{adj}=100\%$, $R^2=100\%$, $S=0.020$; (b) $\ln N_p=-1.29+1.94\cdot\ln L$; $R^2_{adj}=100\%$, $R^2=100\%$, $S=0.014$.

The coefficients of determination R^2 and R^2_{adj} reported by MINITAB 14© were rounded in [3] to 100% (Fig. 4), which proved the high significance and quality of the regression analysis (R^2 = 1 indicates perfect linear correlation [14,15]). The regression on the seven sizes $N=\{24, 48, 72, 96, 120, 192, 288\}$ provided a 2 decimal digits precision for the fractal exponents, which was satisfactory. The size range covered over one order of magnitude.

3.3 Softening

With $\bar{D}$ defined as in (4), the $\bar{D}-\bar{\varepsilon}$ curves were scaled in [1] to obtain Eqs. (2) and (3). While Eq.(2) was a suitable definition of damage parameter for the hardening phase, Eq.(3) was not a valid damage parameter for the softening phase. The lattice is a network of elastic springs and the corresponding secant stiffness $\bar{E}(L)=\bar{E}^o\left[1-\bar{D}(\bar{\varepsilon},L)\right]$ is positive-definitive [12]. Hence, the "proper damage parameter" [3] must always be $0\le\bar{D}\le1$ and should monotonically[3] approach $\bar{D}=1$ at failure ($\bar{E}_{failure}=0$). These two constraints were not accounted for in the softening data scaling in [1]. Therefore, while expression (2) was perfectly legitimate, definition (3) needs improvement.

[3] continuously or discontinuously, depending on whether the failure is first order or second order phase transition [3]

In the lattice model, the number of broken links $n(\bar{\varepsilon})$ was a measure of the total damage. The parameter $\bar{D}$ supplied just the normalization, like in Eq.(5), and possibly rendered this information scale-invariant. A fundamental premise in our framework [1, 3] was that hardening and softening phases were independent non-simultaneous processes. The microcracks nucleation was driven by a fat fractal with fractal exponent 2 for the most part and by a proper fractal with exponent 1.94 at the peak of stress-strain response. Such driving set changes at the transition, i.e. an appropriate denominator (normalization number) should replace μL^2 in (4). The following form of damage parameter was assumed in the softening phase

$$\bar{D}(\bar{\varepsilon}, L, n) = \frac{n(\bar{\varepsilon}_{peak}, L)}{\mu L^2} + \frac{\Delta n(\bar{\varepsilon}, L)}{X(L)} \tag{7}$$

where $\Delta n = n(\bar{\varepsilon}, L) - n(\bar{\varepsilon}_{peak}, L)$ was the number of broken bonds in the softening phase and $\bar{\varepsilon}_{peak}$ corresponds to the critical point ($\partial\bar{\sigma}/\partial\bar{\varepsilon} = 0$). The analytical expression for Δn follows from (1) and (4) as

$$\Delta n(\varepsilon, L) = \mu L^2 \left[\bar{D} - L^{\alpha} \bar{D}_p \right] = \mu L^2 \left[a_1 L^{\alpha} \bar{\varepsilon}_s + b_1 L^{\alpha} L^{z} \left(1 - \exp\left(-\frac{c_1 \bar{\varepsilon}_s}{L^{z}} \right) \right) \right] \tag{8}$$

which was essentially the information conveyed by Eq. (3). Eq.(8) was equivalent to magnifying the scaled data in the softening phase by a factor μL^2. Hence, the constitutive relations for the hardening and softening phases could be rewritten as

$$\bar{\sigma} = \bar{E}^o \left[1 - \frac{n(\bar{\varepsilon}, L)}{\mu L^2} \right] \bar{\varepsilon}, \quad (\partial\bar{\sigma}/\partial\bar{\varepsilon} > 0) \tag{9.a}$$

$$\bar{\sigma} = \bar{E}^o \left[\left(1 - \frac{N_p}{\mu L^2} \right) - \frac{\Delta n(\bar{\varepsilon}, L)}{X(L)} \right] \bar{\varepsilon}, \quad (\partial\bar{\sigma}/\partial\bar{\varepsilon} < 0) \tag{9.b}$$

Then, *X (L)* in the denominator of (7) and (9.b) needed definition. The 3D plot of microcracks location *vs.* simulation time in Fig.3 highlighted the contrast between the uniformly distributed damage nucleation and the highly correlated damage propagation localized along a narrow strip. From this viewpoint, a fractal exponent close to one was intuitively plausible for the invariant set driving the propagation, as much as the fat fractal suited the phenomenology of the nucleation.

A deductive reasoning based upon statistical methods was used to reach a data driven choice for *X (L)*. By assuming that (9.b) was the proper form of the model, one could write

$$\hat{\bar{\sigma}}_i(\bar{\varepsilon}_i, \Delta n_i, \beta) = \bar{E}^o \left[\left(1 - N_p / \mu L^2 \right) - \beta \Delta n_i \right] \bar{\varepsilon}_i \tag{10}$$

where $\beta(L) = 1/X(L)$, Q was the number of numerical observations used for the regression and $\hat{\bar{\sigma}}_i$ was the estimate of stress value at $\bar{\varepsilon}_i$ and Δn_i from the model for $i = 1, 2, \ldots, Q$. Since the model was linear in the unknown parameter β, the "ordinary least squares" method can be used to compute a minimum unbiased estimator $\hat{\beta}$ of β [14]. The mean square error function for this model (the sum of the squared deviations between the simulation data and the predicted value over Q) was minimized with respect to $\hat{\beta}$ in [3], which yield the estimate

$$\hat{X}(L) = \hat{\beta}^{-1}(L) = \frac{\sum_{i=1}^{Q} \bar{E}^o \bar{\varepsilon}_i^2 \Delta n_i^2}{\sum_{i=1}^{Q} \left(\left[\left(1 - N_p / \mu L^2\right) \bar{E}^o \bar{\varepsilon}_i - \bar{\sigma}_i \right] \Delta n_i \bar{\varepsilon}_i \right)} \tag{11}$$

The results of Eq.(11) are marked in Fig.5 by circles for the sizes $N = \{24, 48, 72, 96, 120, 192\}$. The linear fit through the six $\hat{X}(L)$ values matched the results very well, as indicated by a coefficient of determination close to unity $\left(R^2 = 0.9971;\ R^2_{adj} = 0.997\right)$.

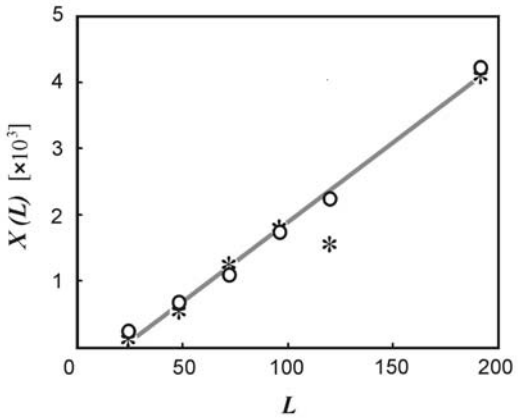

Figure 5. Comparison of $X(L)$ estimates from (11) for the 6 average Δn (circles) and for 6 random replicates per each size $N = \{24, 48, 72, 96, 120, 196\}$ (asterisks).

The equation of the regression line was

$$X(L) = \mu_2 L + \mu_3 = 65.07L - 1038 \tag{12}$$

with 95% confidence intervals (60.38, 69.76) and (-1589, -585.6) for the slope and the intercept respectively. This linear model supplied $X(L)$ in Eqs. (7) and (9.b).

Such a result seemed to confirm the above supposition from phenomenology about the linear dependence of X on L. Nevertheless, more data points were required to increase the

precision and tighten the relatively wide confidence intervals. For very large lattices, when the intercept becomes negligible (1038 << 65.07 L), the relations (8) and (10.b) were nicely approximated for $\bar{\varepsilon} > \bar{\varepsilon}_{peak}$ by

$$\bar{\sigma} = \bar{E}^{o}\left[\left(1 - N_p / \mu L^2\right) - \frac{\Delta n(\bar{\varepsilon}, L)}{65L}\right]\bar{\varepsilon} \tag{13.a}$$

$$\bar{D}(\bar{\varepsilon}, L, n) = \frac{n(\bar{\varepsilon}_{peak}, L)}{\mu L^2} + \frac{\Delta n(\bar{\varepsilon}, L)}{\mu_2 L} = \frac{N_p}{\mu L^2} + \frac{\Delta n(\bar{\varepsilon}, L)}{65L} \tag{13.b}$$

The damage parameter (13.b) implied a C^1 discontinuity due to the abrupt change of the denominator from L^2 to L at the critical point ($\bar{\varepsilon}_{peak}$). While $n(\bar{\varepsilon})$ was a C^1 continuous function at $\bar{\varepsilon}_{peak}$, the damage is C^0 and the damage rate $\partial n(\bar{\varepsilon})/\partial\bar{\varepsilon}$ discontinuous, in agreement with Figs. 2 and 3.

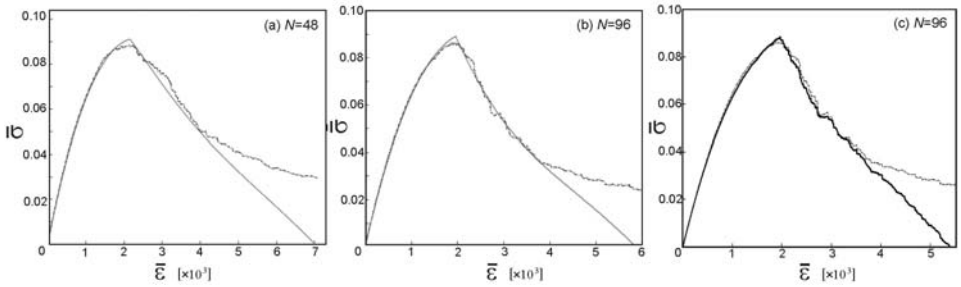

Figure 6. Overall model fitting for N = 48 and N =96 with X from OLS (Eq.(13)). $n(\bar{\varepsilon}, L)$ and $\Delta n(\bar{\varepsilon}, L)$ were estimated via scaling relations. C) Improved fit for N=96 when numerical data were used directly for $n(\bar{\varepsilon}, L)$ and $\Delta n(\bar{\varepsilon}, L)$ instead of scaling relations in the constitutive relations (9).

The choice of the Q data points to be used in the evaluation of (11) was crucial for the accuracy of $\hat{X}(L)$ and depends on what part of the response is of interest. This analysis aimed at capturing the steepest descent of the softening regime after the transition and only the corresponding points (about 25% of softening dataset) were selected to minimize the model error in that part. The performance of the analytical expressions (9) were compared in Fig. 6 against the original average simulation data for N = 48 and N = 96, respectively.

3.4 Interpretation and Limits of Relations for Softening

The model estimated the numerical data for most of the design space. Concerns might arise about the accuracy of relations (7) and (9.b) for the softening phase. Essentially two aspects determined the performances of the model:

1. the selected model form (7) for the damage parameter $\bar{D}$ and
2. the accuracy of the estimates $n(\varepsilon, L)$ and $\Delta n(\varepsilon, L)$ from scaling.

At first, by assuming that the model form (7) was correct, we focused on the second issue. The scaling relations for $n(\varepsilon, L)$ and $\Delta n(\varepsilon, L)$ from Eqs. (1) and (8) referred to the average data, obtained by first averaging the original $n - \bar{\varepsilon}$ curves of individual replicates for each size and then, after scaling, by fitting a regression model to the scaled data. This twofold "filtering" process smeared out the irregularities characteristic of each replicate (compare Fig.2d with Fig.7 in [1]). Thus, while on one side we obtained smooth analytical relations capable of estimating the average microcracks number for any lattice size, on the other the characteristic "details" of each individual replicate were lost. Fig.6c shows the model obtained from Eqs. (8) for $N = 96$ when average n and Δn from simulations were used in place of the scaling relations. The new estimates "shadow" the simulation data of the softening phase better than before. Evidently a better knowledge of n and Δn yielded a more accurate constitutive model. For these simulations, the difference between the estimates of n and Δn from scaling relations and from simulations never exceeded 10% for any lattice size. However, the predictive power did not change significantly.

To assess the other issue about the appropriateness of the selected model form, Eqs. (7) and (9) were tested against individual lattice simulations. Six individual replicates for $N = \{24, 48, 72, 96, 120, 192\}$ were randomly picked. This time the values of n, Δn and N_p were obtained directly from the simulation. As the model was satisfactory for the hardening phase, the previous estimate of μ was kept for all cases. Instead, the parameter $X(L)$ in (7) was re-estimated for each replicate via Eq. (13). These new values of $\hat{X}(L)$ are marked in Fig.5 by asterisks and fall reasonably close to the line (14) for the average values.

The remarkable agreement between the models and numerical data was demonstrated in detail by Rinaldi et al. [3]. Complex patterns and discontinuities were well captured for most of the softening phase. The models were in general able to reproduce the response also after the change of curvature following the initial steep descendent from the peak. Notably, these results were achieved by merely re-estimating a sole parameter $X(L)$.

4 A Microstructural Approach to Understand the Softening Transition

As a final remark, a microstructural approach can better highlight the underlying physics of the softening transition. The rationale is to correlate the spring rupturing with the orientation of each spring [22,23]. With regard to Figure 7A, consider a 2D lattice model similar to the previous one but with perfect geometry ($\alpha_L = 1$), where the springs represent grain-boundary links between hexagonal grains and can only have two orientations to the loading axis, either horizontal or diagonal at ±60°. In this scheme there is just mechanical disorder in the form of random critical strains distribution. The corresponding mechanical

response from a simulated tensile test in displacement controlled mode is shown Figure 7B and represents the locus of all stable configurations $\{\bar{\sigma}, \bar{\varepsilon}\}$ reached at any imparted $\bar{\varepsilon}$. The dotted lines mark the snap-back patterns incompatible with ε, which are signature features of micro-cracks avalanches. Through a bottom-up analysis of tensile test simulations, it can be demonstrated that the damage process on the microscale is a discrete function - amongst other things [22, 23] - of the ratio between the applied strain and the micro-strains in the springs. In particular, the damage increase when the micro-strain in one spring overcomes its critical strain $\varepsilon^*(\bar{\varepsilon})$, such that $D(\bar{\varepsilon}) = f(\varepsilon^*/\bar{\varepsilon})$. Then, from the examination of $\varepsilon^* vs. \bar{\varepsilon}$ in Figure 7C, one can clearly appreciate that the softening transition is a divide between two regimes, one where the relation is initially linear and one where it becomes eventually much scattered for $\varepsilon^* >> \bar{\varepsilon}$. This implies that an explosion in the micro-strain fluctuations in the lattice causes the transition. Furthermore, the plots demonstrates that while the horizontal springs (i.e., the grain boundaries (GBs), normal to the tensile axis) play a major role in the first part of the damage process (note the higher rupturing rate of horizontal springs), the transition represents a cross-over to a regime dominated by a rupture process highly contributed by GBs at an angle. In other words, while the damage process is highly dependent on the orientation of the springs, in a sense it becomes independent of spring-orientation after the transition, which is an aspect of consequence for microstructure engineering and damage tolerance design.

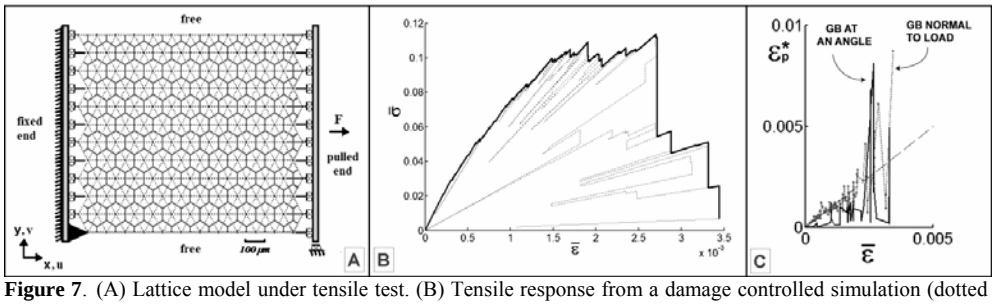

Figure 7. (A) Lattice model under tensile test. (B) Tensile response from a damage controlled simulation (dotted lines) with a large avalanche marking damage localization at the peak response ($\bar{\varepsilon}$ = 2.7 10^{-3}). (C) Greater contribution to damage before localization is from grain boundaries (GB) normal to the load. But GB orientation becomes irrelevant afterwards.

5. Summary and Conclusions

The statistical damage mechanics theory, developed within the present framework, was proposed originally by Krajcinovic and Rinaldi [1]. The sequel paper [3], constituting the gist of this review paper, was committed to constitutive modeling, failure, damage tolerance and durability of structures – issues largely neglected in engineering practice and research [2]. The results offered in [3] displayed the effectiveness of the proposed statistical damage model in the study of the softening regime and failure. The results outlined the potential of this statistical damage mechanics model, which went well beyond the limits of the traditional continuum damage mechanics.

Specifically, the primary conclusions of the analyses reviewed in the present paper were the following:

- the choice of the model form in Eq. (7) was appropriate;
- a simple model could reproduce a variety of softening responses;
- microstructural approach can reveal the finer nature of the softening transition;
- the greatest accuracy was achieved by calibrating the constitutive relations on an individual simulation; the same constitutive relations of the mean response can be used by simply re-estimating $X(L)$ from the simulation data;
- the greater accuracy for the individual replicate was determined by the usage of un-filtered simulation data for n and Δn in place of the average estimates.

The findings corroborated and clarified the proposed constitutive model. The last conclusion pointed out that the continuous approximation of $n(\bar{\varepsilon}, L)$ and $\Delta n(\Delta\bar{\varepsilon}, L)$ from scaling relations overlooked large discontinuities in the $n-\bar{\varepsilon}$ data registered in correspondence of large avalanches (both the peak and post-peak). Although the scaling relations (1) and (2) represented an average behavior and offered the general "trend" for all lattice sizes, an accurate model—capable of matching the data from an individual test—was achieved upon introduction of the specific details of $\Delta n(\Delta\bar{\varepsilon}, L)$ on case-by-case bases. Thus, the additional numerical data improved the precision of the statistical analysis.

The scale invariant damage curves proposed in [1] were re-examined and finalized in [3] to obtain the analytical constitutive relations (9) for the entire damage process. The damage parameter was properly defined in the softening phase to attain this result. In the hardening phase the process was driven by a fractal set of exponent two, while in the softening phase the fractal dimension tended towards one. This work outlined the importance of the statistical methods, such as ordinary least squares, maximum likelihood and hypothesis testing, for the selection of the model parameters. These techniques were the basis for data-driven reasoning and decision making in damage tolerance.

References

[1] Krajcinovic, D. and Rinaldi, A. (2005). Statistical Damage Mechanics – 1. Theory, *J. Appl. Mech.* **72**: 76-85.

[2] Goranson, U.G. (1993). Damage Tolerance – Facts and Fiction, 14th Plantema Memorial Lecture Presented at the 17th Symposium of the International on Aeronautical Fatigue, Stockholm, Sweden.

[3] Rinaldi, A., Krajcinovic, D., Mastilovic, S. (2006). Statistical Damage Mechanics – Constitutite Relations. *J. Theoretical Appl. Mech.* (Warsaw) **44** (3): 585-602.

[4] Krajcinovic, D., Rinaldi, A (2005). Thermodynamics and Statistical Physics of Damage Processes in Quasi-ductile Solids, *Mech. Mater*. **37**: 299-315.

[5] Davidge, R. W. (1979). Mechanical Behavior of Ceramics, Cambridge University Press, Cambridge, UK.

[6] Mastilovic, S., Krajcinovic, D. (1999). Statistical Models of Brittle Deformation: Part II: computer simulations, *Int. J. Plasticity* **15**: 427-456.

[7] Lawn, B. 1993. Fracture of Brittle Solids (2nd ed.). Cambridge University Press, Cambridge, UK.

[8] Mura, T. (1982). Micromechanics of Defects in Solids, Martinus Nijhoff Publishers, The Hague, Belgium.

[9] Kestin, L. (1992). Local-Equilibrium Formalism Applied to Mechanics of Solids, *Int. J. Solids Structures* **29** (14/15): 1827-1836, Pergamon Press, Oxford, UK.

[10] Nemat-Nasser, S., Hori, M. (1999). Micromechanics: Overall Properties of Heterogeneous Materials (2nd ed.). North-Holland, Amsterdam, The Netherlands.

[11] Espinosa, H.D., Zavattieri, P.D., 2003. A grain level model for the study of failure initiation and evolution in polycrystalline brittle materials. Part I: Theory and numerical implementation. *Mech. Mater.* **35**: 333-364.

[12] Krajcinovic D. (1996). Damage Mechanics. North-Holland, Amsterdam, The Netherlands

[13] Hansen A., Roux S., Herrmann H.J. (1989). Rupture of central-force lattices. *J. Phys. France* **50**: 733-744.

[14] Montgomery, D.C., Peck, E.A, Vining, G.G. (2001). Introduction to Linear Regression Analysis, John Wiley and Sons, New York, USA.

[15] Curtin, W.A., Scher, H. (1990). Brittle fracture in disordered materials, J. Mater. Res. **5** (3): 535-553.

[16] Mastilovic, S. (2010). Further Remarks on Stochastic Damage Evolution of Brittle Solids Under Dynamic Tensile Loading. *Int. J Damage Mech.* doi: 10.1177/1056789510385294.

[17] Monette, L., Anderson, M. P., 1994. Elastic and fracture properties of the two-dimensional triangular and square lattices. *Model. Simul. Mater. Sci. Eng.* **2**: 53-66.

[18] Rinaldi, A., Krajcinovic, D., Peralta, P., Lai, Q. (2008). Lattice models of polycrystalline microstructures: A quantitative approach. *Mech. Mater.* **40**: 17-36.

[19] Ostoja-Starzewski, M., 2002. Lattice models in micromechanics. *Appl. Mech. Rev.* **55** (1): 35-60.

[20] Krajcinovic, D., Vujosevic, M. (1998). Strain localization – short to long correlation length transition, *Int. J. Solids Struct.* **35** (31-32): 4147-4166.

[21] Mastilovic, S. (2008). Investigation of Dynamic Behavior of Brittle Solids by Discrete Systems, Faculty of Construction Management, Union University, Belgrade, Serbia.

[22] Rinaldi, A., Lai, Y-C. (2007). Damage theory of 2D disordered lattices: energetics and physical foundations of damage parameter. *Int. J. Plasticity* **23**: 1796-1825.

[23] Rinaldi, A. (2009). A rational model for 2D disordered lattices under uniaxial loading. *Int. J. Damage Mech.* **18** (3): 233-257.

PACKAGE TRANSPORT USING GRAVITY CHUTE SYSTEM - FUZZY LOGIC APPROACH

M. Šelmić[1], R. Šelmić[2]

Faculty of Transport and Traffic Engineering,
The University of Belgrade, Vojvode Stepe 305, 11000 Belgrade
e-mail: [1]m.selmic@sf.bg.ac.rs, [2]ratkos@sezampro.rs

Abstract: In this paper we provide an overview of designs and potential applications of the gravity chute system. The general differential equation of the package motion on the gravity chute that has arbitrary shape described by Bernoulli equation is presented. The general equation can be applied to the different special cases of gravity chutes. According to this equation, the output velocity of the package at the exit of chute is a function of inclination angle, friction coefficient and the initial velocity of the package. In practice, the main objective is to minimize the output velocity of the package. An appropriate model for regulating this velocity by changing the inclination angle in case of gravity chute is presented in this paper. Artificial intelligence methods, including fuzzy logic, are very useful tools for managing and controlling devices in electrical and mechanical engineering. The developed model is based on the principles of fuzzy logic and has been used to optimize performance of gravity chute. A fuzzy logic model manages the gravity chute inclination angle. The input parameters of the proposed fuzzy logic model are: friction coefficient, mass of the packages and number of packages. The presented models, kinematical and fuzzy, are verified by numerical examples.

1. Introduction

The paper deals with different types of the gravity chute and its potential applications. The general differential equation of the package motion on the gravity chute that has arbitrary shape described by Bernoulli equation is presented. This general equation can be applied to special cases of gravity chutes. According to this equation, the output velocity of the package at the exit of chute is a function of inclination angle, friction coefficient and the initial velocity of the package. In the practice, the main objective is minimizing the output velocity of the package. Bearing this in mind, an appropriate model for regulating this output velocity by changing the inclination angle in the case of gravity chute is shown in the paper. The model is based on the fuzzy logic principles.

Having in mind the fact that fuzzy sets can represent linguistic knowledge, i.e. that they can describe qualitative information in a rigorous way, fuzzy logic has become a very popular technique for controlling numerous automatic processes [11]. Results obtained by fuzzy control indicate that it can be used as a convenient tool to solve a certain type of problem.

In this paper, we formed a fuzzy logic model that manages the output velocity of the package, as it affects the inclination angle of the gravity chute. In practice, this is achievable by installing the appropriate mechanical or hydro-mechanical mechanism in the gravity chute. The input parameters of the proposed fuzzy logic model are: friction coefficient, mass of packages and number of packages.

The main goals of this paper are to offer detailed analysis of different gravity chute types and to research the possibility of developing a fuzzy controller to control the process of package movement across gravity chute. In addition, this paper develops a simple fuzzy controller by referring to the operators' knowledge and experience.

The rest of this paper is organized as follows. After Introduction, Section 2 is related to a short review of basic and essential, relevant papers on fuzzy logic and fuzzy control. Section 3 of this paper gives an overview of different gravity chute types and its potential applications. Section 4 contains detailed analysis of fuzzy control, while a description of the problem considered and the fuzzy reasoning algorithm are given in Section 5. Concluding remarks are in Section 6.

2. Short literature review

The similar analysis as the one presented in this paper is done in details for the rectilinear, circular and cycloid gravity chutes, as well as helical chutes in the papers [13, 14]. The same problem is considered, to a lesser extent, in the monograph literature [1, 5]. This paper proposes improved differential equations and a dynamic model based on fuzzy logic, which provides the major optimization of gravity chute parameters, primarily the optimal inclination angle.

Fuzzy logic was first proposed by Lotfi A. Zadeh of the University of California at Berkeley in 1965 paper [17]. The papers of Mamdani [7] and Mamdani and Assilian [8] presented the first application of fuzzy set theory in the control of a dynamic process. In their paper, Mamdani and Assilian discussed the control of a laboratory steam engine. Tong [12] presented and analyzed a large number of experimental applications of a fuzzy control.

Recently, a lot of papers that deal with fuzzy logic controllers appear in the relevant literature. The authors of paper [4] introduced a neuro-fuzzy controller for the speed control, a permanent magnet synchronous motor drive. The authors used a four layer neural network to adjust input and output parameters of membership functions in a fuzzy logic controller.

In their paper, [3 authors tried to minimize power consumption used to operate the ventilation system. To achieve the objectives, fuzzy control methods have been usually utilized due to the complex and nonlinear behavior of the system.

The design of fuzzy controllers for the implementation of behaviors in mobile robotics is a complex and highly time-consuming task and it was presented in [9]. In this paper, the automated design of a fuzzy controller using genetic algorithms for the implementation of the wall-following behavior in a mobile robot is described.

A fuzzy logic was also used in the paper [2. This paper presents a data-driven design methodology able to generate a Takagi–Sugeno–Kang (TSK) fuzzy model for maximum energy extraction from the variable speed wind turbines. In order to obtain the TSK model, fuzzy clustering methods for partitioning the input–output space, combined with genetic algorithms (GA), and recursive least-squares (LS) optimization methods for model parameter adaptation are being used.

According to author's knowledge, there are no papers dealing with implementation of fuzzy logic concept into the gravity chute parameters optimization.

3. A survey of the constructions and potential applications of gravity chute

The gravity chute is fixed device which is used for transport of piece or loose load under the influence of the gravitational force. The package (load) is lowered by slipping or rolling down the supporting (working, sliding) surface. The gravity chute permits a continuous gravitational transport at different speeds, in a rectilinear or curvilinear manner, depending upon the type of package and the function of the gravity chute. According to its function

and package shape, the supporting surface is the basic part of the gravity chute whereas the lateral slides are not so heavily loaded, and their function is more of a directional nature.
According to the supporting surface, which also determines the path of the packages, the gravity chute can be:

- Inclined, where the longitudinal axis of the supporting surface is in the vertical plane (Fig. 1a and 1b), and
- Spiral (helicoidally), where the supporting surface is spiral (Fig. 1c).

The cross-section of the gravity chute is a groove, which is open in the inclined gravity chute, with either closed or open spirals, having a rectangular, trapezioform, semicircular, trough-like or circular form.

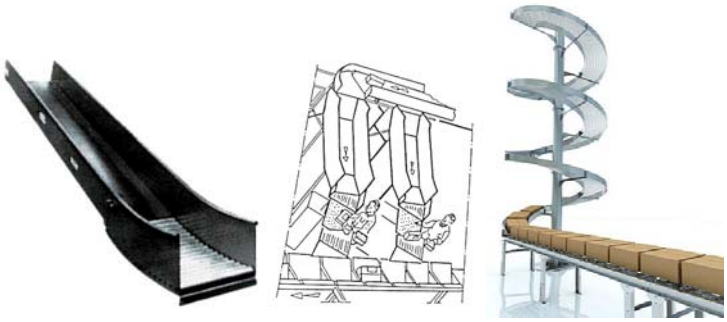

a) b) c)

Figure 1. Gravity chutes: a) inclined, b) inclined gravity chute in the Post, c) spiral

There is a wide variety of applications of the gravity chute:

- For transporting postal deliveries (parcels, bags and boxes with postal correspondence) or for filling bags and containers with the sorted mail;
- For connecting certain technological stages of the transportation process;
- As parts of the working units or certain transportation devices.

The significant applications of the gravity chutes results in the development of construction with various technical parameters (length, width, height, friction coefficient), which has ensured the required working regimes as well as an economic construction in a limited area. In order to realize the required movement regime, which implies the corresponding speed of the package, and at the same time to avoid failures (the discontinuing of the package upon the gravity chute), it is necessary to determine exactly the basic gravity chute parameters: its form, cross-section, material, length, width, angle of trapper, etc. The determination of these parameters is possible by applying a detailed kinematics analysis of the movement of the package, which has been done in this paper for inclined rectangular, circular and cycloid gravity chute.

3.1. The inclined curvilinear gravity chute

The inclined gravity chutes with the curvilinear supporting surface (Fig. 2) ensure a slow movement of the package without shock, since owing to the centrifugal force, the frictional resistance increases.

By using the gravity chutes of this type, package movement can be accomplished according to the desired rule. Production of such gravity chutes are more complex compared to rectilinear gravity chute.

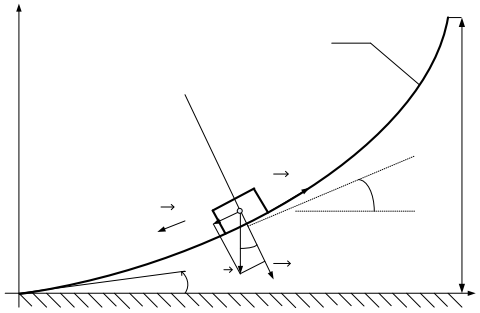

Figure 2. The inclined curvilinear gravity chute

Let us first consider the general case of a movement along a curvilinear gravity chute of an arbitrary case of movement, whose equation is $y=y(x)$. The differential equation of the package movement, which is considered to be a material point, is:

$$m\frac{dv}{dt} = mg\sin\alpha - \mu\left(mg\cos\alpha + m\frac{v^2}{\rho}\right), \tag{1}$$

where:

m, v – mass and speed of the package respectively,
μ – the coefficient of friction,
ρ – the current radius of the curve.

After the substitution of the expression for the radius of the curve s – arc of the gravity chute, equation (1) is transformed into following differential equation:

$$v\frac{dv}{ds} = g(\sin\alpha - \mu\cos\alpha) - \mu\frac{v^2}{\rho}. \tag{2}$$

After the substituting of the expression for the differential arc $ds = \sqrt{1+y'^2}\,dx$, radius of the curve $\rho = [1+(y')^2]^{3/2}/y''$ and trigonometrically transformation, equation (2) becomes:

$$\frac{dv}{dx} - \mu\frac{y''}{1+y'^2}v = g(\mu - y')v^{-1}. \tag{3}$$

The solution obtained by the Bernoulli differential equation (3) is:

$$v^2 = e^{2\mu arctgy'} \left[2g \int (\mu - y') e^{-2\mu arctgy'} dx + C\right]. \quad (4)$$

In order to determine the integral constant *C,* the condition for the speed of the descent of the package from the gravity chute (at point *K*) will be utilized:

$$x = 0, y = 0, \ v = v_k \ \Rightarrow C = v_k^2.$$

Finally, the solution is presented by equation (5):

$$v^2 = e^{-2\mu arctgy'} \left[2g \int (y' - \mu) e^{2\mu arctgy'} dx + v_k^2\right]. \quad (5)$$

Equation (5) ensures the solution of the two practical and very significant problems:
a) For the given gravity chute form $y = y(x)$, determine the velocity change $v = v(x)$;
b) Determine the trajectory $y = y(x)$ for the most favorable velocity change law $v = v(x)$.

3.2. The inclined rectilinear gravity chute (the inclined plane)

In the case of the inclined rectilinear gravity chute (the inclined plane) (Fig. 3) equation of supporting surface is:

$$y = kx = tg(\alpha_g)\, x = \frac{h}{b} x \quad (6)$$

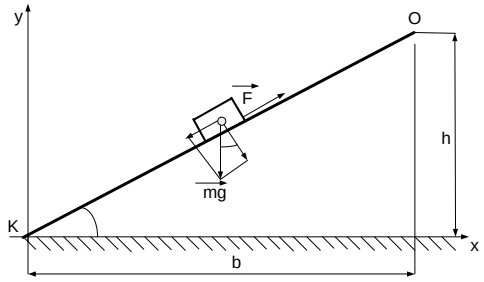

Figure 3. The inclined rectilinear gravity chute

Substituting equation (6) in the general expression for the speed of package (4), we can get the velocity of a package that slides on the inclined rectilinear gravity chute:

$$v^2 = 2g\,(\mu - tg\alpha_g)(x - b) + v_0^2\,, \quad (7)$$

where: v_0 is initial package velocity in the point O(*b,h*).

Velocity of package movement at the end of gravity chute, at the point *K* (0.0) is:

$$v_k = \sqrt{2g(h - b\mu) + v_0^2} \tag{8}$$

The same expression can be arrived at basing upon the live force law or by applying differential equations of package movement directly for this gravity chute.
From equation (8) required coefficient of friction, a very important structural parameter, can be determined in order to achieve optimal package velocity at the end of gravity chute, v_k .

$$\mu = \frac{h}{b} - \frac{v_k^2 - v_0^2}{2gb} \quad . \tag{9}$$

3.3. The inclined circular gravity chute

In the case of inclined circular gravity chute (Fig. 4), which geometrically represents the arc with central angle β , differential equation of package movement (1) taking following shape:

$$\frac{dv}{d\varphi} + \mu v = gR(sin\alpha - \mu cos\alpha)v^{-1}, \tag{10}$$

where:
R - radius of the circle,
α, φ - central angles of a circle, which determine the current position of the package.

The fact that between the variable angles α and φ exists relation $\alpha + \varphi = \beta = const$, i.e.

$d\varphi = -d\alpha$ leads to the differential equation (10) new form:

$$\frac{dv}{d\alpha} - \mu v = gR(\mu cos\alpha - sin\alpha)v^{-1}. \tag{11}$$

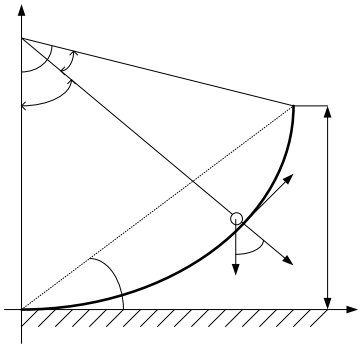

Figure 4. The inclined circular gravity chute

The solution of the differential equation (11) is:

$$v^2 = 2gR\,\frac{2\mu\sin\alpha+\cos\alpha-2\mu^2\cos\alpha}{4\mu^2+1} + C e^{2\mu\alpha}\,, \tag{12}$$

where the integration constant is determined from the condition $\alpha = \beta\ (\varphi = 0),\ v = v_0$

$$C = e^{-2\mu\beta}\left(v_0^2 - 2gR\,\frac{2\mu\sin\beta+\cos\beta-2\mu^2\cos\beta}{4\mu^2+1}\right).$$

Velocity of package movement at the end of the gravity chute (for $\alpha = 0,\ \varphi = \beta$) is:

$$v_k^2 = 2gR\,\frac{1-2\mu^2}{4\mu^2+1} + e^{-2\mu\beta}\left(v_0^2 - 2gR\,\frac{2\mu\sin\beta+\cos\beta-2\mu^2\cos\beta}{4\mu^2+1}\right). \tag{13}$$

3.4. The inclined cycloid gravity chute

The parametric equations of the cycloid are:

$$x = r\,(\theta + \sin\theta),\quad y = r(1-\cos\theta)\,, \tag{14}$$

where:
r – radius of the circle whose rolling at the line p, point on the circle M describes a cycloid.
θ – central angle of the circle that determines the current position of the package (Fig. 5).

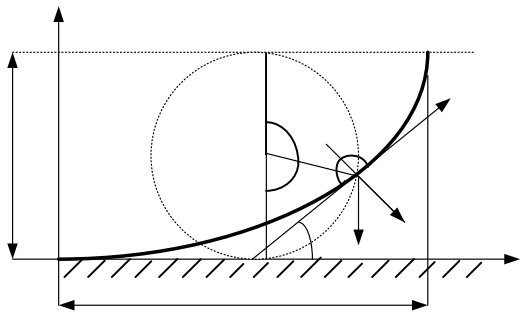

Figure 5. The inclined cycloid gravity chute

The parametric equations of cycloid in function of central angle φ $(\varphi = \pi - \theta)$ are:

$$x = r(\pi - \varphi + \sin\varphi), \quad y = r(1 + \cos\varphi). \tag{15}$$

The geometric parameters of cycloid are:

$$ds^2 = dx^2 + dy^2 = 4r^2\sin^2\frac{\varphi}{2}\,d\varphi^2, \quad ds = 2r\sin\frac{\varphi}{2}d\varphi, \quad s = r\left(1 - \cos\frac{\varphi}{2}\right). \tag{16}$$

$$\sin\alpha = -\frac{dy}{ds} = \cos\frac{\varphi}{2}, \quad \alpha = \frac{\pi}{2} - \frac{\varphi}{2}. \tag{17}$$

$$\rho = \left|\frac{ds}{d\alpha}\right| = 4r\sin\frac{\varphi}{2}, \tag{18}$$

where:
s - corresponding cycloidal arc; α - angle of the tangent cycloid at the point M, ρ - the radius of curvature of cycloid.
Taking into account (16), (17) and (18) the differential equation of the package movement (1) gets following form:

$$\frac{dv}{d\varphi} + \frac{\mu}{2}v = gr\left(\sin\varphi - 2\mu\sin^2\frac{\varphi}{2}\right)v^{-1} \tag{19}$$

The solution of the differential equation obtained (17), under the initial conditions $\varphi = 0$ $s = 0, v = v_0$ is:

$$v^2 = v_0^2 e^{-\mu\varphi} + \frac{4gr}{\mu^2+1}\left[e^{-\mu\varphi} - \left(\cos\frac{\varphi}{2} - \mu\sin\frac{\varphi}{2}\right)^2\right]. \quad (20)$$

The velocity of the package at the end of the gravity chute at point *K* is, for $\varphi = \pi$:

$$v_K^2 = v_0^2 e^{-\pi\mu} + \frac{4gr}{\mu^2+1}(e^{-\pi\mu} - \mu^2) \quad (21)$$

The package arrives to the cycloid end point for a short time, much faster comparing to the movement trough any other given curve line.

3.5. Numerical example

For given parameters for all three gravity chute: μ=0,36 , h=6 m , b=14,14m, l=15,36m , α = 23° v_o=0,5 m/s, r = 3 m, R = 18,1 m, β=46°=0,80 rad, the dependence of package movement velocity upon the coefficient of friction (Fig.6) and the dependence of current speed of package parameters, which indirectly determines the path taken, are determined and shown in the graphs (Fig. 7,8 and 9).
The best final package velocity, according to the safety of packages, is achieved by the inclined circular gravity chute (Fig. 6). In that case final package velocity is minimal and equals to $v_k = 1{,}90$ m/s . However, this conclusion is valid for the friction coefficient

μ=0,36.
When the coefficient of friction is less than a certain value, in this case less than 0.325, the final package velocity of circular gravity chute is greater than in the case of other two gravity chutes.

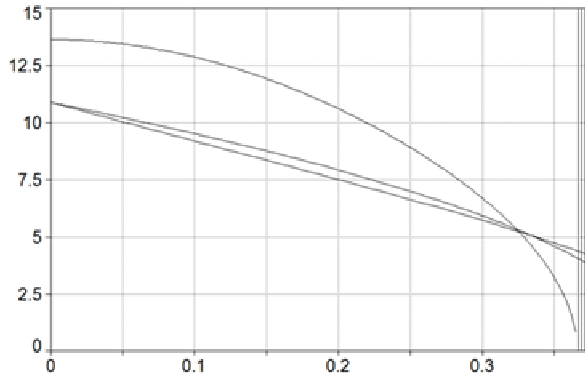

Figure 6. The dependence of the final package movement velocity v_k upon the coefficient of friction, μ:

a) The rectilinear gravity chute, b) The circular gravity chute, c) The cycloid gravity chute

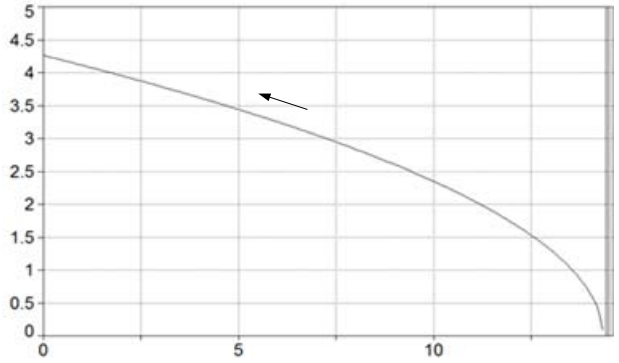

Figure 7. The dependence of current package velocity v upon coordinates x, in case of the rectilinear gravity chute

The incline circular and cycloid gravity chutes, unlike the rectilinear gravity chute, provide a lower final velocity of package movement as well as movement of packages without shock. They also make possible that acceleration of packages that move though gravity chute (point *T*, Fig. 8.9), which becomes slower, primarily due to supplementary force of friction due to the influence of centrifugal force. While such gravity chute is more complex to create comparing to the rectilinear gravity chute, the positive effect of these gravity chutes is achieved by making combine rectilinear gravity chute or rectilinear gravity chute with two or more segments [11].

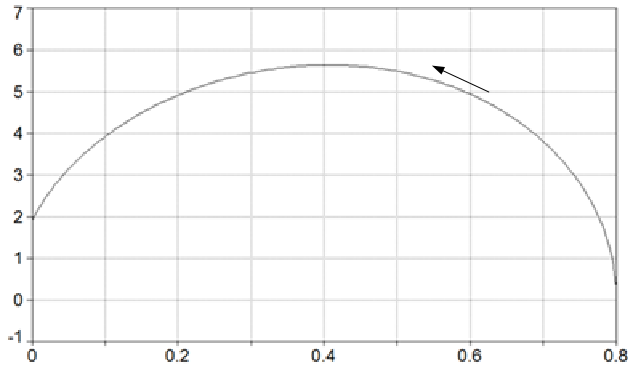

v
m/s

Figure 8. The dependence of current package velocity v upon the angle □ in case of the circular gravity chute

Figure 9. The dependence of current package velocity v upon the angle φ in case of the cycloid gravity chute

4. Fuzzy control in detail

As an alternative, fuzzy control provides a formal methodology for representing, and implementing a human's heuristic knowledge about how to control a system. Fuzzy controller is unique in its ability to utilize both qualitative and quantitative information. Qualitative information is gathered not only from the expert operator strategy, but also from the common knowledge.

Fuzzy controllers are very simple conceptually. They consist of an input stage, a processing stage, and an output stage. The input stage maps sensor or other inputs, such as switches, thumbwheels, etc., to the appropriate membership functions and truth values. The processing stage invokes each appropriate rule while generating a result for each, then combines results of the rules. Finally, the output stage converts the combined result back into a specific control output value.

v
m/s

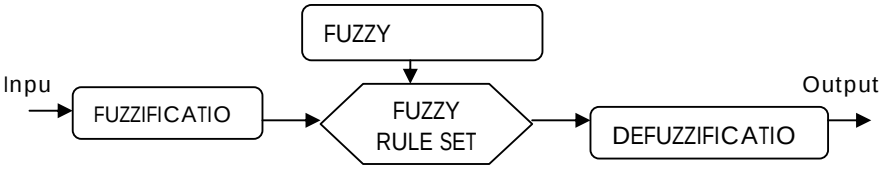

Figure 10. Fuzzy logic process

The most common shape of membership functions is triangular, although trapezoidal and bell curves are also used, but the shape is generally less important than the number of curves and their placement. The processing stage is based on a collection of logic rules in the form of IF-THEN statements, where the IF part is called the "antecedent" and the THEN part is called the "consequent". Typical fuzzy control systems have dozens of rules.

There are several different ways to define the result of a rule, but the one used in this paper is the most common Mamdani "max-min" inference method, in which the output membership function is given the truth value generated by the premise.

The results of all the rules that have fired are "defuzzified" to a crisp value by one of several methods, but we used very popular "centroid" method, in which the "center of mass" of the result provides the crisp value.
The diagram below demonstrates max-min inferencing and centroid defuzzification for a system with input variables "x_1", "x_2", and "x_3" and an output variable "y".

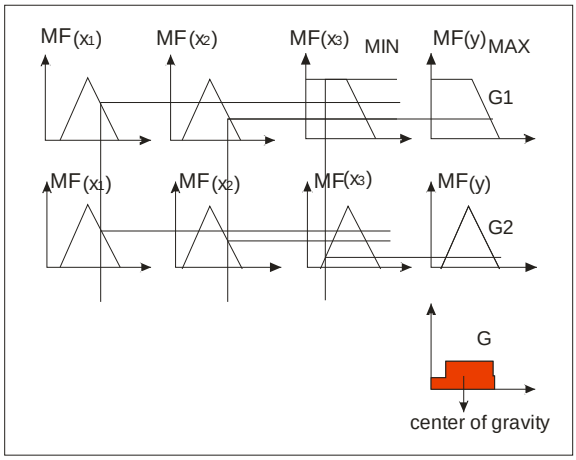

Figure 11. Max-min inferencing and centroid defuzzification

5. Description of the problem considered and fuzzy control process

When making decisions in a fuzzy environment, for the purpose of fuzzy logic modeling, it is necessary to transform all input data into fuzzy variables which can be expressed in quantitative form through fuzzy sets [15].
The basic geometric and functional gravity chute parameters, in addition to the coefficient of friction may vary depending on the materials of packages, gravity chute height and angle. In packages transport stochastic effect is very pronounced. Besides that, failures (delays) during a package transport can occur. Having in mind the fuzzy theory and possibilities of its applications, authors formed a model for managing performances of gravity chute. The main goals are to optimize gravity chute output velocity by changing the inclination angle and thus to minimize number of failures and unpredicted situations.
Normal operating performances of gravity chute depend on coefficient of friction, mass and number of packages. A coefficient of friction is strongly related to inclination angle, because it has to be satisfied condition of slippery:$\alpha>\rho$, where ρ=arctgμ is angle of friction. The recommendation is that inclination angle of gravity chute should be larger for 2-3 grades comparing to the angle of friction.
Usually, operators that work on gravity chute are not able to accurately determine the coefficient of friction of the package. But, they can determine this by using linguistic variables for mass of the package, the package volume and number of packages as the relevant parameters.
Our model based on a fuzzy logic consists of three input variables, as shown on Fig.12. and one output variable, the inclination angle of the gravity chute.

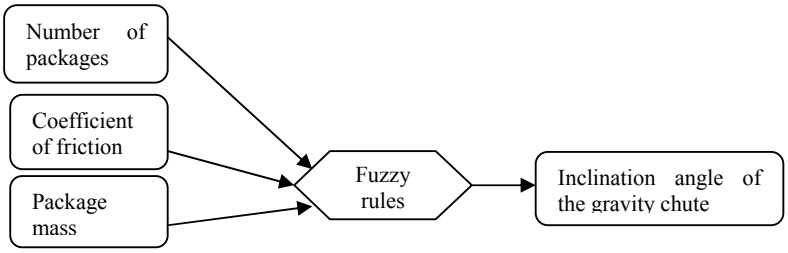

Figure 12. Fuzzy logic model for determining the inclination angle of the gravity chute

For each of the input variables of fuzzy model, we defined the appropriate intervals. The first input variable, *number of packages,* was separated into three classes: small, medium and large. The second input variable, *the mass of the package*, was divided into three intervals: small, medium and big. Finally, the last input variable, *coefficient of friction*, was divided into five intervals: very small, small, medium, heavy and very heavy.
For each of the input variables membership functions were formed. To form the membership functions we used triangular and trapezoidal shapes (for forming and testing phase of the logical model we used program Matlab r2008a). The following tables and figure show membership functions for each of input variables.

Table 1: Values used for input variable *number of packages* membership function definition (measured in package per minute unit)

Small	**Medium**	**High**
from 0 to 6	from 2 to 18	from 14 to 20

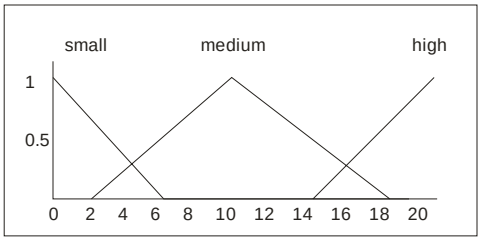

Figure 13. Membership functions of input variable number of packages

Table 2: Values used for input variable *coefficient of friction* membership function definition

Very low	**Low**	**Medium**	**Heavy**	**Very Heavy**
from 0.21 to 0.44	from 0.32 to 0.55	from 0.44 to 0.66	from 0.55 to 0.78	from 0.66 to 0.78

Table 3: Values used for input variable *package mass* membership function definition (measured in kilograms)

Small	Medium	High
from 0 to 10	from 2 to 29	from 20 to 31.5[1]

Output variable is defined as the inclination angle of the gravity chute and it is divided into five intervals: very small, small, average, big and very big. To define the output variable membership functions we used triangular fuzzy numbers.

Table 4: Values used for output variable *the inclination angle* membership function definition (measured in radians)

Very small	Small	Average	Big	Very big
From 20 to 25	from 20 to 30	from 25 to 35	from 30 to 40	from 35 to 40

The most important step in the formation stage of the logical system is to properly define fuzzy rule set. Fuzzy rule set was formed on the basis of "if-then" rules. One possible rule would look:

IF the *number of packages* is x1 and IF the *coefficient of friction* is x2 and IF the *mass of the package* is x3
THEN *the inclination angle of the gravity chute* equals to y.

After fuzzy rules are formed we can determine necessary inclination angle of the gravity chute. In such way we formed 45 fuzzy rules (Fig. 14). In order to obtain the best possible results, output and input membership functions were tailored. Also, it is important to notice that it was necessary to revise some rules in order to achieve satisfactory results.

On Figure 14 one numerical example is presented. If number of packages is 5 per time unit, coefficient of friction is 0.36 and package mass is 1 kilos, and according to fuzzy logic model necessary inclination angle of the gravity chute is 25 rad.

[1] Maximal allowed package mass according to the rules in the Post is 31.3 kilos.

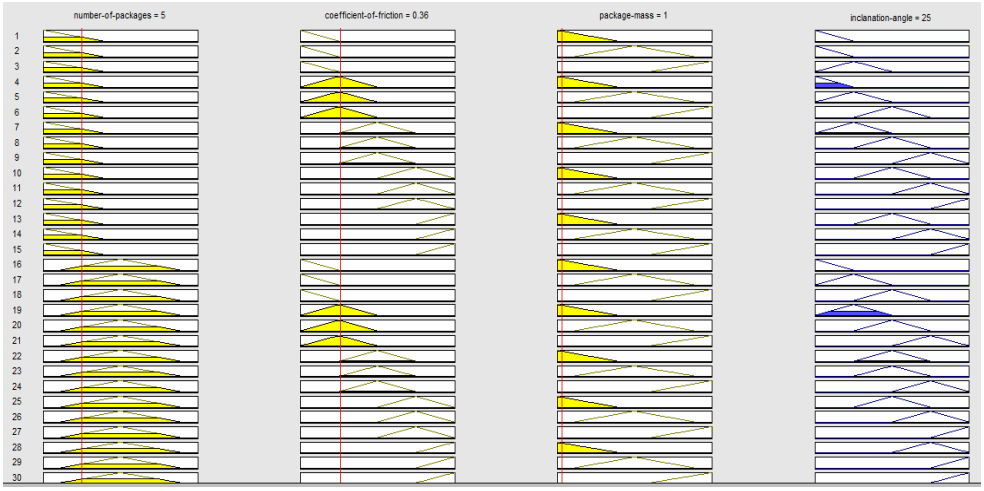

Figure 14: Numerical example

6. Conclusion

In this paper we gave an overview of different types of gravity chutes. The potential applications are also presented in the first part of the paper along with the kinematics equation.

The basic geometric and functional gravity chute parameters, in addition to the coefficient of friction may vary depending on the materials of packages, gravity chute height and angle. In packages transport stochastic effect is very pronounced. Besides that, failures (delays) during package transport can occur. Having in mind the fuzzy theory and possibilities of its applications, authors formed a model for managing performances of gravity chute. The main goals are to optimize gravity chute output velocity by changing the inclination angle and thus to minimize number of failures and unpredicted situations.

Proposed model, based on the fuzzy logic concepts, includes coefficient of friction, packages mass and number of packages in order to obtain optimal inclination angle of the gravity chute.

References

[1] *Буланов Э. А, Третенко Ю. И, Лебедева Е. В* (1985) Подъемно-транспортные устройства почтовой связи, *Радио и связь*, Москва.

[2] Calderaroa V, Galdia V, Piccoloa A and Siano P (2008) A fuzzy controller for maximum energy extraction from variable speed wind power generation systems, *Electric Power Systems Research,* 78, pp. 1109-1118.

[3] Chua B, Kima D, Hongb D. Parkc J, Chungb J T, Chungd J and Kime TH (2008) GA-based fuzzy controller design for tunnel ventilation systems, *22nd Symposium on Automation and Robotics in Construction, ISARC*, pp. 130-136.

[4] Elmasa C, Ustun O and Sayana H H (2008) A neuro-fuzzy controller for speed control of a permanent magnet synchronous motor drive, *Expert Systems with Applications,* 34, pp. 657-664.
[5] *Ивановский К. Е* (1969) Теоретические основы перемещения штучных грузов, *Машиностроение*, Москва.
[6] Lee K K, Hwang C S and Young I M (1995) Design and implementation of fuzzy-logic based aircraft drag-chute system, *Proceedings of the 6th International Fuzzy Systems Association World Congress*, pp. 41-44.
[7] Mamdani E H (1981) Advances in the linguistic synthesis of fuzzy controllers, in: E.H. Mamdani and B.R. Gaines (eds.), *Fuzzy Reasoning and Applications,* Academic Press, London.
[8] Mamdani E H, Assilian S (1975) Eexperiment in linguistic synthesis with a fuzzy logic controller", *International Journal of Man-Machine Studies,* 7, pp. 1-13.
[9] Mucientes M, Morenoa D L, Bugarína A, Barroa S (2007) Design of a fuzzy controller in mobile robotics using genetic algorithms, *Applied Soft Computing,* 7, pp. 540-546.
[10] Simoes M G, Bose B M, Spiegel R J (1997) Fuzzy Logic Based Intelligent Control of a Variable Speed Cage Machine Wind Generation System, *IEEE Transactions on power electronics,* 12, pp. 84-95.
[11] Teodorović D., Vukadinović K., Traffic control and transport planning: a fuzzy sets and neural networks, Kluwer Publishers, USA, 1998.
[12] Tong R M (1977) A control engineering review of fuzzy systems, *Automatica,* 13, pp. 559-569.
[13] Šelmić R, Cvetković P, Bukumirović M (1994) Transport tereta gravitacionim kliznicama – analiza relevantnih parametara, *Tehnika – Saobraćaj,* 41, pp. 1-3.
[14] Šelmić R, Cvetković P, Analiza brzine kretanja tereta kod zavojnih kliznica, *Tehnika – Mašinstvo,* 44, pp. 10-13.
[15] Vukadinović K, Teodorović D (1994) A fuzzy approach to the vessel dispatching problem, *European Journal of Operational Research,* 76, pp. 155-164.
[16] Wensrich M C (2003) Evolutionary optimization in chute design, *Power Technology*, 138, pp. 118-123.
[17] Zadeh L A (1965) Fuzzy sets, *Information and Control*, 8, pp. 338-353.

ANALYZING METHODS FOR THE RESPONSES OF THE LAUNCHING SYSTEM SUBJECTED TO THE STOCHASTIC EXCITATION CAUSED BY WIND

Dragoslav Živanić[1], Vlado Đurković[2], Siniša Jovančić[3]

[1] Military Tehnical Institute, Belgrade,
Ratka Resanovića br. 1, Belgrade,
E-mail: dragoslav@ptt.rs
[2] Military Academy, Belgrade,
Pavla Jurišića Šturma 33, Belgrade,
e-mail: svskom@scnet.rs
[3] Military Tehnical Institute, Belgrade,
Ratka Resanovića br. 1, Belgrade,
e-mail: jovancicsinisa@gmail.com

Abstract. This paper presents two analyzing methods for the responses of the launching device at vehicle subjected to the random stimulations caused by the wind: mean square response method and Monte Carlo simulation method. The basis hypothesis of the stohastic functions and the relevant theoremes nedeed for the analysis of the random processes are presented.
Keywords: Stochastic processes, Chebyshev inequality, Central limit theorem, Ergodic stochastic processes, Correlation function, Spectral density, Mean square response , Monte Carlo simulation.

1. Introduction

One of the most important aspects of studying the launching systems response to external disturbances are the value and the nature of changes of the firing line. The first step in the analysis of system behavior is the identification of the external stochastic disturbances, and their introduction into the appropriate mechanical model. The paper describes two basic approaches to analyzing of the system response to stochastic disturbances (which is represented by the influence of horizontal wind to the structure):
a) Monte Carlo simulation
b) Mean square response.

2. Random disturbances

The atmosphere flowing - wind, constantly changes its state, both in space and in time (direction, orientation and speed). Because we can not predict the wind speed certainly, we can consider it as a random process, $X(r,t)$, where r is vector which indicates the position of the observing point with the respect to the selected origin of coordinates. Measuring the wind speed at a certain place during a certain period of time obtain realization of a random process $X(r_1,t)$. Complex of all possible realization makes a random process. At certain place r_1 and time t_1 random process becomes a continuous random variable $X(r_1,t_1)$, for

which can be defined probability distribution function $F_X(x;r_1,t_1)$ and probability density function $f_X(x;r_1,t_1)$.

Any of these two functions completely describes the stochastic nature of random variable. However, it is often impossible to obtain any of them from the available data. Instead, some average values of certain functions could be available: mathematical expectation $\mu_X(r_1,t_1)$, variance (dispersion) $D=\sigma^2$ and correlation function $R_{XX}(r_1,t_1;r_2,t_2)$. Correlation function defines the relationship between the value of the random variables $X(r_1,t_1)$ and $X(r_2,t_2)$ in two different times and at two different places:

$$R_{XX}(r_1,t_1;r_2,t_2)=E\left[X(r_1,t_1)X(r_2,t_2)\right]=\int_{-\infty}^{+\infty}\int_{-\infty}^{+\infty}x_1\cdot x_2\cdot f_{XX}(x_1;r_1,t_1:x_2;r_2,t_2)dx_1dx_2 \tag{1}$$

As the space locations and the moments of time are closer, the correlation between $X(r_1,t_1)$ and $X(r_2,t_2)$ strengthens. Then function becomes $R_{XX}(r_1,t_1)=\sigma_X^2(r_1,t_1)+\mu_X^2(r_1,t_1)$.

If the random process is stationary (invariant to translation of time) and if the mean values and autocorrelation function does not change from one sample to another, then the random process is ergodic. In mathematical terms, this means that there is no dependence of the elementary events, so it's all the same which realization of random process we choose.

If the ergodicity is not confirmed, the process is:

- nonergodic – a special analysis are needed,
- possible ergodic, but the intervals of time series are short

Thus, for some random process that is made up of infinite set of realizations: $X^{(1)}(r,t)$, $X^{(2)}(r,t)\ldots X^{(N)}(r,t)$, the average value of the whole set are::

$$\begin{aligned}\mu&=\lim_{N\to\infty}\frac{1}{N}\sum_{i=1}^{N}X^{(i)}(r,t)\\ \sigma^2&=\lim_{N\to\infty}\frac{1}{N}\sum_{i=1}^{N}\left(X^{(i)}(r,t)-\mu\right)^2\\ R_{XX}(\rho,\tau)&=\lim_{N\to\infty}\frac{1}{N}\sum_{i=1}^{N}X^{(i)}(r,t)\,X^{(i)}(r+\rho,t+\tau)\end{aligned} \tag{2}$$

If the only one realization of random process is known $X^{(1)}(r,t)$, during time T and space shift S, apply the following equations using the substitution $i=1$ и $N=ST$. For ergodic process applies: $R_{XX}(0)=\sigma_X^2+\mu_X^2$ and $R_{XX}(\infty)=\mu_X^2$.

Ergodic process can be analyzed in frequent range, by Fourier transformation of the autocorrelation function – power spectral density:

$$S_x(\omega)=\frac{1}{2\pi}\int_{-\infty}^{+\infty}R_{xx}(\tau)e^{-j\omega\tau}d\tau \tag{3}$$

3. Wind Modeling

In engineering application, the wind is represented by its mean velocity and fluctuating (turbulent) component. Figure 1.b shows the change of horizontal wind according to the altitude, where can be seen that the turbulence is more expressive closer to ground as a direct consequence of the inhomogeneity of the soil (level of the soil heating, relief, etc.). In general, whenever inhomogeneities occur in the soil, there are circulation and local-scale inhomogeneities in the atmosphere.

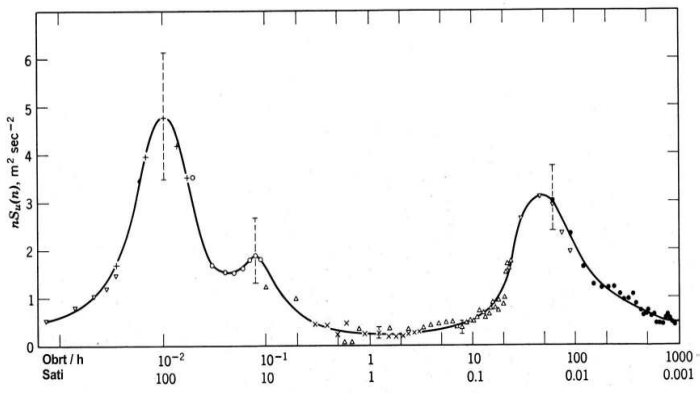

Figure 1.a.

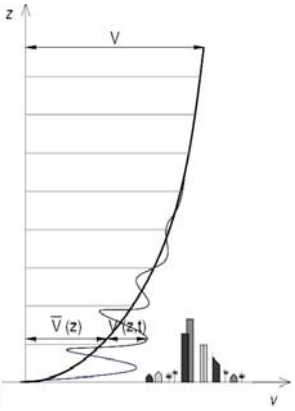

Figure 1.b.

Let's consider the spectrum intensity of wind near the ground according to Van der Hoven (Figure 1.a). On the abscissa the number of cycles per hour (top row of numbers) and the periods in hours (bottom row of numbers) are indicated, and the ordinate is the product of amplitude with frequency. Field maximum, the spectral density diagram shows that the main part of the kinetic energy of wind is in the fluctuation components of wind speed. The three maximums are clearly expressed here:

1) the first is the period of about four days, which corresponds to the synoptic weather systems
2) the second is for a period of 12 hours, which is a consequence of the diurnal changes of the wind speed
3) the third is for a period of about a minute, which is a reflection of the turbulent fluctuations of wind speed

The generally accepted standard for measuring wind speed in a certain area is a ten-minute average (the most portion of the kinetic energy of wind is in the part of average flow and is the least dependent on the current fluctuations of velocity) measured at the altitude of $10\,m$ above the ground.

Turbulent wind speed generation is carried out by passing the white noise through the forming filter. In addition, the filter transfer function is determined by the known spectrum of turbulent wind according to von Karman, Harris or Dryden spectrum, obtained empirically , lit. [9], [12]. The Figure 2 shows a characteristic change of horizontal wind speed.

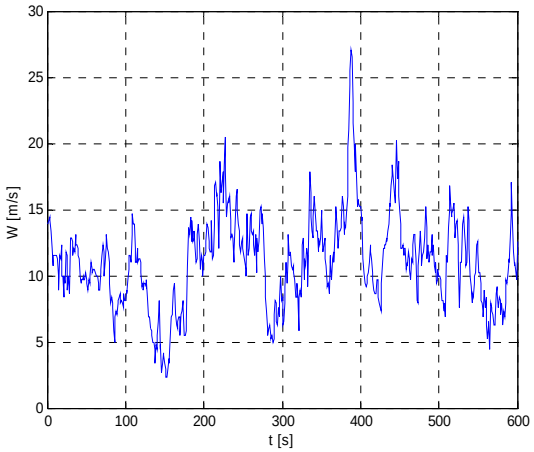

Figure 2

4. Mechanical Model MLRS

This paper will consider the SVRL mechanical model composed of rigid bodies with concentrated masses and deformable elements with elastic and damping connections shown in [1].

According to the accepted model, the movement (oscillation) of MLRS is defined by the following generalized coordinates:

- z_1 - vertical movement the vehicle frame in the direction of z axis,
- ε - rotating of the vehicle frame around around the transverse axis y,
- θ - rotating the launching device around the elevation rotating point O_3

In this case, the Lagrangian equations of second order are very suitable for analyzing the oscillatory motion, which present the mathematical model represented by three inhomogeneous linear differential equations, in the following form:

$$\frac{d}{dt}\left(\frac{\partial E_k}{\partial \dot{q}_r}\right)-\frac{\partial E_k}{\partial \dot{q}_r}+\frac{\partial E_p}{\partial q_r}=Q_r^n, \tag{4}$$

Kinetic energy of the system:

$$E_k=\frac{1}{2}\cdot\left\{m_1\cdot V_{O1}^2+J_{1y}\cdot\varepsilon^2+m_2\cdot V_{O2}^2+J_{2y}\cdot\varepsilon^2+m_4\cdot V_{O4}^2+m_5\cdot V_{O5}^2+J_{5y}\cdot\left(\varepsilon^2+\theta^2\right)\right\}, \tag{5}$$

where: m_1 - the rear of the chassis mass concentrated at point O_1, m_2 - the front of the chassis mass concentrated at point O_2, $m_4=m_k$ - the mass of the cradle's console, $m_5=m_L$ - mass of loaded/unloaded launching device and charger, J_{1y} - the main central moment of inertia of the rear MLRS, J_{2y} - the main central moment of inertia of the front of MLRS, J_{5y} - the main central moment of inertia of a launching device and charger.

The potential energy of the system:

In order to simplify the mechanical model the weight of the system is considered to be balanced by elastic forces of the springs in the position of static equilibrium, i.e. differential equations of motion are set with respect to the position of the equilibrium, which means

that the weight of the vehicle will not be taken into account when setting the differential equations of motion:

$$E_p = \frac{1}{2}\cdot\left\{C_1\cdot\left(z_1 + l_1\varepsilon\right)^2 + C_2\cdot\left(z_1 - l_2\varepsilon\right)^2 + C_3\cdot\left[\left(e\theta\cdot\sin\gamma\right)^2 + \left(p\varepsilon\cdot\sin\delta\right)^2 - 2e\theta p\varepsilon\cdot\sin\gamma\cdot\sin\delta\right]\right\} \quad (6)$$

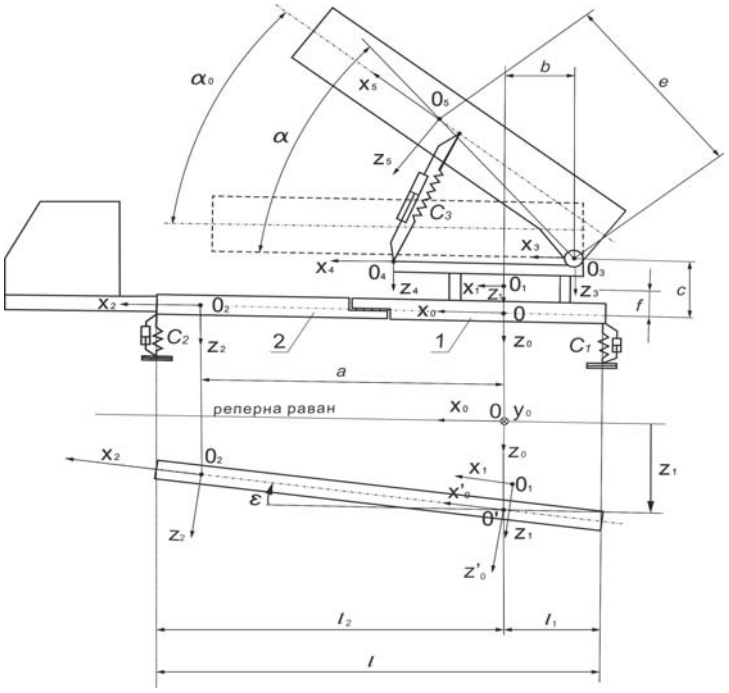

Figure 3

Reley's dissipative function:

All dumpings in the system can be replaced by an equivalent viscous damping, where the damping force is proportional to the first order of the speed function of dissipation (dissipative function), and the coefficient of proportionality is the coefficient of dumping β. During the MLRS oscillations, the dominant damping oscillation energy occurs in the supports (the ground), and as a representative of the damping of the MLRS structure itself is quite enough to take the dumping in reduced mechanisms of the elevation. Dissipative energy of the system is:

$$\Phi = \frac{1}{2}\cdot\left\{\beta_1\cdot\left(\dot{z}_1 + l_1\dot{\varepsilon}\right)^2 + \beta_2\cdot\left(\dot{z}_1 - l_2\dot{\varepsilon}\right)^2 + \beta_3\cdot\left[\left(e\dot{\theta}\cdot\sin\gamma\right)^2 + \left(p\dot{\varepsilon}\cdot\sin\delta\right)^2 - 2e\dot{\theta}p\dot{\varepsilon}\cdot\sin\gamma\cdot\sin\delta\right]\right\} \quad (7)$$

Generalized disturbance forces:

Random disturbance is introduced through the aerodynamic forces acting on the structure:

$$\overline{F} = \begin{bmatrix} X \\ Z \end{bmatrix} = \begin{bmatrix} -F_D \\ -F_L \end{bmatrix} = \begin{bmatrix} -0{,}5\cdot\rho W^2\cdot A_{ref1}\cdot C_D(\alpha) \\ -0{,}5\cdot\rho W^2\cdot A_{ref2}\cdot C_L(\alpha) \end{bmatrix} \quad (8)$$

where: ρ - the air density, W - the wind speed, A_{ref1} , A_{ref1} - the characteristic surfaces, $C_D(\alpha)$ and $C_L(\alpha)$ - coefficients of drag and lift pressure.

Based on the general form of disturbing force, and with respect to the geometrical characteristics shown in Figure 4, generalized disturbance force is:

$$Q_k = \sum_{j=1}^{3} \vec{F}_r \frac{\partial \vec{r}_k}{\partial q_k} = \begin{bmatrix} Q_{z_1} \\ Q_\varepsilon \\ Q_\theta \end{bmatrix} = \begin{bmatrix} -F_L \\ F_D\left(c + p\sin\alpha_1\right) - F_L\left(b - p\cos\alpha_1\right) \\ F_D p\sin\alpha_1 - F_L p\cos\alpha_1 \end{bmatrix} \tag{9}$$

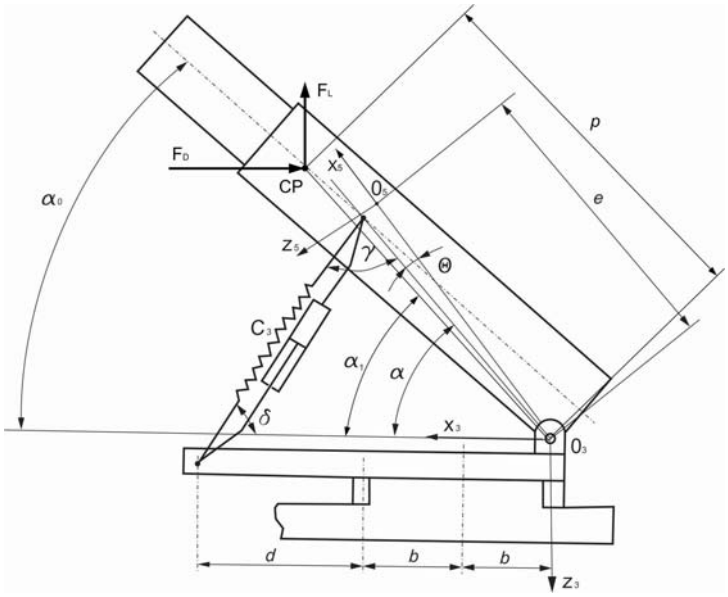

Figure 4

By differentiating the expression for the kinetic, potential and dissipation energy, and the shift in the general form of Lagrange equations we obtain a system of three nonlinear differential equations in the following form:

$$\mathbf{A}\cdot\ddot{q} + \mathbf{B}\cdot\dot{q} + \mathbf{C}\cdot q = Q_k \tag{10}$$

which define the oscillatory movement of the system, with appropriate matrices **A**, **B** and **C** functions of generalized coordinates and velocities. Analysis of the system response will be done by Monte – Carlo method and mean square response method.

Method of *Monte – Carlo* is based on the repetition of simulation (experiment) and data processing to determine the statistical characteristics of the system with random inputs. To increase the accuracy of the statistical parameters it is necessary to perform a large number of simulations.

Method of *spectral analyze* – which is based on the known autocorrelation function of excitation $R_{xx}(\tau) = \begin{bmatrix} D_{Q_{z1}} & D_{Q_\varepsilon} & D_{Q_\theta} \end{bmatrix}^T \cdot e^{-k|\tau|}$, respectively power spectral density of excitation forces $S_x(\omega) = \begin{bmatrix} D_{Q_{z1}} & D_{Q_\varepsilon} & D_{Q_\theta} \end{bmatrix}^T \frac{2k}{k^2+\omega^2}$, and mechanical characteristics **A**, **B** and **C** define:

- Frequency response function of system: $H(\omega) = \left(-A\omega^2 + j\omega B + C\right)^{-1} \cdot I$ (11)
- Output spectral density: $S_y(\omega) = \left|H(\omega)\right|^2 \cdot S_x(\omega)$ (12)

• Mean square response: $E\left[y^2\right]=\int_{-\infty}^{+\infty} S_y(\omega)d\omega=\int_{-\infty}^{+\infty}\left|H(\omega)\right|^2\cdot S_x(\omega)d\omega$ (13)

For the analysis of probability of exceeding the response will be used:
Chebyshev inequality: The probability that the outcome of an experiment with the random variable X, unknown probability density, will fall more than some arbitrary constants ε beyond the mean of μ_X is less than

$$p\left(\left|X-\mu_X\right|\geq\varepsilon\right)\leq\frac{D_x}{\varepsilon^2} \quad (14)$$

Central limit theorem: Sum of independent random variables gravitates to the random variable with normal distribution, regardless of the distribution of each random variable individually.

5. Numerical example

For a numerical example the MLRS will be considered, loaded with 12 rockets, during the launching from the hard clay surface with elevation of 45^0. To solve the system of the differential equations, as in general form (5), the numerical method Runge-Kutta will be used. The responses of the system to a random excitation are shown in the Figure 5.
For 20 simulated wind blows, by statistical analysis of structure response the following are obtained:

q	μ_q	D_q	σ_q
z_1	$3,6305\cdot10^{-5}$	$7,9990\cdot10^{-10}$	$2,8282\cdot10^{-5}$
ε	$5,4620\cdot10^{-5}$	$1,8027\cdot10^{-9}$	$4,2458\cdot10^{-5}$
θ	$1,7752\cdot10^{-4}$	$1,9029\cdot10^{-8}$	$1,3795\cdot10^{-4}$
$\Delta\alpha\approx\varepsilon+\theta$	$2,3214\cdot10^{-4}$	$3,2544\cdot10^{-8}$	$1,8040\cdot10^{-4}$

On the basis of Chebyshev inequality, probability that the angle of deviation from the firing line $\Delta\alpha$ exceeds the value of half a thousandth in the artillery scale 64-00, by the calculated values $D_{\Delta\alpha}$ is less than: $p\left(\Delta\alpha>0.5"\right)\leq0,11899$.

Assuming a normal distribution of angle deviation from the firing line, the probability that the angle of deviation exceeds the value of half a thousandth, respectively one thousandth in the artillery scale 64-00, is equal: $p\left(\Delta\alpha>0.5"\right)=0,054162$, $p\left(\Delta\alpha>1"\right)=0,000015$.

Figure 6 shows the standardized autocorrelation function of the force excitation and its spectrum excitation is approximated by $\rho_{xx}=e^{-k|\tau|}$, where is the exponent $k=0,096$.
Figure 7 shows the frequency response function of system (the forms with diagonal matrix) $H(\omega)$, and spectral responses of the system. The fundamental frequencies of oscillation are: $\omega_1=15,2$; $\omega_2=31,8$ and $\omega_3=65,2$ Hz. The mean square response is obtained by numerical integration of the expression (13), and the solutions are variances D_q, upon which according to the Chebysev inequality (14) the estimate of probability can be carried out.

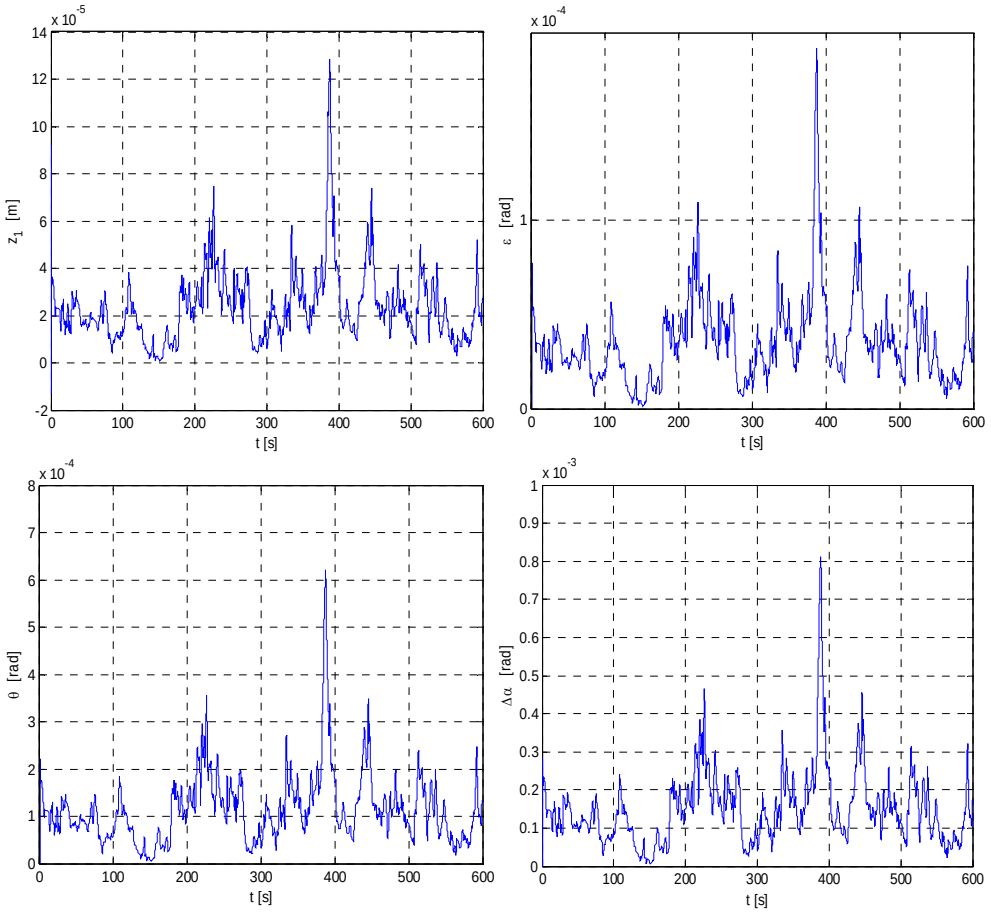

Figure 5

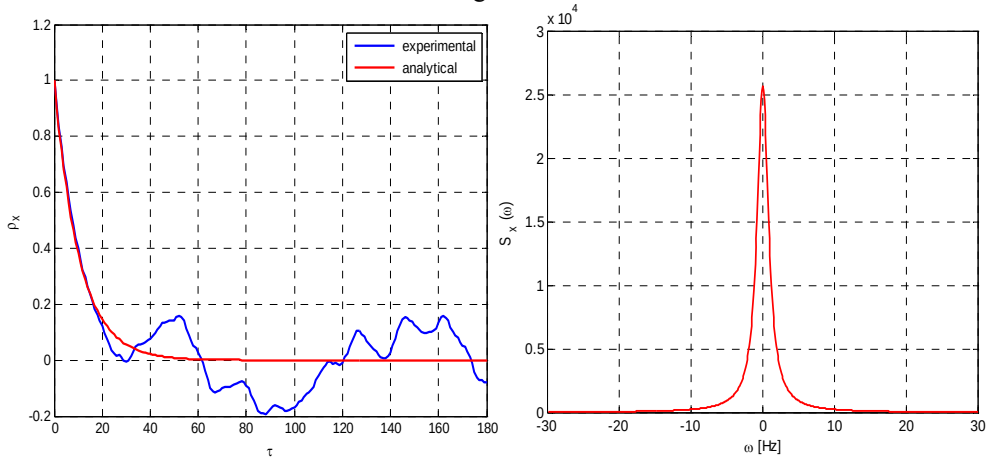

Figure 6

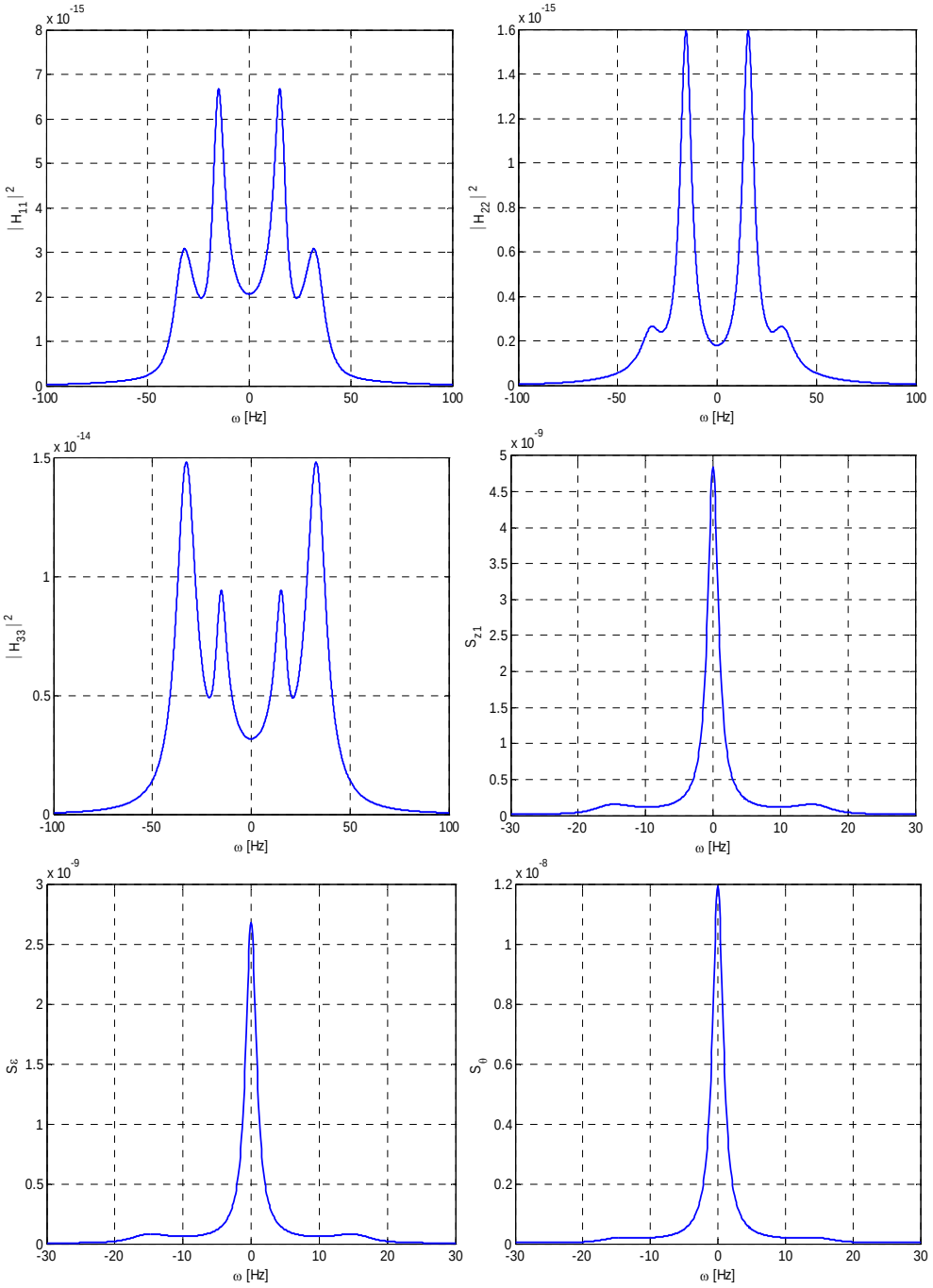
x 10^-15
|H11|^2
ω [Hz]
x 10^-15
|H22|^2
ω [Hz]
x 10^-14
|H33|^2
ω [Hz]
x 10^-9
Sz1
ω [Hz]
x 10^-9
Sε
ω [Hz]
x 10^-8
Sθ
ω [Hz]

Figure 7

6. Conclusion

On the basis of the calculated displacements and their probabilities can be concluded that even extremely strong horizontal wind has not a major impact on the deviation of the firing line from the set value.

Chebyshev inequality gives the approximate solution of probability, but its good feature is that it does not take into account the distribution of random variables. The actual value of probability was calculated assuming a normal distribution (it's usually supposed that distribution of responses is of the same type as the excitations, so besides normal distribution in [9], [10] and [11], the Weibull or Reley distribution is suggested).

The peaks in graphs of the response of the complex frequency on the fundamental frequencies of oscillation are the consequence of the coupled elements in the system (10). By approximating the excitation spectrum with an analytical curve, the influence on the response of the system at higher frequencies is lost.

The spectrum of the excitation could be seen as "white noise", if the exponent in the autocorrelation function will be of higher value k (that means that the autocorrelation function is approximately of the exponential character).

The matrix **A** changes its value according to the change of generalized coordinates, but due to relatively small movements, those changes are imperceptible and it is practically constant

.

Literature

[1] Živanić D., Uticaj oscilovanja samohodnih višecevnih lansera raketa na rasturanje raketa i kadencu lansiranja, Magistarski rad. Mašinski fakultet, 1990.

[2] Newland D. E., An Introduction to Random Vibrations, Spectral & Wavelet Analysis, by Dover Publications , Inc, New Jork, 1993.

[3] Radosavljević LJ., Male oscilacije materijalnog sistema sa konačnim brojem stepeni slobode, Mašinski fakultet, Beograd, 1986.

[4] Radosavljević LJ., Teorija oscilacija, Mašinski fakultet, Beograd, 1972.

[5] Harti V. C., Rubinstein M. F., Dynamics of structures, by Prentice-Hall, Inc, Englewood Cliffs, New Jersey,1964.

[6] Вентцељ Е. С., Теорија вероватностеј, Государственное издатељство физико-математическој литератури, Москва, 1962

[7] Merkle M., Verovatnoća i statistika, Akademska Misao, Beograd, 2002.

[8] De Silva C. W., Computer Tehniques in Vibration, by Taylor & Francis, Boca Raton, 2007.

[9] Holmes J. D., Wind Loading of Structures, by Taylor & Francis, Abingdon, 2007.

[10] Rajković B., Fedor M., Mikrometeorologija, Fizički fakultet, Beograd, 2002.

[11] Rajković B., Popov Z., Procena brzine vetra na izabranim lokacijama, Novi Sad, 2005.

[12] Graovac S., Automatsko vođenje objekata u prostoru, Akademska Misao, Beograd, 2005.